Biodegradable polymeric nanoparticles for neuroprotection against neonatal brain injury

Andrea Joseph

A dissertation

submitted in partial fulfillment of the

requirements for the degree of

Doctor of Philosophy

University of Washington

2021

Reading Committee:

Elizabeth Nance, Chair

Lilo Pozzo

Sandra Juul

Program Authorized to Offer Degree:

Department of Chemical Engineering

University of Washington

Abstract

Biodegradable polymeric nanoparticles for neuroprotection against neonatal brain injury

Andrea Joseph

Chair of the Supervisory Committee:

Dr. Elizabeth Nance, Assistant Professor

Department of Chemical Engineering

Hypoxic-ischemic encephalopathy (HIE) is the leading cause of permanent brain injury in term newborns. HIE can lead to significant impairments during development and adulthood including cerebral palsy, learning disability, and epilepsy. Currently, there is no effective cure for HIE, and the standard-of-care only offers a 15% reduction in the risk of death or disability. This thesis project is focused on an engineering approach to the development of novel treatment strategies for this devastating disease.

First, we must understand and evaluate the disease physiology in order to determine the desired therapeutic activity: how will a therapeutic enter the brain and interrupt injury pathways? It is well known that HIE is initiated as a result of low flow of oxygen and blood flow to the brain (hypoxic-ischemia, or HI), producing a crisis of energy failure. This crisis precipitates excitotoxicity and neuroinflammation, which propagate the resulting injury over hours, days, and years. However, critical intervention points remain unknown, including the time window for effective treatment and the permeability of delivery barriers in the brain. We demonstrate that injury can be ameliorated by curcumin, a broad-acting anti-inflammatory and antioxidant molecule, when incorporated into a nanoparticle formulation for improved solubility and stability (Chapter 3). This supports the further investigation of drugs which are able to target inflammatory and oxidative stress pathways. We additionally use an *ex vivo* brain slice model to assess nanoparticle transport in the diseased brain microenvironment, discovering disease-mediated disruptions to the extracellular matrix and changes in microglial uptake of nanoparticles (Chapter 4). This supports the further investigation of nanotechnology for applications in brain-targeted drug delivery.

Next, we optimized the nanoformulation to more effectively address delivery challenges. Small molecule drugs and biologics face challenges including limited solubility, low circulation time, and low penetration of the brain. Drug encapsulation in a poly(lactic-*co*-glycolic acid) (PLGA) nanoparticle is an accessible solution, especially as PLGA nanoparticles have been FDA-approved in other disease applications. As we will demonstrate, the PLGA nanoparticle platform can be tailored for improved brain penetration by modulating surface properties: 1) the conjugation of poly(ethylene glycol) (PEG), which improves nanoparticle diffusive ability through brain tissue, and 2) the inclusion of surfactants in the formulation, specifically polysorbate 80 (P80), which improves brain cell-specific targeting (Chapter 5). The investigation of a brain-penetrating, cell-specific drug delivery platform is relevant for a variety of brain diseases and allows for tailoring the formulation specifically to the HIE model.

This project culminates by evaluating the optimized PLGA-PEG/P80 nanoparticle platform for catalase drug delivery after HIE (Chapter 6). Catalase is a therapeutic enzyme that combats oxidative stress disease pathways but exhibits poor nanoparticle encapsulation due to its hydrophilic nature. Using a hydrophobic ion-pairing technique to increase catalase's hydrophobicity, we formulate catalase-loaded PLGA-PEG/P80 nanoparticles. After *in vivo* administration in the HIE model, we demonstrate catalase nanoparticle accumulation in the injured tissue and a significant neuroprotective effect. The work in this thesis supports the further investigation of curcumin and catalase nanoformulations for the treatment of HIE. More broadly, it demonstrates that a range of therapeutic cargo can be successfully incorporated into biodegradable, brain-penetrating nanoparticles for application across the spectrum of neurological disorders.

Acknowledgements

If you want to go fast, go alone. If you want to go far, go together.
– African proverb

It is a testament to the excellence of the Nance Lab, Department of Chemical Engineering, and University of Washington that, looking back on graduate school, I feel overwhelming gratitude. What an opportunity it was to spend 5 years solving interesting problems with some of the smartest and kindest people in the world! Let me begin by thanking the custodians of the land upon which my research was conducted. The UW Seattle campus sits on the traditional, ancestral, ceded and unceded territory of the Duwamish, Puyallup, Suquamish, Tulalip and Muckleshoot nations. These Coast Salish Peoples have been and continue to be responsible for protecting and preserving the natural spaces that supported this thesis work.

When I think about the ways I have grown since 2016— knowing who I am and what I value, becoming a better communicator, managing stress and conflict— I know most of this was influenced by two incredible women in my life. Elizabeth, thank you for showing me who I want to be: an excellent mentor above everything; a patient teacher and relentless advocate for her students; a strategic leader; someone who faces the past with honesty and the future with hope. You helped me see myself in academia and your support means the world to me. Mom, you have always been kind and wise, but I want to particularly thank you for how you have brought mindfulness into your own life and shared your journey with me. It feels rare and special to not be able to imagine a better mom than the one you have. The world would be a better place with more women like you both.

I am thankful for the time and service of my thesis committee, without whose support I also would not be receiving my PhD. Lilo, I've learned so much from the way you ask questions and how passionately you fight for the things that are important to you, especially diversity in science and outreach that positively changes our community. Sunny, working with your lab has grounded me and helped me see the long game: one day, in a few decades, maybe something I'm studying will save lives the way your work has. Ying, it was wonderful to meet you as we discussed the microvessel collaboration; I look forward to reading about it in the future! Thank you all for reading through this document; I hope I have made it concise and interesting.

I am grateful for the support of colleagues who made the work in this thesis possible. First, Tommy, thank you for teaching me about (among many things) brain health and ancestral health, and for sharing your home gym. Half of these projects, and all of my sanity, would not look the same without you! Thank you to the rest of the Neonatology team as well, especially Kylie for her friendship and superpowers in managing labs and people. In the Nance Lab, I want to highlight the contributions of: Rick, who trained me on most of what I know; Mike, whose team spirit and eye for detail truly keep the lab running; Mengying, who trained me on everything Rick didn't; and Chris, who always brings a fresh perspective. When research got tough, it was a blessing to rely on and decompress with my fantastic team of undergraduate students (Danny, Zach, Denise, Ana, Norah, Tora, Georges, Hugo, and Emily—I'll also include Victoria, who wasn't technically my mentee but is so awesome I have to mention her!) and high schoolers (Maria, Sanjana, and Meghan). What an incredible honor it has been to work with so many people who are going to change the world.

Finally, I want to thank my family and friends outside of lab for their unconditional support over the past few years. I have had the good fortune of being close friends with my immediate and extended family (Mom, Papa, Kathy, and Stephanie; the Josephs in Philadelphia; the Jacobs in Maryland) and having friends who feel like close family (Rick and Alex; Kayla and Carson). I have no doubt that my academic success is a privilege afforded to me by the financial, emotional, and social stability that you collectively provide. I am beyond excited to see most of you in person for my biggest birthday party yet! As you hopefully know, I will first have to present on my research accomplishments. For spoilers, please continue reading the next 100 or so pages.

Table of Contents

List of Tables ..... **iv**

List of Figures ..... **v**

Chapter 1 – Introduction to neonatal brain injury and nanotechnology **1**
1.1 Neonatal brain injury: background **1**
1.2 Neonatal hypoxic ischemia **1**
1.2.1 Pathophysiology of HI brain injury 1
Primary phase of injury *2*
Secondary phase of injury *3*
Tertiary phase of injury *3*
1.2.2 The Vannucci model 3
1.2.3 Therapeutic hypothermia, novel treatment strategies, and current challenges 4
1.3 Applications of nanotechnology in medicine **5**
1.3.1 Pediatric physiological considerations for nanotherapeutic design 5
1.3.2 Translational challenges of nanotechnology to pediatric populations 8
1.4 Overview of project chapters **8**

Chapter 2 – Methods **10**
2.1 Methods for nanoparticle formulation and *in vitro* characterization **10**
Nanoparticle formulation by the nanoprecipitation method *10*
Dendrimer, polystyrene, and quantum dot nanoparticle preparation *10*
Preparation of hydrophobic ion-pairing (HIP) complexes with catalase *11*
Nanoparticle formulation with HIP catalase complexes *11*
Characterization of particle size, polydispersity, zeta potential, and morphology *12*
Curcumin drug loading and encapsulation efficiency *12*
In-vitro drug release profile *12*
Mass spectrometry for quantification of surfactants in nanoparticle formulations *13*
Time-of-Flight secondary ion mass spectrometry (ToF-SIMS) *13*
Plasma protein adsorption study *14*
Characterization of catalase binding efficiency and mass by BCA assay *14*
Catalase activity assay *14*
2.2 Methods for nanoparticle analysis *ex vivo* **15**
Animal and ethics statement *15*
Brain slice preparation for live particle tracking studies *16*
Multiple particle tracking (MPT) *16*
Slice culturing, oxygen-glucose deprivation (OGD), and treatment *17*
Glutathione (GSH) assay *18*
Cytotoxicity analysis and slice imaging *18*
VAMPIRE for microglial morphometric analysis *19*
Nanoparticle co-localization in microglia and neurons and flow cytometry *19*
Statistical analysis *21*
2.3 Methods for nanoparticle analysis *in vivo* **22**
Animal and ethics statement *22*
Biodistribution, capillary depletion, and nanoparticle quantification *22*
Unilateral hypoxic-ischemic brain injury model in neonatal rats *23*
PLGA-PEG nanoparticle uptake across the impaired blood brain barrier *24*
Drug administration *24*
Gross injury scoring and total area loss *25*
Histopathological evaluation *26*

Immunohistochemistry *27*
Statistical analysis *28*

Chapter 3 – Curcumin-loaded polymeric nanoparticles are neuroprotective in neonatal rats with hypoxic-ischemic encephalopathy **29**
3.1 Introduction **29**
3.2 Results **29**
Preparation and characterization of curcumin-loaded nanoparticles *29*
PLGA-PEG nanoparticles can diffuse in the brain parenchyma *31*
PLGA-PEG nanoparticles can overcome the BBB and extravasate into the parenchyma of the HI brain *32*
Curcumin-loaded PLGA-PEG nanoparticle treatment reduces global injury in the Vannucci model *33*
Curcumin-loaded PLGA-PEG nanoparticle treatment does not result in region-specific neuroprotection *35*
Microglia show altered morphology following PLGA-PEG/curcumin nanoparticle treatment *38*
3.4 Discussion **39**
3.5 Conclusion **43**

Chapter 4 – Nanoparticle-microglial interaction in the ischemic brain is modulated by injury duration and treatment **45**
4.1 Introduction **45**
4.2 Results **46**
OGD time-dependent severity *46*
OGD and AZ effects on microglial shape as determined by VAMPIRE *48*
OGD enhances nanoparticle diffusion through the brain ECS *50*
Microglial uptake of nanoparticles is influenced by disease state and nanoparticle properties *53*
4.3 Discussion **57**
4.4 Conclusion **61**

Chapter 5 – Surfactant effects drive nanoparticle penetration and cellular uptake in the brain **63**
5.1 Introduction **63**
5.2 Results **64**
Surfactants and PEG enhance nanoparticle stability and diffusive ability *64*
Nonionic surfactants result in decreased cellular uptake and diffusivity ex vivo *66*
Nonionic surfactants enhance BBB permeation and accumulation in the brain *70*
Polysorbate 80 is surface-associated and influences serum protein adsorption *73*
5.3 Discussion **77**
5.4 Conclusion **81**

Chapter 6 – Catalase-loaded nanoparticles for neuroprotection against neonatal brain injury **82**
6.1 Introduction **82**
6.2 Results **83**
Effect of ion-pairing agent, molar ratio, pH, and buffer ion on complexation efficiency *83*
Effect of nanoparticle formulation method on catalase loading and protection *84*
Effect of catalase-loaded nanoparticles on brain injury severity in neonatal rats *86*
6.3 Discussion **87**
6.4 Conclusion **89**

Chapter 7 – Research summary **91**
7.1 Determining dominant driving forces affecting controlled protein release from polymeric nanoparticles **91**
7.2 Curcumin-loaded polymeric nanoparticles for neuroprotection in neonatal rats with hypoxic-ischemic encephalopathy **92**
7.3 Pharmacokinetics of nanotechnology-based formulations in pediatric populations **93**
7.4 Nanoparticle-microglial interaction in the ischemic brain is modulated by injury duration and treatment **94**
7.5 Governing transport principles for nanotherapeutic application in the brain **95**
7.6 Surfactants influence polymeric nanoparticle fate within the brain **96**
7.7 Formulation and efficacy of catalase-loaded nanoparticles for the treatment of neonatal hypoxic-ischemic encephalopathy **97**
References **98**
Curriculum Vitae **116**

List of Tables

Table 2.1 Neuropathological scoring criteria. 26
Table 3.1 Physicochemical properties of PLGA and PLGA-PEG nanoparticle loaded with curcumin. 30
Table 3.2 Outcome measures following treatment in neonatal HI rats. 36
Table 4.1 Average circularity of microglia by shape mode for a given experimental condition. . 50
Table 4.2 Physicochemical properties of PS-PEG used in MPT and nanoparticle uptake studies. 50
Table 4.3 Summary of multiple particle tracking in OGD slices. 51
Table 5.1 Physicochemical properties and diffusivity of PLGA-PEG nanoparticles formulated with biocompatible surfactants. 65
Table 5.2 Proposed chemical identifications of selected ToF-SIMS peaks from nanoparticle and P80 control samples. 74
Table 6.1 Characterization of nanoparticles loaded with HIP complexes. 85

List of Figures

Figure 1.1 Developmental changes across the pediatric age range from premature infant (<37 weeks gestation) to child/adolescent (2-16 years of age). 7
Figure 2.1 Representative FACS data from control samples. 21
Figure 2.2 Biodistribution calibration curves. 23
Figure 3.1 Curcumin release kinetics from PLGA and PLGA-PEG nanoparticles. 31
Figure 3.2 Nanoparticle diffusion within the brain parenchyma. 32
Figure 3.3 Nanoparticle uptake in regions of injury in the HI brain. 33
Figure 3.4 PLGA-PEG/curcumin effects on global brain injury and percent area loss in the HI brain. 34
Figure 4.1 OGD exposure-dependent effect on cell death and oxidative stress environment. 47
Figure 4.2 Therapeutic effects on OGD exposure-induced injury. 48
Figure 4.3 AZ reverses microglial heterogeneity and circularity after 0.5h OGD. 49
Figure 4.4 Characterization of nanoparticle diffusive behavior after OGD. 51
Figure 4.5 Supplemental geometric feature analysis of nanoparticle trajectories. 52
Figure 4.6 Microglial uptake of PS-PEG, D-Cy5, and QD nanoparticles at 5h for NC, 0.5h OGD, and 0.5h OGD+AZ conditions. 54
Figure 4.7 Supplemental analysis of microglial uptake of PS-PEG at a 100-fold increased dose. 55
Figure 4.8 Microglial number decreases after OGD and is restored with AZ. 56
Figure 5.1 Mass spectrometry analysis of surfactants P80 and CHA. 66
Figure 5.2 Supplementary assessments of nanoparticle transport in organotypic brain slices. 68
Figure 5.3 Geometric analysis of nanoparticle diffusion trajectories. 70
Figure 5.4 Distribution of biodegradable, PEGylated nanoparticles (red) in the brain and major organs at t=4h. 72
Figure 5.5 Supplementary assessments of in vivo nanoparticle localization at 4h and 24h. 73
Figure 5.6 PLGA-PEG/P80 surface analysis and serum protein adsorption. 74
Figure 5.7 Supplementary analysis: size and surface charge characterization for all nanoparticle formulations after 4-hour incubation in plasma. 76
Figure 6.1 Effect of molar ratio on catalase complexation efficiency with different ion-pairing agents. 84
Figure 6.2 Catalase loading and protection in PLGA-PEG nanoparticles by formulation method. 85
Figure 6.3 Global brain injury is significantly reduced by treatment with catalase-loaded nanoparticles. 87

Chapter 1 – Introduction to neonatal brain injury and nanotechnology

One of the fascinations of small things is that they turn out to be so alien, in spite of superficial similarities in shape or function to larger, more familiar relatives.
– George Whitesides

1.1 Neonatal brain injury: background

Perinatal asphyxia (PA), where newborns suffer from a lack of oxygen and blood flow to the brain, accounts for one of the highest numbers of disability adjusted life years for any condition [1, 2]. PA can result in the development of hypoxic-ischemic (HI) brain injury, also known as hypoxic-ischemic encephalopathy (HIE), which occurs in 1.3-4.7 per 1000 live births in developed countries, and in as many as 26 per 1000 live births in low-resource settings [3]. Without treatment, 20-50% of affected infants die within the newborn period, and up to 25% of survivors exhibit permanent neuropsychological handicaps including intellectual disability, cerebral palsy, epilepsy, or sensorineural hearing loss or vision loss, which carry a huge burden on society [4].

1.2 Neonatal hypoxic ischemia

Neonatal HI begins with a reduction in blood flow to the newborn through either the umbilical cord or placenta. Suppression of blood flow is typically associated with an acute perinatal event such as obstructed labor, placental abruption, or umbilical cord prolapse, although chronic conditions like pre-eclampsia or intrauterine infection may increase susceptibility. Low blood flow induces systemic hypoxia, which reduces cardiac output, which results in global ischemia and reduced cerebral blood flow. Although this general etiology is shared between infants with HI, the progression and outcome of injury is highly variable across individuals. Injury severity is typically classified as mild, moderate, and severe, with diagnosis occurring at birth (within 4.5-5 hours) immediately followed by treatment for moderate and severe cases. Importantly, it is not possible to predict which infants will develop HI prior to delivery, nor to predict the severity of injury once the insult has occurred. Despite advances in obstetric care, clinicians are left having to start treatment after the primary neurological injury has occurred, with the injury progressing at an unknown speed, for a poorly-defined duration of time.

1.2.1 Pathophysiology of HI brain injury

Next-generation therapies for HI will leverage disease physiology in order to target therapeutics to sites of injury and specific injury pathways of interest. Thus, it is important to understand the

role of energy failure, excitotoxicity, oxidative stress, neuroinflammation in the progression of HI. The development of HI occurs in three phases: a primary injury phase, where the insult immediately causes cell swelling, oxidative stress, and mitochondrial dysfunction; a secondary phase, where energy production briefly improves and then precipitously declines to cause causes seizures and increased cell death; followed by a tertiary phase, characterized by ongoing inflammation and excitotoxicity-induced cell death to propagate the injury [5].

Primary phase of injury

By definition, global and cerebral hypoxia and ischemia cause a dramatic reduction of oxygen and metabolic substrates in the brain. This directly induces energy failure as cells are unable to produce adequate adenosine triphosphate (ATP) through aerobic respiration, a process which requires oxygen as the terminal electron acceptor in the mitochondrial electron transport chain (ETC). The less efficient anaerobic respiration is used to partially meet cellular energy demands, but a buildup of lactate byproduct leads to lactic acidosis, a fatal condition on its own. ATP-dependent processes also begin to fail, initiating a cascade of cytotoxic activity [5].

One important ATP-dependent process is the maintenance of sodium and potassium gradients across the neuronal membrane. Failure of these gradients results in influx of sodium into the cell, which creates an osmotic gradient driving water influx as well. This leads to cellular edema and acute cell lysis. Sodium influx can also trigger action potentials leading to neuronal depolarization and release of excitatory neurotransmitters such as glutamate (“excitotoxicity”). Excess glutamate in the extracellular space is normally scavenged by astrocytes, but this recycling process is ATP-dependent and its failure creates a feed-forward cycle which exacerbates the injury. Excess glutamate and general mitochondrial failure, combined with the re-introduction of oxygen as hypoxic and ischemic conditions improve, initiate the excito-oxidative cascade [6].

The first step of the excito-oxidative cascade is glutamate overactivation of N-methyl-D-aspartate (NMDA) receptors leading to an influx of calcium into the cell. Excess calcium activates neuronal nitric oxide synthase which produces nitric oxide (NO) [7]. When oxygen is re-perfused through the brain, dysfunctional mitochondria produce reactive oxygen species (ROS) like superoxide (O_2^-), which reacts with NO to produce the peroxynitrite radical $ONOO^-$. This peroxynitrite radical can cause lipid peroxidation, protein deactivation, and DNA damage, ultimately leading to cell death by apoptosis [8]. Pro-apoptotic factors are upregulated in newborns, increasing the likelihood of cell death by apoptosis [9]. The newborn brain is especially susceptible to ROS damage due to relatively immature antioxidant defenses and a

reduced ability to regenerate antioxidants in HI conditions [10, 11]. Additionally, compared to adults, the newborn brain overexpresses NMDA receptors, has a lower threshold for NMDA receptor activation, and is open for longer once activated [12]. Thus, glutamate excitotoxicity is a critical intervention point for neonatal brain injury.

Secondary phase of injury

As blood flow and oxygenation return to the body and brain, cells improve their ATP production and a “latent” period begins [13, 14]. The degree of injury from the HI insult is highly correlated to function in this 24-48h period [14, 15]. Function is correlated with degree of mitochondrial activity as well as the body’s ability to supply metabolic substrates [16-20]. Ultimately, cells must be able to match energy production with metabolic demand. Near the end of the latent period, glutamate levels increase again, bringing with it a secondary energy failure [21]. A large inflammatory response is initiated, the blood-brain barrier (BBB) breaks down, and seizures and secondary edema may develop [21]. At this point, it is generally thought to be too late for therapeutic intervention [22].

Tertiary phase of injury

The cycle of excitotoxicity, oxidative stress, and cell death present in early phases of HI provokes a delayed inflammatory response which may persist for weeks or months after birth [23]. The neuroinflammatory response recruits leukocytes to the brain and activates local microglia and astrocytes [24]. Glial cell activation initiates changes in cell phenotype and function [25-28]. For example, microglia proliferate and migrate to sites of injury, as well as becoming extra-phagocytic for the clearance of cellular debris [25, 29-33]. Activated astrocytes also proliferate and undergo glial scarring to isolate and contain damaged areas [34, 35]. Both astrocytes and microglia lose their neuroprotective functions once activated [36], and when tissue damage overwhelms the immune response, a chronic state of neuroinflammation is sustained [37]. Several promising therapies for HIE have anti-inflammatory or immune-modulating properties, suggesting that prevention or augmentation of the neuroinflammatory response may be an ongoing therapeutic target [38-40].

1.2.2 The Vannucci model

The most widely-utilized model of neonatal HI brain injury is the Vannucci model of unilateral HI in rodents. Initially described in the adult rat by Seymour Levine [41], the model was translated

to neonatal rats [42] and has been optimized to be the model now used ubiquitously in the HIE field [43]. The etiology of HIE is thought to be largely due to the combined effects of reduced oxygen delivery to the brain (hypoxia) and a concurrent fall in cardiac output or cerebral blood flow (ischemia). In the postnatal day 7 (P7) rat HI model, the cerebral structures most likely to be damaged are the hippocampus, cortex, striatum, and thalamus [44], depending on the severity of insult [42, 45-47]. These patterns of injury in the P7 rat are broadly comparable to injury patterns seen in infants with HIE [48, 49]. In general, the non-ligated side of the brain remains largely undamaged, outside of very severe injury [45]. Loss of ipsilateral hemispheric volume relative to the contralateral side correlates closely with both sensorimotor function and more formal pathology scores [46, 50]. In addition, this model has shown suppression of electroencephalogram power with continued seizure activity up to 48h after insult, which is often seen in infants with HIE [51-53]. The Vannucci model was used to develop the therapeutic hypothermia (TH) treatment, which has been the standard of care since 2010 [54-57]. The successful translation of TH makes the Vannucci model a valuable tool to understanding the pathophysiology of HI and developing novel treatments.

1.2.3 Therapeutic hypothermia, novel treatment strategies, and current challenges

Currently, TH is the only clinically-implemented treatment that has been shown to provide robust improvement in outcome in asphyxiated term newborn infants who develop moderate or severe HIE [54]. TH, in which either the head or whole body is cooled to 33-34°C for 72 hours, is thought to slow injury and promote recovery through several mechanisms. First, cerebral metabolic rate decreases 5% per 1°C drop in temperature, resulting in reduced ATP demand and therefore a reduced degree of energy failure [58, 59]. Cooling is also anti-inflammatory [60-62] and anti-apoptotic [61-64]. However, TH only provides a 15% risk reduction in death and disability, and 40-50% of infants treated with TH are still likely to have a poor outcome [54, 65]. There is also evidence that TH may harm infants born with certain co-morbidities such as infections or bleeding [66, 67].

Other neuroprotective agents like xenon, tetrahydrobiopterin, N-acetyl cysteine (NAC) and erythropoietin (Epo) have been studied in either, or both, preclinical and clinical trials as an adjuvant to TH [68, 69]. Many of these therapies, for instance NAC and Epo, appear to be neuroprotective due to the fact that they have broad-spectrum activities, including anti-inflammatory and antioxidant effects. However, high doses of these drugs are usually needed to have these effects [40, 70]. Nonetheless, these treatment strategies are often combined with TH due to the fact they do not outperform TH [71], and none of these therapies are currently

curative. Thus, additional interventions during this critical period may reduce the severity of ongoing brain injury [72]. Strategies that can improve drug delivery and efficacy, providing better neuroprotection, are necessary to address this critical need.

1.3 Applications of nanotechnology in medicine

Nanoparticles have been proposed as a means to improve drug delivery efficiency, reduce off-site effects, provide sustained drug release, and allow delivery of a diverse range of therapeutics [73]. Polymeric nanoparticles have additionally demonstrated an ability to overcome barriers to drug delivery in the brain, including the highly selective BBB and a tightly regulated extracellular space (ECS). Among the variety of polymers that can be used as delivery vehicles for treatments of neurological disorders, some of the most promising are those made of poly(lactic-*co*-glycolic acid) (PLGA). For example, PLGA nanoparticles coated with polysorbate 80 (P80) surfactant facilitated the delivery of a number of drugs that are unable to cross the BBB in free form [74]. PLGA nanoparticles have improved delivery of therapeutics to glioma [75], Alzheimer's disease [76, 77], glaucoma [78], traumatic brain injury [79], and other diseases of the central nervous system [79-81]. At the disease site, cell-specific delivery can be achieved by surface modifications on the PLGA polymer with targeting ligands, surfactants, or cell-penetrating peptides [82]. After crossing the BBB, the challenge of penetrating the brain parenchyma to diffuse long distances to reach diseased cells must also be overcome before those cells can be targeted. Dense poly(ethylene glycol) (PEG) surface coatings have been shown to improve polymeric nanoparticle diffusion in the brain parenchyma [83] in addition to increasing stability, solubility [84, 85], and circulation time of the nanoparticle system [86]. However, most nanotherapeutic studies investigate adult disease. As outlined in the following subsections, neonatal and pediatric physiology is substantially different from the adult, which can affect nanoparticle and drug behavior.

1.3.1 Pediatric physiological considerations for nanotherapeutic design

Upon systemic administration into the body, nanotherapeutic formulations undergo absorption, distribution, metabolism, and elimination (ADME). The most dramatic physiological changes affecting ADME of nanotherapeutics occur in the infant and toddler ages; these are briefly outlined here and are summarized in Figure 1.1. During the neonatal period, absorption of nanotherapeutics is affected by relatively high gastric pH, with a pH of 4.6 in the first week of life compared to an adult range of 1.5-3.5. There is also an increased gastric emptying rate at 75 min in neonates compared to 45 min in adult males and 60 min in adult females for calorie-

containing liquids [87]. In the intestinal lumen, permeability is generally increased due to the immaturity of the mucosa, but transport systems are also immature, so some transporter-mediated interactions can limit therapeutic absorption [88]. The gut microbiome is highly variable, ranging from completely sterile at birth, to some colonization within 4-8 hours, to adult levels in adolescence [88]. However, factors like whether the infant drinks maternal or artificial milk can influence the microbial composition, increasing observed variability of intestinal permeability at young ages [89]. The relationship between the gut microbiome and intestinal permeability has been covered extensively [90-92]. Developmental changes also affect adsorption after alternative routes of nanotherapeutic administration, such as transdermal [93], oral transmucosal [94], rectal [95], and intrapulmonary [96].

Nanotherapeutic distribution is specifically affected in infants due to proportionally higher body water, with 80-90% body weight (BW) compared to 55-60% BW in adults, and lower body fat, at 10-15% BW compared to 11-20% in adult men and 16-30% in adult women [88]. One consequence of this is relatively high volumes of distribution of water-soluble drugs. For example, gentamicin has a volume of distribution of 0.5-1.2 L/kg in infants compared to 0.2-0.3 L/kg in adults [88]. Metabolism is typically dissimilar between children and adults, and importantly, the cytochrome enzymes responsible for metabolism are immature from birth to approximately 2 years of age [97]. In general, children have higher rates of hepatic clearance than adults, resulting in higher dosages by weight. However, since the maturation of metabolic enzymes is not linear, doses must be carefully determined based on a drug's metabolic pathway and the developmental age of the patient [89, 98, 99]. Broad physiological differences including increased ventilation rate, increased cardiac output, and increased body surface area to weight compared to adults, can further impact the distribution and elimination of pediatric formulations [88]. Babies and children are not "little adults"; the development of novel therapeutics for this patient population must specifically take into account their distinct physiology.

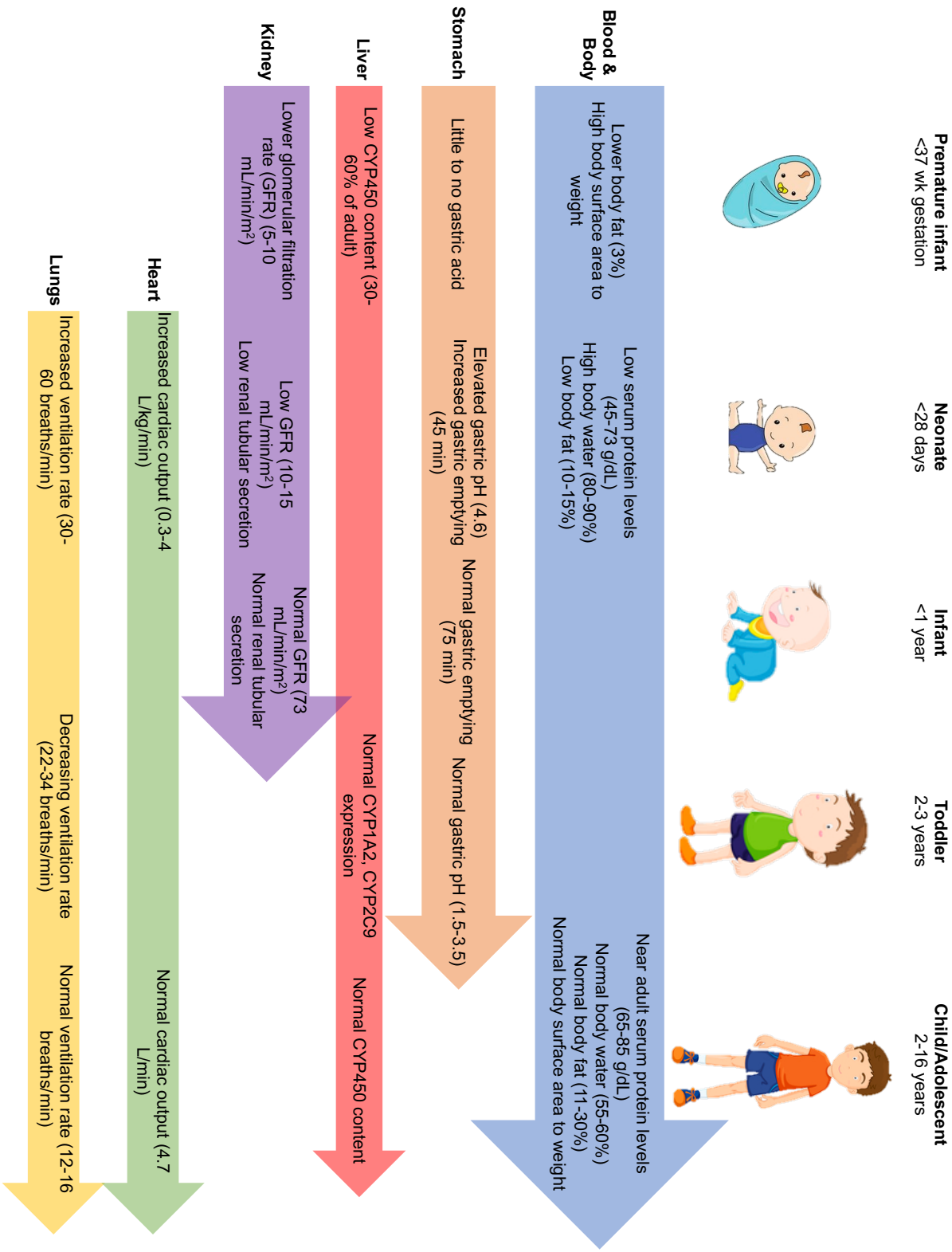

Figure 1.1 Developmental changes across the pediatric age range from premature infant (<37 weeks gestation) to child/adolescent (2-16 years of age).
Changes in blood and body composition, and stomach, liver, kidney, heart, and lung physiology are summarized.

1.3.2 Translational challenges of nanotechnology to pediatric populations

Potential advantages of nanotechnology for pediatric formulations are similar to adult formulations and include improved drug targeting to specific tissues of interest, controlled and sustained release medications to reduce dosing frequency, increased solubility of lipophilic or otherwise insoluble therapeutic agents, and enhanced bioavailability [100]. Nanotechnology-based drug delivery platforms beneficially alter the pharmacokinetics (PK) of drugs and result in a different dose-response relationship when compared with the drug itself. However, nanoparticle formulation development for the pediatric population is challenging because of the patient group's heterogeneity and dissimilarity to adults. Due to their distinct physiology, pediatric patients experience different medicine-related toxicities compared to adults [101, 102] and often both active drug and formulation excipients (such as nanomaterials) have different bioactivity in children [103]. Dosing challenges are exacerbated by rapid growth and development during childhood, with doses of certain formulations varying 100-fold during this period [104-106]. The lack of PK data in pediatrics compounds the problem of a lack of age-appropriate formulations, leading to off-label use of drugs by clinicians and resulting in increased risk of toxicity or sub-therapeutic dosing [107].

To overcome the challenges of heterogeneity in patient population, disease progression, and pathology, we can look towards the example of dendrimer-NAC (D-NAC) nanoparticles for the treatment of cerebral adrenal leukodystrophy. This is the only nanoformulation to date which has been successfully translated to the pediatric population. Before clinical investigation, D-NAC was evaluated in eight separate models of inflammation-mediated disease—in mice, rabbits, and dogs—accounting for sex differences and developmentally appropriate ages in each model [108]. Looking forward, it is clear that increased study of nanoformulations in pediatric models is necessary for the development of safer and more effective therapeutics for this age group. The work in this thesis supports that overarching goal.

1.4 Overview of project chapters

In Chapter 2, the methods used for the thesis are summarized. These methods cover nanoparticle formulation and their characterization *in vitro*, *ex vivo*, and *in vivo*, with appropriate statistical analysis.

In Chapter 3, curcumin is introduced as a broad-acting therapeutic with potential to be neuroprotective after HI injury. A PLGA-PEG nanoformulation is used to increase drug solubility, extend drug release, enhance uptake across the BBB, and deliver drug to sites of injury. Gross

injury and area loss measurements show a significant neuroprotective effect of the nanotherapeutic, which is demonstrated on a cellular level by the return of partially healthy microglial morphology in PLGA-PEG/curcumin treated brains.

In Chapter 4, nanoparticle diffusion and uptake into brain cells is assessed in an *ex vivo* brain slice model of hypoxic-ischemic injury. Nanoparticles are successfully used to probe disease-mediated extracellular changes in the brain microenvironment. Further, nanoparticle uptake into microglia is found to be a consequence of both disease state and nanoparticle physicochemical properties.

In Chapter 5, the polymeric nanoformulation is optimized for brain penetration by the incorporation of surfactants, which are commonly used to promote the formulation and stabilization of nanoparticles. The surfactant P80 is shown to significantly improve nanoparticle penetration of the blood-brain barrier and uptake into brain cells, while retaining diffusivity in the brain extracellular space.

In Chapter 6, the PLGA-PEG/P80 formulation is used for the delivery of catalase, an antioxidant enzyme, after HI injury. Given catalase's large and hydrophilic nature, a hydrophobic ion-pairing technique was used to improve its loading into the nanoparticle core. The resulting nanoformulation demonstrated high protein activity with relatively low mass loading and sustained enzyme protection in degradative conditions. Finally, these nanoparticles were found to be neuroprotective in the Vannucci model of HI injury.

In Chapter 7, the thesis research and other manuscript contributions are summarized.

Chapter 2 – Methods

Truth has nothing to do with the conclusion, and everything to do with the methodology.
– Stefan Molyneux

2.1 Methods for nanoparticle formulation and *in vitro* characterization

Nanoparticle formulation by the nanoprecipitation method

Nanoparticles in Chapters 3 and 5 were formed by nanoprecipitation. A polymer solution (organic phase) was added dropwise into 25 mL aqueous solution where nanoparticles formed spontaneously and were stirred for 3h at 700 rpm to remove the organic solvent. The organic solvent was further removed with rotary evaporation (Buchi Rotavapors, Buchi Corporation, New Castle, DE) under reduced pressure (15 mbar) at 4ºC for 30 min. Nanoparticles were collected and washed twice by ultracentrifugation with deionized (DI) water at 100,000xg for 25 min. Finally, the nanoparticles were resuspended in 1 mL DI water, or in sterile 1x phosphate buffered saline (PBS) for animal experiments. For fluorescently-labeled nanoparticles, the same nanoparticle formulation procedure was used with PLGA and PLGA-PEG and conjugation of AlexaFluor 555 (AF555), AlexaFluor 647 (AF647), or CF647 dye was achieved by attachment to the free COOH on the PLGA backbone, as described previously [83].

In Chapter 3, PLGA-PEG or PLGA polymers were dissolved with curcumin in acetone at a concentration of 20 mg/mL polymer and 2 mg/mL curcumin. The aqueous sink was 1% F127.

In Chapter 5, PLGA-PEG (20 mg/mL) was added to one of the following aqueous solutions: 1% P80, 5% polyvinyl alcohol (PVA), 1% Pluronic F127 (F127), 5% Pluronic F68 (F68), 3% cholic acid (CHA), or no surfactant in deionized water.

Dendrimer, polystyrene, and quantum dot nanoparticle preparation

Dendrimer, polystyrene (PS), and quantum dot (QD) nanoparticles were used in Chapter 4. 40nm dark red fluorescent carboxylate-modified PS latex nanoparticles (PS-COOH) (Thermo Fisher) were covalently modified with methoxy-PEG-amine (NH_2) (5kDa MW, Creative PEG Works) by a carboxyl amine reaction [109]. Generation-4 hydroxyl modified PAMAM dendrimers labeled with Cy5 (D-Cy5) were provided by Dr. Rangaramanujam Kannan and Dr. Anjali Sharma at the Johns Hopkins University Center for Nanomedicine [110, 111]. These conjugates are stable at physiological conditions and have been validated for *ex vivo* application at the concentration used in our study (1 ng/μL) [112]. CdSe/CdS core-shell QDs with PEG-methoxy functionality were provided by Dr. Vince Holmberg in the UW Department of Chemical Engineering, which were proven stable at physiological conditions for *ex vivo* application [113].

Preparation of hydrophobic ion-pairing (HIP) complexes with catalase

HIP complexes of catalase were prepared prior to catalase nanoparticle formulation in Chapter 6. Stocks of ion-pairing agent was made in DI water: 20 mM dextran sulfate (DS, M_r 5000), 250 mM sodium dodecyl sulfate (SDS), and 500 mM taurocholic acid (TA). 50 mM phosphate buffer was adjusted to pH 4.7 with 0.1 N HCl and then used to dissolve catalase at a 10 mg/mL concentration. Based on molar ratio, an appropriate volume of ion-pairing agent (less than 25 µL) was slowly added to the catalase solution, spontaneously forming HIP complexes. The solution was vigorously vortexed for 1 min followed by centrifugation at 12,000 rpm for 15 min at 4ºC. Uncomplexed catalase in the supernatant was measured by bicinchoninic (BCA) assay. Pelleted HIP complexes were lyophilized into powder and stored at 4ºC.

The above procedure was modified appropriately for individual experiments: The catalase solution pH was adjusted to 4.2, 5.2, and 7.0 for the pH variation study. 10 mM citrate buffer was used instead of phosphate buffer to determine the effect of buffer ion species. For bovine serum albumin (BSA) complexes used as a non-therapeutic control, BSA (ThermoFisher) was dissolved in citrate buffer at pH 3.7 prior to the addition of ion-pairing agent.

Nanoparticle formulation with HIP catalase complexes

Nanoparticles in Chapter 6 were formed by either solid/oil/water (S/O/W) emulsion or nanoprecipitation. To formulate nanoparticles by S/O/W emulsion, 1 mL of 25 mg/mL PLGA45k-PEG5k (LA:GA 50:50, Akina) dissolved in dichloromethane (DCM, Fisher Scientific) was added to 1 mg lyophilized catalase HIP complexes. The mixture was emulsified with a Sonic Dismembrator Ultrasonic Processor (Fisher Scientific) using 20 kHz probe sonication at 30% amplitude with 1s on:1s off pulses for 30s on. After adding 4 mL 3% cholic acid (Millipore Sigma) in DI water, the second sonication was performed at 20% amplitude with 1s on:1s off pulses for 30s on. This emulsion was then poured into 25 mL beaker of 1% P80 and stirred for 3h at 500 rpm to remove the organic solvent. Nanoparticles were collected and washed twice by ultracentrifugation with phosphate buffer at 100,000xg for 25 min. Finally, the nanoparticles were resuspended in 1 mL DI water. Nanoparticles were used immediately or stored at 4ºC for a short time.

To formulate nanoparticles by nanoprecipitation, 1 mg lyophilized catalase or BSA complexes were dissolved in 0.3 mL dimethyl sulfoxide (DMSO). 25 mg PLGA-PEG was dissolved in 0.7 mL acetone. The two solutions were quickly vortexed together before being

added dropwise into 25 mL 1% P80. The remainder of the procedure was as described above. For animal experiments, catalase and BSA nanoparticles were resuspended in sterile PBS.

Characterization of particle size, polydispersity, zeta potential, and morphology

For nanoparticles formulated in all chapters, size and polydispersity index (PDI) were measured by dynamic light scattering (DLS), and the zeta potential was determined using a zeta potential analyzer (NanoSizer Zeta Series, Malvern Instruments, Malvern, UK). Samples were diluted to appropriate concentrations to obtain accurate measurements in 10 mM sodium chloride, pH 7.4, as described previously [114].

For scanning electron microscopy in Chapter 3, nanoparticles were resuspended in DI water and diluted 100-fold in ethanol. Subsequently, 100 µL of the diluted nanoparticle solutions were pipetted onto a silicon wafer and allowed to air-dry for 1h in a fume hood. The nanoparticles were sputter coated with palladium under an argon environment and imaged on the FEI XL830 Dual Beam Focused Ion Beam/Scanning Electron Microscope in the UW Molecular Analysis Facility.

Curcumin drug loading and encapsulation efficiency

In Chapter 3, drug loading and encapsulation efficiency of curcumin-loaded nanoparticles were determined by ultraviolet-visible light spectrometry (UV-Vis) compared to a standard calibration curve of curcumin in DMSO. Each sample's absorbance at 430 nm was measured and adjusted by subtracting a blank of unloaded polymer nanoparticles' absorbance in DMSO. The weight of polymer and drug was determined by lyophilizing the nanoparticle sample. Drug loading and encapsulation efficiency are defined as follows:

$$\%\ \text{Drug Loading} = \frac{\text{weight of drug encapsulated in NP}}{\text{weight of polymer and drug in NP}}$$

$$\%\ \text{Encapsulation Efficiency} = \frac{\text{weight of drug encapsulated in NP}}{\text{weight of drug used in formulation}}$$

In-vitro drug release profile

In Chapter 3, curcumin release from PLGA-PEG/curcumin and PLGA/curcumin nanoparticles was measured over 24h. Nanoparticles were resuspended in 1 mL 1xPBS and then evenly distributed to three dialysis tubes made of cellulose ester (MWCO: 300kDa, Spectrum Laboratories, Inc.). The membranes were submerged in 20 mL 1xPBS containing 1% P80 and placed on a shaker at 60 rpm at 37ºC. At 1h, 2h, 4h, 8h, and 24h of incubation, the membranes

were transferred to fresh 20 mL of 1% P80 in 1xPBS. In the supernatants collected at each time point, curcumin content was determined by UV–Vis compared to a calibration curve of curcumin in the 1xPBS 1% P80 solution. Percent curcumin released from the nanoparticles was defined as the curcumin amount released at a specific time point divided by the total curcumin encapsulated in the nanoparticles.

Mass spectrometry for quantification of surfactants in nanoparticle formulations

High performance liquid chromatography (HPLC)-mass spectrometry (MS) was used to quantify surfactant amounts in nanoparticles formulated in Chapter 5. Standard solutions of each surfactant were injected into a triple quadrupole LC-MS/MS system (AB Sciex 5600 QTOF) equipped with a Waters BEH column (50 mm, 2.1x150 mm). Surfactant was eluted using two mobile phases, HPLC-grade water and acetonitrile at 0.3 mL/min and identified on the chromatogram by molecular weight. For surfactants P80 and CHA, where a sample peak was identified, a calibration curve from standard solutions was created and used to determine the amount of surfactant present in PLGA-PEG/P80 and PLGA-PEG/CHA, respectively. For surfactants F68, F127, and PVA, no sample peak could be identified.

Time-of-Flight secondary ion mass spectrometry (ToF-SIMS)

In Chapter 5, ToF-SIMS was used to confirm surfactant presence on the nanoparticle surface. ToF-SIMS spectra were acquired on a IONTOF ToF-SIMS 5 spectrometer using a 25 keV Bi_3^+ cluster ion source in the pulsed mode. Spectra were acquired for both positive and negative secondary ions over a mass range of m/z = 0 to 800. The ion source was operated at a current of 0.2 pA. Secondary ions of a given polarity were extracted and detected using a reflectron time-of-flight mass analyzer. Spectra were acquired using an analysis area of 100 micron x 100 micron. Positive ion spectra were calibrated using the CH_3^+, $C_2H_3^+$, and $C_3H_5^+$ peaks. The negative ion spectra were calibrated using the CH^-, OH^-, C_2H^-, and C_4H^- peaks. Calibration errors were kept below 25 ppm. Mass resolution (m/Δm) for a typical spectrum was between 5000 to 5600 for m/z = 27 (pos) and between 4000 to 6500 for m/z = 25 (neg). PLGA-PEG/DI nanoparticle, surfactant and PLGA-PEG/surfactant samples were drop cast on cleaned silicon wafers. 5 positive and 5 negative ion spectra were collected from random positions on each sample. Sample preparation and data acquisition was repeated on two separate dates for a total of 10 positive and 10 negative ion spectra per sample type. The positive and negative ion data were analyzed separately to generate a peak list across all spots on all samples. The peak area tables were imported into the NBToolbox spectragui (https://www.nb.uw.edu/mvsa/nbtoolbox)

and used to create a peak ratio A/(A+B) where A = sum of all P80 peaks and B = sum of all nanoparticle peaks.

Plasma protein adsorption study

In Chapter 5, nanoparticles formulated with surfactants were incubated in plasma to assess differences in protein adsorption. Plasma was collected from P9 rat pups by collecting blood into a heparin-coated tube and then centrifuging out cells at 2000xg for 10 min. 100 µL of each PLGA and PLGA-PEG nanoparticles were mixed well with 900 µL plasma and then left in a 37°C incubator. 4h later, 5 µL of the protein/nanoparticle solution was diluted in 995 µL 10 mM NaCl for DLS characterization as described above. Then, nanoparticles were pelleted by centrifugation at 100,000xg for 25 min to remove non-adsorbed protein. The samples were then tested for protein concentration with the Pierce BCA Protein Assay Kit (ThermoFisher) as described above.

Characterization of catalase binding efficiency and mass by BCA assay

In Chapter 6, catalase was quantified in the HIP complexation process and in nanoparticles. HIP binding efficiency was measured indirectly by measuring protein concentration in the initial solution and supernatant using the Pierce BCA Protein Assay Kit (ThermoFisher) as described above. Percentage binding efficiency was calculated according to the following equation:

$$\text{Binding efficiency} = \frac{(\text{initial-supernatant})}{\text{initial}} \times 100\%$$

For the quantification of catalase mass in nanoparticles, 100 µL of catalase-loaded nanoparticles was combined with 50 µL of 1 M sodium hydroxide (ThermoFisher). The solution was vortexed for 2s, spun down on a minicentrifuge, and then incubated at 37 °C for 30 min for base-catalyzed hydrolysis of the PLGA polymer to release all loaded catalase. 50 µL PBS was then added to neutralize the solution, which was then measured according to the BCA assay kit.

Catalase activity assay

Catalase nanoparticles in Chapter 6 were evaluated for catalase activity using a catalase spectrophotometric assay adapted from Beers and Sizer [115]. A pH 7.0 solution of 0.036% w/w H_2O_2 (Sigma) was prepared in 50 mM phosphate buffer with a 240-nm absorbance (A_{240}) between 0.48 and 0.52. In an optically clear quartz cuvette (Hellma Analytics), 100 µL of catalase sample was added to 2.9 mL of H_2O_2 solution, mixed via pipetting, and A_{240} was measured at 2s intervals for 3 min using a kinetic spectrometric reading on a SpectraMax M5

UV–Vis Spectrophotometer (Molecular Devices). The active units per mL of catalase solution (freely dissolved or encapsulated in nanoparticles) were calculated using the following equation:

$$\text{Active units/mL} = \frac{(3.45)(\text{dilution factor})}{(\text{time})\times 0.1}$$

In the equation, 3.45 represents the decomposition of 3.45 μmol H_2O_2 during A_{240} decrease from 0.45 to 0.4 and 0.1 is the mL volume of sample added. This assay measures catalase activity even when the enzyme is encapsulated, due to the ability of H_2O_2 to diffuse throughout the polymer matrix [116]. Stock catalase had 2000-5000 AU/mg catalase.

To evaluate catalase protection in the nanoparticle polymer matrix, nanoparticles were incubated in PBS with 0.2 wt% pronase (pronase from *Streptomyces griseus*, Sigma). Aliquots were collected at 0h, 1h, 2h, 4h, and 24h, and immediately tested for catalase activity. Enzyme activities were calculated as the sample activity at a given timepoint divided by the initial sample activity at 0h.

2.2 Methods for nanoparticle analysis *ex vivo*

Animal and ethics statement

Ex vivo animal studies in Chapters 3-5 were performed in strict accordance with the recommendations in the Guide for the Care and Use of Laboratory Animals of the National Institutes of Health. All of the animals were handled according to approved Institutional Animal Care and Use Committee (IACUC) protocols (#4383-01 and #4383-02) of the University of Washington, Seattle, WA, USA. The University of Washington has an approved Animal Welfare Assurance (#A3464-01) on file with the NIH Office of Laboratory Animal Welfare (OLAW), is registered with the United States Department of Agriculture (USDA, certificate #91-R-0001), and is accredited by AAALAC International. Every effort was made to minimize suffering. Time-mated pregnant female Sprague–Dawley rats (virus antibody-free CD® (SD) IGS, Charles River Laboratories, Raleigh, NC, USA) were purchased and arrived on estrous (E) day 17. Dams were housed individually and allowed to acclimate to their environment for a minimum of 3 days prior to delivering. The day of birth was defined as P0. Litters containing both sexes were cross-fostered and culled to 12 animals early after birth. Before and after the experiment, each dam and her pups were housed under standard conditions with an automatic 12h light/dark cycle, a temperature range of 20–26°C, and access to standard chow and autoclaved tap water ad libitum. The pups were checked for health daily.

Brain slice preparation for live particle tracking studies

Brain slices for Chapters 3-5 were prepared from P9-14 rat pups, as previously described [112]. Normal rats were sacrificed and brains quickly removed under sterile conditions. Fresh 300 μm thick brain slices were prepared using a tissue chopper (McIlwain, Ted Pella, Inc, Redding, CA) and surgical dissecting scope. Slices were placed onto 30-mm, 0.4-μm-pore-sized cell culture membrane inserts. The membranes were then placed in 35-mm plates containing 1 mL culture medium consisting of 50% minimal essential media, 50% Hanks Balanced Salt Solution (HBSS), 1% GlutaMAX, and 1% penicillin. The cultures were maintained at 37°C, with constant humidity and 95% air and 5% CO_2.

Multiple particle tracking (MPT)

MPT was used in Chapters 3-5 to evaluate diffusive ability of PLGA, PLGA-PEG, and PS-PEG in the living brain [83, 117, 118]. In Chapters 3 and 5, fresh brain slices were used; in Chapter 4, slices were cultured for 3 days and subgroups were exposed to oxygen-glucose deprivation prior to MPT. Before tracking, slices were transferred to 35 mm glass bottom imaging disks and 2 μL of AF555-labeled PLGA and PLGA-PEG particles were injected directly into brain tissue. Visualization of the nanoparticles was accomplished with the excitation/emission spectra specific to AF555 in two different general brain regions, the cortex and thalamus. Five 6.5 s videos were collected per slice at 10 Hz and 40x magnification via fluorescent microscopy with a cMOS camera (Hamamatsu Photonics Corporation, Bridgewater, NJ) coupled with a confocal microscope (Nikon Instruments, Inc, Melville, NY). Trajectories were calculated via MOSAIC MPT (Chapter 3) or TrackMate (Chapters 4 and 5) ImageJ plugin, and geometrically-averaged precision-weighted mean squared displacements (MSD) were calculated via a self-developed Python package. Effective diffusion coefficients for each particle type in each brain region were then extracted from MSD data and an average diffusivity of the particle type was obtained from a weighted average of the two brain regions. At least 50 particles were tracked per sample, with n=3 independent brain samples per particle type.

In Chapters 4 and 5, selected trajectory features, described below, were extracted [119]. First, geometrically-averaged precision-weighted MSDs were calculated for each trajectory and timestep using the equation:

$$\langle r^2 \rangle = \frac{1}{N-1} \sum_{i=0}^{N-n-1} |x_{i+N} - x_i|^2$$

where r^2 indicates the MSD determined at each step, n, for a total number of steps, N, with 3D position coordinates x(x,y,t). Then, diffusion coefficients, D, and the anomalous diffusion coefficient (D_{eff}), alpha, were determined by fitting MSD curves to the function:

$$<r^2(n)> = 4D(n\Delta t)^{\alpha}$$

Alpha values of 1 indicate normal diffusive behavior, while values below 1 indicate subdiffusion and values above 1 indicate superdiffusion. The MSD ratio, which characterizes the shape of the MSD curve, is defined by:

$$<r^2>_{n_1,n_2} = \frac{<r^2(n_1)>}{<r^2(n_2)>} - \frac{n_1}{n_2}$$

where n_1 and n_2 represent the first and last frames of the trajectory, respectively. Ratios below 0 indicate restricted diffusion (subdiffusion) while ratios above 0 indicate superdiffusion. Trajectory efficiency (E), a measure of the nanoparticle's net displacement compared to the sum of its step lengths, was calculated by the equation:

$$E = \frac{|x_{N+1} - x_0|^2}{\sum_{i=1}^{N-1} |x_i - x_{i-1}|^2}$$

The fractal path dimension (D_f), which can distinguish between confined and random walk trajectories, was calculated from:

$$D_f = \frac{\log(N)}{\log(NdL^{-1})}$$

where d is the largest distance between any two positions and L is the sum of all step lengths. Fractal dimension values of 2 indicate random walk trajectories and values above 2 indicate confined diffusion. Finally, trappedness (p_t), the probability that a particle with diffusion coefficient D and traced for a period of time $N\Delta t$ is trapped into a region r_0, is given by:

$$p_t = 1 - \exp\left(0.2048 - 0.25117\left(\frac{DN\Delta t}{r_0^2}\right)\right)$$

All calculations were done in Python using a package available on GitHub [120].

Slice culturing, oxygen-glucose deprivation (OGD), and treatment

Slices for Chapter 4 were prepared as described above. For glutathione (GSH) and flow cytometry studies, three brain slices were plated per membrane insert. For all other experiments, 1 brain slice was plated per membrane insert. After slices rested overnight in the incubator, media was removed and fresh media was added, followed by two more days of rest. Samples underwent OGD after 3 days *in vitro* (DIV), except for flow cytometry studies, which underwent 2 DIV. The end of the OGD incubation period was defined as time t=0h. For the

normal control (NC) condition, slices proceeded directly to t=0h without OGD media exchange. For a subset of groups, 100μL 1x PBS containing 0.1mg superoxide dismutase (SOD, Cu/Zn SOD1 from bovine erythrocytes, Sigma) or 0.75μg (150mg/kg brain tissue) AZ (Zithromax) per slice was added directly to the 3h and 0.5h OGD slices, respectively. 6-well plates were returned to the CO_2 incubator until further processing.

Glutathione (GSH) assay

Slices in Chapter 4 were tested for GSH as an assessment of oxidative stress. At t=24h for all sample conditions, brain slices were frozen at -80°C for GSH detection with the GSH/GSSG ratio detection assay kit fluorometric green (Abcam). Three brain slices approximating 15g of brain tissue were processed for each sample. Samples were processed following the manufacturer's instructions and analyzed for fluorescence at 490/520 excitation/emission on a Cytation 3 UV-Vis Spectrophotometer (BioTek Instruments) to measure the extent of thiol green indicator reaction with GSH. Adjusting for volume resuspension and dilutions, GSH concentrations were reported as μmoles GSH per gram of initial brain tissue.

Cytotoxicity analysis and slice imaging

Slices in Chapter 4 and 5 were stained with 5μg/mL propidium iodide (PI), fixed, and stained with 4′,6-diamidino-2-phenylindole (DAPI, Invitrogen, 1:10,000). Slices were imaged using a Nikon A1R with a 40x objective. For every slice, five images were acquired from each brain region of interest (cortex and thalamus). Image acquisition settings were consistent for all images. For each image, DAPI-positive cells (total cells) and PI-positive cells (dead cells) were counted manually in ImageJ after applying an Otsu threshold and fluorescent cutoff to aid in visualization. The PI-positive/DAPI-positive cell ratio was expressed as the percentage of dead cells in an individual image. Immunofluorescence staining for microglia was done with goat anti-Iba1 antibody (Wako 019-19741, 1:200) and anti-goat AlexaFluor 488 (Life Technologies A11034, 1:500). Microglia images were analyzed using an adaptation of Visually Aided Morpho-Phenotyping Image Recognition (VAMPIRE) as described below [121]. Image acquisition and analysis was performed in a blinded manner.

Slice health was measured in Chapter 5 by lactase dehydrogenase (LDH) release. 4h after nanoparticle treatment, slice media was collected and flash frozen. For LDH cytotoxicity analysis, media samples were thawed to room temperature and LDH assays (Cayman Chemical) were conducted according to the manufacturer's protocol. 100 μL of the sample was added to 100 μL of LDH reaction buffer in triplicate to 96-well plates on ice and the plates were

gently shaken in a 37°C incubator. After 30 min, the plates were returned to the ice and then measured by UV-Vis (SpectraMax M5, Molecular Devices) for absorbance at 490 nm. Percent cytotoxicity was calculated as the sample absorbance normalized to the 4h absorbance of the Triton-X condition x100%.

VAMPIRE for microglial morphometric analysis

All confocal microscopy images were converted from the .nd2 to .tiff. Using Python, all images were separated by RGB channel and labeled with the appropriate cell stain: DAPI for the blue channel and Iba1 for the green channel [122-124]. Every image was then split into four quadrants using Image_slicer. Scikit-learn was used to split all images in an 80:20 test-to-train ratio [125], assuring at least two images for each slice of the three experimental conditions: NC, 0.5h OGD, and 0.5h OGD+AZ. Cells from each image were segmented using the Cell Profiler pipeline associated with the VAMPIRE package [126]. Five shape mode models were built from all training images using the VAMPIRE package and associated protocol (https://github.com/kukionfr/VAMPIRE_open) [121], and then applied to all images. Shape mode frequencies of individual slices were averaged for resulting distribution plots. Equation 1 was used to calculate the difference in sample shape mode frequency from NC shape mode frequency:

$$\text{Absolute difference} = |x_n - x_{NC,n}|$$

where n is shape mode (1 through 5), x_n is sample frequency for shape mode n, and $x_{NC,n}$ is NC frequency for shape mode n. Circularity was calculated with equation 2:

$$\text{Circularity} = \frac{4\pi A}{P^2}$$

where A is area and P is perimeter for each microglia.

Nanoparticle co-localization in microglia and neurons and flow cytometry

To probe nanoparticle interactions with brain cells *ex vivo*, nanoparticles were topically pipetted on organotypic whole hemisphere slices. In Chapter 4, PS-PEG, D-Cy5, and QDs (10μL of 1ng/μL) were applied at t=1h after OGD injury or equivalent normal control time point. In Chapter 5, 100 μL PLGA-PEG nanoparticles (100 ng/μL) formulated with each surfactant were applied. The slices were then live-incubated for 4h to allow the nanoparticles to diffuse through brain tissue and interact with microglia. For qualitative analysis, slices were fixed, stained for Iba-1+ microglia or NeuN+ neurons, and then imaged.

For quantitative analysis of nanoparticle uptake in Chapters 4 and 5, brain slices were processed for flow cytometry. After 4h of nanoparticle incubation, slices from each experimental group were placed in 1 mL Accutase. Samples were gently shaken on ice for 30 min and then carefully pipetted to ensure tissue was fully homogenized. The sample was then transferred to a new tube through a top filter (Pierce Tissue Strainers) until all the homogenate was filtered. During this process, HBSS and 25 mM HEPES were added to dilute homogenate to a final volume of 10 mL. The tube was spun down at 600xg at 4ºC for 5 min to pellet cells, then aspirated and the supernatant discarded. 100% fetal bovine serum (FBS) was then added to resuspend the cell pellet. Percoll Solution (final concentration 33%) was added to the cell suspension and mixed well, and then FACS media was added to the suspension. The cell suspension was centrifuged for 15 min at 800xg and 4ºC, and then the supernatant was aspirated, leaving the cell pellet at the bottom. To wash excess Percoll Solution, the pellet was resuspended in FACS media and centrifuged for 10 min at 600xg and 4ºC, and again the supernatant was removed. The final pellet was resuspended in FACS media for staining. Fc block (BD Biosciences) was added to the FACS media cell suspension and incubated for 5 min on ice, and then cells were stained with DAPI (1:10,000) and fluorescein isothiocyanate (FITC)-CD11b (1:200). Appropriate controls for CD11b gating were done with an aliquot of the control sample. The cells were stained with the above stains for 15 min and washed 3 times with FACS media for 4 min at 1000xg and 4ºC. The BD LSRII (BD Biosciences) machine recorded cells in each sample with fluorescence in the DAPI, CD11b, and AF555 channels until 100,000 events (live cells) were reached. Analysis of the cytometry data was performed in FCS Express 7 Research and representative data is shown in Figure 2.1.

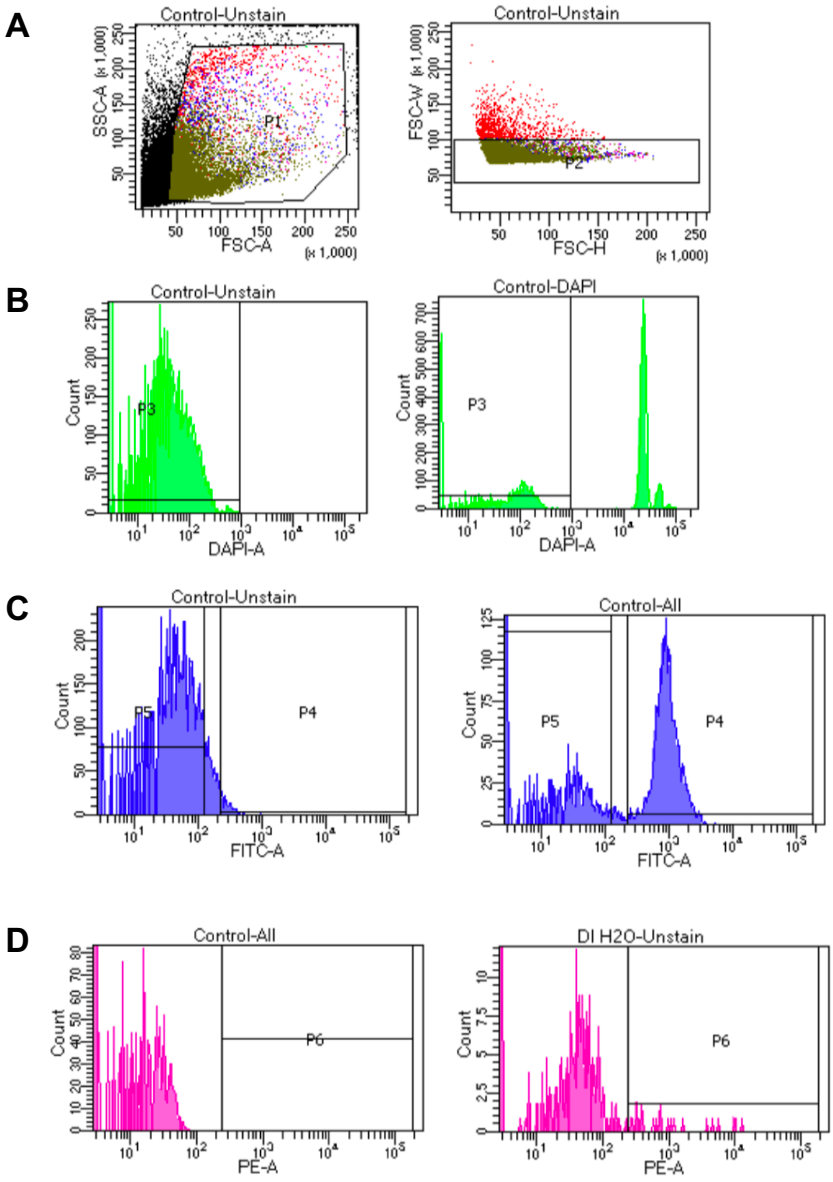

Figure 2.1 Representative FACS data from control samples.
(A) Based on forward and side scatter, gate P1 was drawn such that cellular debris would be eliminated. From height and width scatter, gate P2 was drawn to isolate single cells only. (B) Gate P3 was drawn to isolate DAPI-negative (live) cells; data from an unstained sample (left) and DAPI-stained sample (right) are shown. (C) Gate P4 was drawn to isolate CD11b-positive cells (microglia); data from an unstained sample (left) and CD11b-stained sample (right) are shown. (D) Marker P6 was drawn to determine the proportion of microglia with nanoparticle fluorescence; data from a sample without nanoparticles (left) and with nanoparticles (right) are shown.

Statistical analysis

Statistical analysis of *ex vivo* cytotoxicity, GSH concentration, and microglial uptake by flow cytometry were made using an unpaired t-test, assuming normality. Statistical analysis of MPT

data distributions was conducted using a two-tailed Mann-Whitney U-test. All analysis was performed using GraphPad version 7. A P-value <0.05 was considered statistically significant.

2.3 Methods for nanoparticle analysis *in vivo*

Animal and ethics statement

In vivo animal studies in Chapters 3, 5 and 6 were performed in strict accordance with the recommendations in the Guide for the Care and Use of Laboratory Animals of the National Institutes of Health and as described above. All of the animals were handled according to approved IACUC protocols #4383-01, #4383-02, #4484-01, and #4484-02 of the University of Washington, Seattle, WA, USA. Sprague–Dawley female dams with sex-balanced litters (virus antibody-free CD® (SD) IGS, Charles River Laboratories, Raleigh, NC, USA) were purchased and arrived when pups were postnatal day 5 (P5). The day of birth was defined P0. Before and after the experiment, each dam and her pups were housed under standard conditions with an automatic 12h light/dark cycle, a temperature range of 20–26°C, and access to standard chow and autoclaved tap water ad libitum. The pups were checked for health daily.

Biodistribution, capillary depletion, and nanoparticle quantification

In Chapter 5, AF647-labeled PLGA and PLGA-PEG nanoparticles were administered via tail vein (150 mg/kg) in healthy P9 pups (n=5). After 4h, pups were sacrificed and the animal was perfused with 20 mL 1xPBS. The brain was extracted and major organs (lungs, heart, spleen, liver, and kidneys) were frozen at -80°C. Serum was collected by centrifuging the blood sample at 2000xg for 10 min and removing supernatant. All frozen organs were homogenized by pipetting in 1xPBS at a concentration of 100% (w/v), then centrifuged at 10,000xg for 10 min to remove cell debris. Capillary depletion was conducted on freshly extracted brains (n=4) according to the protocol described by Banks *et al.* [127]. Briefly, brains were homogenized in 0.8 mL capillary depletion buffer (CDB) and then mixed with 1.6 mL CDB with 26% dextran on ice. The homogenate was centrifuged at 5400xg for 15 min at 4°C. The middle, clear layer was separated as the capillary-depleted brain fraction and the bottom, red pellet was resuspended in 0.3 mL PBS as the capillary-rich brain fraction.

Nanoparticle concentration in tissue samples were determined by measurement of sample fluorescence intensities (excitation 625 nm/ emission 665 nm) by UV-Vis spectroscopy. Separate calibration curves were created for each organ and nanoparticle formulation combination; sample curves for brain parenchyma and brain capillaries is shown in Figure 2.2. The same nanoparticle

batch was used for injection and calibration curves. The analysis was conducted by first subtracting blank fluorescence values for every organ from a control animal. All calculated nanoparticle concentrations were normalized by injected dose (ID) and then organ weight to find % ID per mg tissue or mL serum.

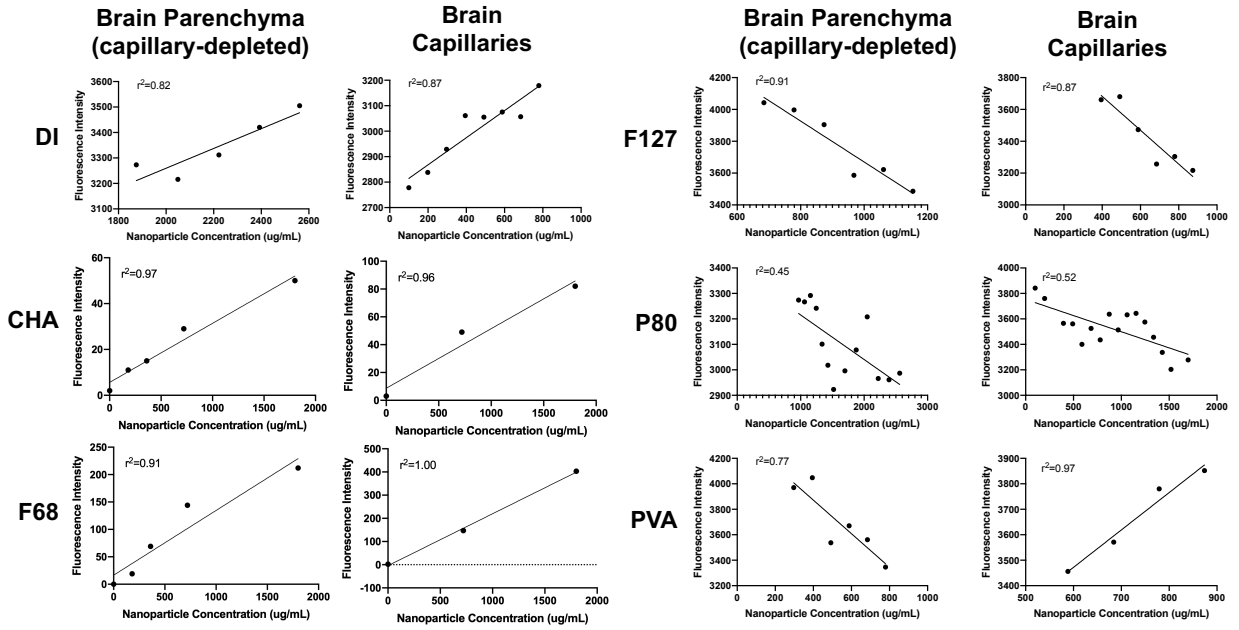

Figure 2.2 Biodistribution calibration curves.
Individual calibration curves for each tissue fraction-nanoparticle combination were created in order to accurately calculate nanoparticle accumulation in the brain.

Unilateral hypoxic-ischemic brain injury model in neonatal rats

The Vannucci model of HIE was performed in Chapters 3 and 6. On the day of insult, pups were separated from their dams, weighed and sexed, and randomized to experimental groups. In Chapters 3, injury was performed on P7; for chapter 6, P10 pups were used. Anesthesia with isoflurane (3% induction, 1.5-2% maintenance) was given in 100% O_2 via a nose cone, under a dissecting microscope. The left carotid artery was identified and either cauterized with fine tip disposable cautery (Chapter 3) or ligated (Chapter 6). Pups were maintained in a temperature-controlled water bath before and after undergoing unilateral ligation of the left carotid artery. After all the animals recovered from anesthesia, they returned to the dams for a minimum of 30 min before placement in a hypoxic chamber in a temperature-controlled water bath. Once rectal temperature in a sentinel animal was stable at 36°C for 5 min, the chamber was sealed and 8% O_2 (92% N_2) administered at a rate of 2.5 L/min. Once the oxygen concentration within the chamber reached 8%, hypoxia was maintained for approximately 2 hours or until 10% mortality

was reached. For all studies in this proposal, temperature of pups was monitored during the nesting period and immediately after each dose of nanoparticle, saline, or free drug.

PLGA-PEG nanoparticle uptake across the impaired blood brain barrier

Nanoparticle uptake across the impaired BBB was assessed in Chapter 3. HI pups (n = 6) were administered 50 mg/kg AF647-PLGA-PEG particles intraperitoneally (i.p). 30 min after HI. Pups were sacrificed 24h after HI injury, perfused, and the brain removed and placed in formalin. FITC-labeled dextran (3 kDa) was injected 30 min after HI at a 7.5 g/kg dose as a measurement of BBB extravasation [128]. For biodistribution, healthy pups (n = 6) were administered 150 mg/kg AF647-PLGA-PEG particles i.p. on P7, with HI pups (n = 10) receiving the same dose 30 min after HI. Pups were sacrificed 24h after injection. Blood was collected before perfusion and organ extraction, and all organs were subsequently frozen at -80°C. Serum was collected by centrifuging the blood sample at 2000xg for 10 min and removing supernatant. Frozen brains were homogenized in 1xPBS using a tissue homogenizer (Wilmad-LabGlass, NJ) and centrifuged at 10,000xg for 10 min to remove cell debris. Nanoparticle concentration in brain and serum samples were determined by comparison to a UV-Vis calibration curve of AF647-PLGA-PEG nanoparticles in 1xPBS (excitation 625 nm/ emission 665 nm). For each animal, brain/serum ratio was calculated by first determining the mg of PLGA-PEG in brain per mg brain tissue and then dividing by mg of PLGA-PEG in serum per ml serum.

Drug administration

For Chapters 3 and 6, treatment was administered i.p. 30 min, 24h, and 48h after HI. Dosage and timing were based on previous investigation of the therapeutic window for pharmacological agents in the Vannucci model [129]. In Chapter 3, a total of 75 pups (42 males, 33 females) were randomized into four separate treatment groups: saline, free curcumin, blank PLGA-PEG nanoparticles, and curcumin-loaded PLGA-PEG nanoparticles. Curcumin dosing was 10 mg/kg in the particle groups and 100 mg/kg in the free drug group. In the free drug group, curcumin was dissolved in DMSO and then diluted in twice the volume of saline. This amount of DMSO was necessary to maintain curcumin solubility, further supporting the need for a nanoparticle delivery system for curcumin. In Chapter 6, a total of 58 pups (30 males, 28 females) were randomized into three separate treatment groups: saline, catalase-loaded nanoparticles (3300 active units/kg), and blank nanoparticles using the hydrophobic ion-pairing method.

Gross injury scoring and total area loss

72h after injury, animals received an overdose of pentobarbital before transcardiac perfusion with 1xPBS followed by 10% neutral-buffered formalin (NBF). Immediately following brain extraction, a photo of each whole brain was taken and subsequently analyzed by an individual who was blinded to group allocation. Gross brain injury in the hemisphere ipsilateral to ligation was assessed on a five-point ordinal scale (0–4) as follows: 0 = no injury, 1 = mild injury with < 25% lesion of ipsilateral hemisphere, 2 = 25–50% lesion, 3 = 51–75%, and 4 = ≥75% injury, as previously described [130].

In Chapter 6, the freshly extracted brain was then sliced into 3 mm thick slices at approximately the level of the hippocampus and thalamus. Slices were incubated in prewarmed 2,3,5-triphenyltetrazolium chloride (TTC, Fisher Scientific) for 10 min at 37°C. The slices were then fixed in 10% NBF for 24h before being imaged for area loss measurement.

In Chapter 3, freshly extracted brains were post-fixed in 10% NBF for at least 48h. Following fixation, blocks of brain were obtained. Using external landmarks, brains were cut at approximately the level of the striatum (block 1) and level of the hippocampus and thalamus (block 2). Sections were paraffin embedded, cut into 5-µm sections, and stained with hematoxylin and eosin (H&E). Given some slide-to-slide variability in the first cohort of animals, four additional sections between the striatum and thalamus at 120 µm intervals were taken in the second cohort of animals. Slides were scanned in bright field with a 20X objective using a Nanozoomer Digital Pathology slide scanner (Hamamatsu; Bridgewater, NJ).

Area loss analysis was performed as previously described [46]. Briefly, two 5 µm sections from the slices best representing the cortex, hippocampus, basal ganglia and thalamus were selected. Virtual slides were exported as 600dpi images. The optical density and hemispheric area of each section was analyzed with ImageJ software by another blinded individual. The average percentage area loss from the two sections (one at the level of the frontal cortex and one at the mid-hippocampal level) was calculated by using the following formula:

$$\% \text{ Area Loss} = \left(1 - \frac{\text{ipsilateral area}}{\text{contralateral area}}\right) \times 100\%$$

Sections from two animals (one each in the blank PLGA-PEG nanoparticle and PLGA-PEG/curcumin groups) could not be assessed for area loss due to damage to the tissue during processing.

Histopathological evaluation

In Chapter 3, H&E-stained slides from saline (n = 17); free curcumin (n = 18); PLGA-PEG/curcumin (n = 20) and blank PLGA-PEG particle (n = 20) treated animals were evaluated by a board-certified veterinary pathologist blinded to treatment group. A previously reported nine-step scoring system for HIE [131] was used, with modifications, to grade the following regions: cerebral cortex; striatum; thalamus; and hippocampus. There was some section-to-section variability, although all regions were present for grading (or in severely affected animals were absent due to marked cystic necrosis) with the exception of one PLGA-PEG/curcumin treated animal in which section 2 was further caudal and lacked hippocampus. This animal had severe disease elsewhere in the brain and was assigned the maximum score of 16. Lesions in the cortex, striatum, and thalamus were scored semi-quantitatively using a 0-4 scale, where "0" was normal; "1" indicated scattered random neuronal necrosis or a small focal area (<10%); "2" indicated columnar damage in the cortex involving layers II-IV or partly confluent or incomplete multifocal to coalescing neuronal cell necrosis/loss affecting 20-30% of the region; "3" indicated large, confluent and complete injury affecting 40-60% of the region (all layers of cortex); and "4" indicated markedly rarefied/cystic lesions with near complete loss of architecture (>80% affected). Half scores were possible based on defined criteria (Table 2.3). Scoring for the hippocampus was also performed on a 0-4 scale, with "1" indicating <10% injury; "2" indicating 50% injury, "3" indicating 75% injury; and "4" indicating 100% injury (Table 2.3).

Table 2.1 Neuropathological scoring criteria.
Region-specific scoring used for evaluation of neuropathology in saline, free curcumin, blank PLGA-PEG, and PLGA-PEG/curcumin treatment groups.

	Cortex, Striatum, Thalamus		**Hippocampus**
Score	Percent involved	Criteria	
0	Normal		No injury
0.5	<10 necrotic neurons		<10 scattered necrotic neurons
1	<10%	small, patchy	<10%; dentate not involved
1.5	10-20%	patchy	<50% or if dentate is involved
2	21-30%	party confluent or incomplete	50%; patchy areas necrotic neurons CA1-4

2.5	31-40%	mostly confluent	Coalescing compared to score of 2; <75% affected
3	40-60%	large, confluent, complete	75%; extensive
3.5	61-80%	severe	76-95%
4	>80%	with cystic rarefaction	complete infarction including dentate (100%)

Scores from each region were summed to yield the final score, ranging from 0 to 16. For figures, the median score from each group was calculated and an animal representing that median score (or within 1 point of the median score) was used to show pathology in the various regions of brain. Images of lesions captured from the digitally scanned slides were exported and plated in Adobe Photoshop Elements. Image brightness and contrast was adjusted using White Balance level and/or Auto Contrast manipulations applied to the entire image. Original magnification and scale bars are stated.

Immunohistochemistry

PLGA-PEG uptake in the brain was evaluated as previously described [132, 133] by placing brains in a formalin-to-30% sucrose gradient and sectioned on a Leica cryostat into 30 μm sections. For cell density and morphology qualitative evaluations, 10 μm slices from a paraffinized brain were deparaffinized before staining. Primary antibodies for microglia (1:250 goat anti-Iba1, Abcam) and neurons (1:250 donkey anti-NeuN, Abcam) were prepared in 1xPBS containing 0.01% Triton-X (Sigma) and either normal donkey serum (Sigma) or normal goat serum (Sigma). Primary antibody solutions were added to tissue sections for 8-12h at 4°C in a humified chamber. Sections were washed twice in 1xPBS. Secondary antibodies were prepared in 1xPBS and added to tissue sections for 2 h. Sections were washed twice in 1xPBS, then stained with 1:1000 DAPI (Invitrogen). Slides were washed and dried for 30 min in the dark. Mounting medium (Dako, Agilent Technologies, Santa Clara, CA) was added to each slide and a glass coverslip placed on top. Slides were stored at 4°C until imaged on an A1 confocal microscope (Nikon Instruments) and at 20°C for long-term storage.

Statistical analysis

Pups carrying rectal probes were excluded from the final analysis, as the stress of carrying probes has previously been shown to have a neuroprotective effect [134]. Injury data is summarized as median with 95% confidence interval (CI). Total area loss, gross injury, and global neuropathology scores were compared using a two-tailed Wilcoxon- Mann–Whitney U-test and a Bonferroni correction applied for multiple comparisons. Statistical analysis was performed using GraphPad version 7. A p-value <0.05 was considered statistically significant.

Chapter 3 – Curcumin-loaded polymeric nanoparticles are neuroprotective in neonatal rats with hypoxic-ischemic encephalopathy

The nontoxic curative compound remains undiscovered but not undreamt.
– James F. Holland
Protecting the newborn brain: we need cocktails and ice!
– Donna Ferreiro

This project feels full of momentous beginnings: when Edward first trained me on formulating curcumin-loaded nanoparticles, which we are now studying in larger animal models of HIE; when I first met the neonatology team, including Tommy, Kylie, and Daniel, who make a comeback in Chapter 6; and when I first learned confocal imaging and multiple particle tracking, which make an appearance in most upcoming chapters. My search for a "nontoxic curative compound", a drug "cocktail" to treat the newborn brain, began here with curcumin.

3.1 Introduction

Preclinically, therapies with broad-spectrum activities including anti-inflammatory and antioxidant properties are thought to have potential for pharmacologically targeting HI brain injury. Curcumin is a promising pharmacologic intervention with anti-inflammatory, antioxidant, and anti-apoptotic effects, and is an inducer of neurogenesis [135-137]. Curcumin is the active ingredient in turmeric, which has been traditionally consumed as a dietary component for centuries [138]. However, in pharmacological form, it has poor bioavailability due to its hydrophobic nature and rapid hepatic metabolism [139]. Incorporation of curcumin into a nanoparticle platform could alleviate current delivery limitations by increasing curcumin's solubility and improving curcumin's absorption, distribution, metabolism, and excretion profiles in the body.

Curcumin nanoformulations have previously been shown to enhance therapeutic efficacy in a variety of animal models of neurological disorders [140], including reductions in edema, oxidative stress, inflammation, and apoptosis, as well as improved behavioral outcomes [141-146]. However, investigation of both curcumin and polymeric nanoparticles has been limited to adult models of injury, despite the fact that the newborn brain is uniquely vulnerable to brain injury [9, 12]. We therefore sought to test the neuroprotective effect of curcumin-loaded polymeric nanoparticles in the Vannucci rat model of neonatal HI brain injury.

3.2 Results

Preparation and characterization of curcumin-loaded nanoparticles

Brain-penetrating curcumin-loaded nanoparticles were synthesized using PLGA polymer and PLGA-PEG diblock copolymer via the nanoprecipitation method. After formulation of curcumin-

loaded nanoparticles, nanoparticle hydrodynamic size, polydispersity index and zeta-potential were determined by DLS and Zetasizer, and curcumin loading and efficiency by UV-Vis (Table 3.1). PLGA/curcumin nanoparticles had a size, ζ-potential, and PDI of 58.84 nm, -4.98 mV, and 0.15 respectively, while PLGA-PEG/curcurmin had similar physicochemical characteristics of 61.13 nm, -2.69 mV, and 0.12. The PLGA-PEG/curcumin nanoparticles achieved marginally higher curcumin loading (6.00%) than PLGA/curcumin (5.27%).

Table 3.1 Physicochemical properties of PLGA and PLGA-PEG nanoparticle loaded with curcumin.

PLGA and PLGA-PEG nanoparticles loaded with curcumin was characterized for hydrodynamic diameter, ζ-potential (ZP), and PDI using dynamic light scattering at 37°C and pH 7.2 in 10mM NaCl. Drug loading (DL) and drug encapsulation efficiency (DEE) was measured using UV-vis spectroscopy. All values are reported with mean ± standard error (SEM).

Particle type	PEG % (w/w)	Mean Size ± SEM (nm)	Mean ZP ± SEM (mV)	Mean PDI ± SEM	DL ± SEM (%)	DEE ± SEM (%)
PLGA45k (50:50)/Curcumin	0	58.8 ± 2.0	-5.0 ± 0.2	0.2 ± 0.01	5.3 ± 0.1	46.0 ± 21.0
mPEG5k-PLGA45k (50:50)/Curcumin	10	61.1 ± 0.8	-2.7 ± 0.1	0.1 ± 0.05	6.0 ± 0.5	27.3 ± 2.6

Drug release studies showed burst release phenomena in both PLGA and PLGA-PEG particles, with 40% and 49% curcumin release, respectively, in the first 4h, followed by a sustained phase releasing up to 59% or 99% curcumin in the next 4 days (Figure 3.1A). SEM imaging shows similar spherical morphology for blank PLGA-PEG and PLGA-PEG/curcumin nanoparticles (Figure 3.1B).

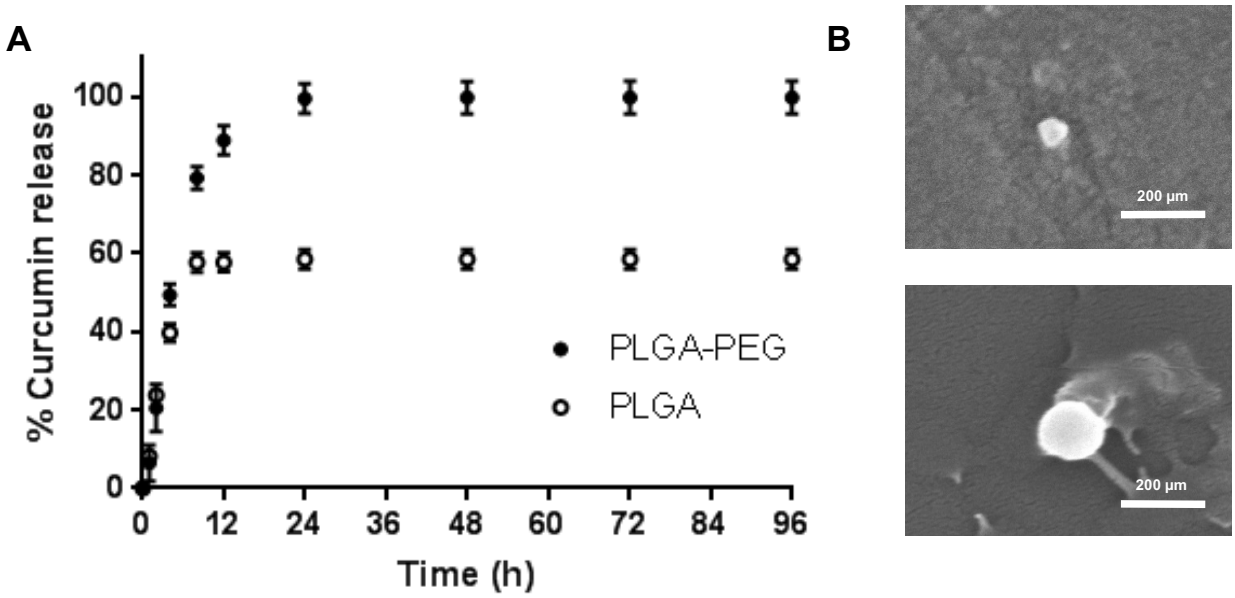

Figure 3.1 Curcumin release kinetics from PLGA and PLGA-PEG nanoparticles. PLGA and PLGA-PEG nanoparticles loaded with curcumin were incubated in 1xPBS with 1% P80 at 37°C and samples were collected over 96h. (A) About 80% curcumin is released from PLGA-PEG nanoparticles within 8h. 41.19% more curcumin is released from PLGA-PEG nanoparticles compared with PLGA nanoparticles within 96h. (B) SEM images show curcumin-loaded PLGA-PEG and blank PLGA-PEG nanoparticles are spherical in shape. Scale bars: 200 nm

PLGA-PEG nanoparticles can diffuse in the brain parenchyma

AF555-labeled PLGA-PEG nanoparticle diffusivity was determined to ensure that particles are capable of moving within the brain microenvironment (Figure 3.2) to reach target cells, upon reaching the brain following systemic administration. Diffusion analysis demonstrated PLGA-PEG nanoparticles had a diffusivity of 0.1 $\mu m^2/s$ in the cortex (Figure 3.2A) and 0.085 $\mu m^2/s$ in the thalamus (Figure 3.2B). This was a 10-fold increase in diffusivity over PLGA particles in the cortex (0.01 $\mu m^2/s$), and a 20-fold increase in diffusivity in the thalamus (0.004 $\mu m^2/s$). Overall, PLGA-PEG nanoparticles had 14-fold higher diffusive ability, 1.13-fold greater drug loading, and a 35% increase in drug release compared to PLGA nanoparticles. Therefore, PLGA-PEG nanoparticles were chosen for evaluation of therapeutic effect in vivo in the rat model of neonatal HI brain injury.

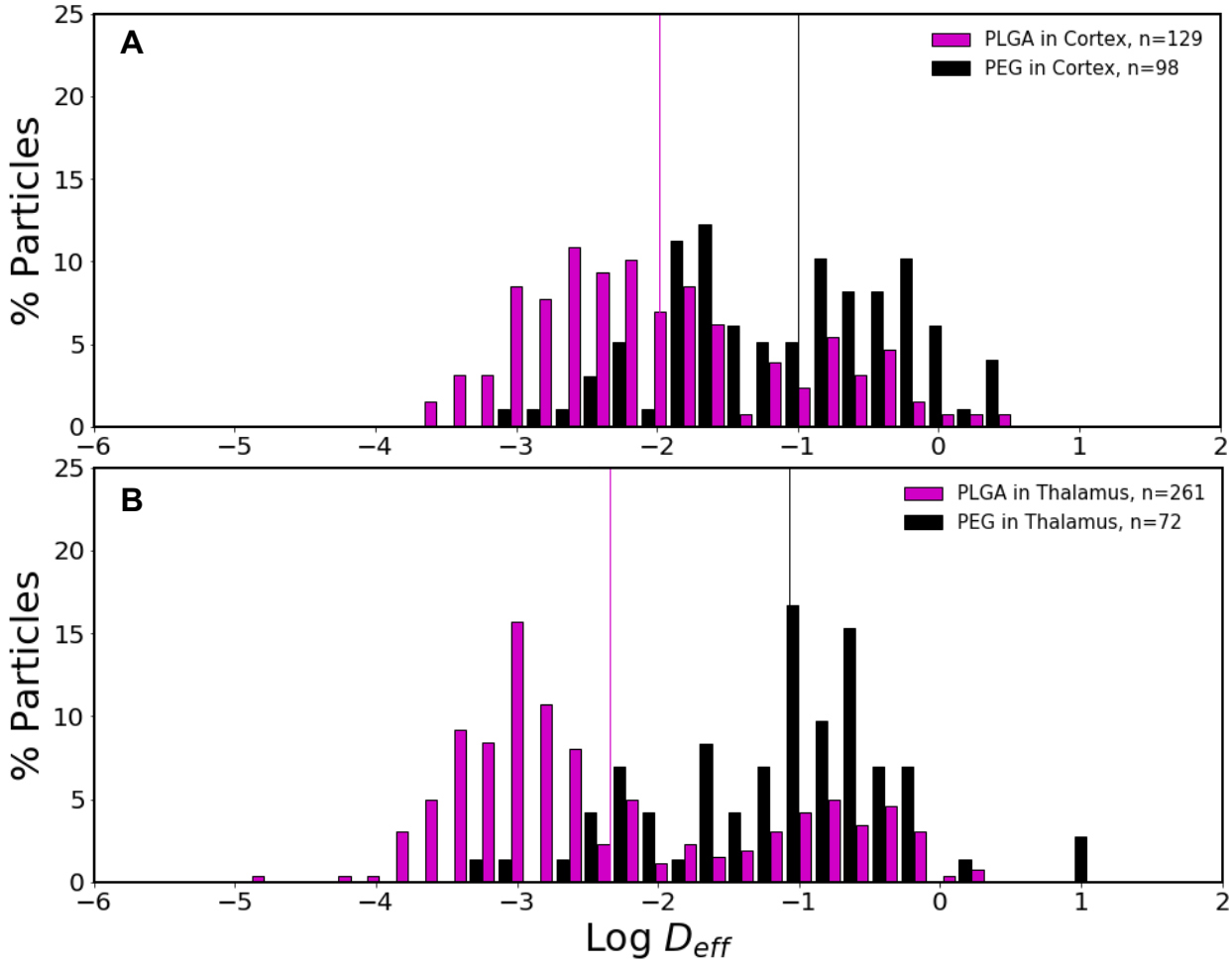

Figure 3.2 Nanoparticle diffusion within the brain parenchyma.
P14 organotypic brain slices were treated with AF555-labeled PLGA and PLGA-PEG nanoparticles. MPT videos were collected and individual particles tracked. (b) Log plot of effective diffusion coefficients of PLGA-PEG nanoparticles in the cortex (n = 98) and thalamus (n = 72). The average D_{eff} in the cortex is 0.1 $\mu m^2/s$ in the cortex and 0.085 $\mu m^2/s$ in the thalamus. (b) Log plot of effective diffusion coefficients of PLGA nanoparticles in the cortex (n = 129) and thalamus (n = 261). The average D_{eff} in the cortex is 0.01 $\mu m^2/s$ in the cortex and 0.004 $\mu m^2/s$ in the thalamus. Data represent means of at least n = 3 experiments in 3 brain slices.

PLGA-PEG nanoparticles can overcome the BBB and extravasate into the parenchyma of the HI brain

AF647-PLGA-PEG nanoparticles accumulated in the hippocampus, dentate gyrus, and thalamus in the ipsilateral hemisphere of the HI brain (Figure 3.3A). However, there was no apparent co-localization in Iba-1+ amoeboid microglial cells (Figure 3.3B) in the CA1 region of the ipsilateral hippocampus. Quantification of AF647-PLGA-PEG nanoparticles in healthy and injured pups (Figure 3.3C) demonstrated significantly higher nanoparticle accumulation in the

injured brain (average brain/serum ratio 0.0135) compared to the healthy brain (average brain/serum ratio 0.0047; p=0.0037). PLGA-PEG extravasation into the brain parenchyma demonstrates that the nanoparticle is able to leverage the impaired BBB to deliver therapeutic payload within proximity of cells involved in ongoing injurious pathways.

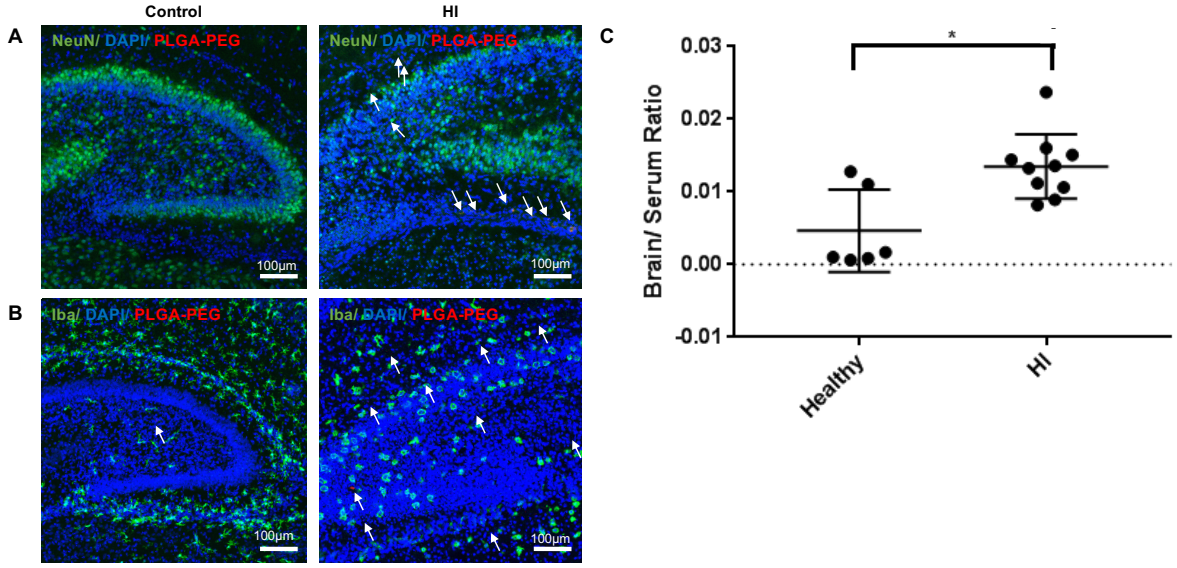

Figure 3.3 Nanoparticle uptake in regions of injury in the HI brain.
AF647-labeled PLGA-PEG nanoparticles (50mg/kg, red) were administered i.p. 30 min after HI in P7 pups. Pups were sacrificed 24h after HI and perfused. (A) PLGA-PEG localization near NeuN+ neurons (green) is visible in the ipsilateral (injured, right image) hemisphere of HI pups. There is no visible uptake near neurons in healthy pups (left image). (B) PLGA-PEG localization near Iba-1+ microglia (green) is also present in the ipsilateral hemisphere in HI pups and absent from uninjured pups. Blue: DAPI cell nuclei stain. Scale bars in all images: 100 μm. (C) Fluorescently-labeled nanoparticles were injected at a 150 mg/kg dose to healthy (n=6, injected at t=0) and HI (n=10, injected 30 min after injury) pups on P7 and pups were perfused and sacrificed after 24h. Nanoparticle concentration in the brain and serum was measured by UV-Vis and normalized to sample volume or mass. The brain/serum ratio in HI pups (0.0135) was significantly higher (p=0.0037) than the brain/serum ratio in healthy pups (0.0047) indicating enhanced brain penetration of the PLGA-PEG vehicle after HI injury.

Curcumin-loaded PLGA-PEG nanoparticle treatment reduces global injury in the Vannucci model

Following i.p. injection of blank PLGA-PEG nanoparticles (250 mg/kg) and PLGA-PEG/curcumin (10 mg/kg curcumin, 250mg/kg PLGA-PEG), free curcumin (100 mg/kg), and saline (10 mL/kg) into HI pups at P7 – P9, gross injury scores decreased significantly from a median (95% CI) of 3 (3-4; p=0.006), 3.5 (1-4; p=0.03), and 4 (3-4; p=0.003) in the saline, free curcumin, and blank PLGA-PEG groups, respectively, compared to a median of 0 (0-3) in the PLGA-PEG/curcumin group (Figure 3.4A). Representative median brains are shown in Figure 3.5. Total area loss showed similar results (Figure 3.4B). Median (95% CI) hemispheric area

loss of the left side was 37.2% (27.9-51.4%), 37.8% (20.2-44.2%), 35.4% (6.0-44.4%), 12.3% (3.6-26.8%), in the saline, free curcumin, blank PLGA-PEG, and PLGA-PEG/curcumin groups, respectively. Area loss was significantly lower in the PLGA-PEG/curcumin compared to the saline (p=0.006) and free curcumin groups (p=0.04). An initial trend (p=0.07) towards a significant difference in area loss between the PLGA-PEG/curcumin and blank PLGA-PEG particle groups did not remain after adjustment for multiple comparisons.

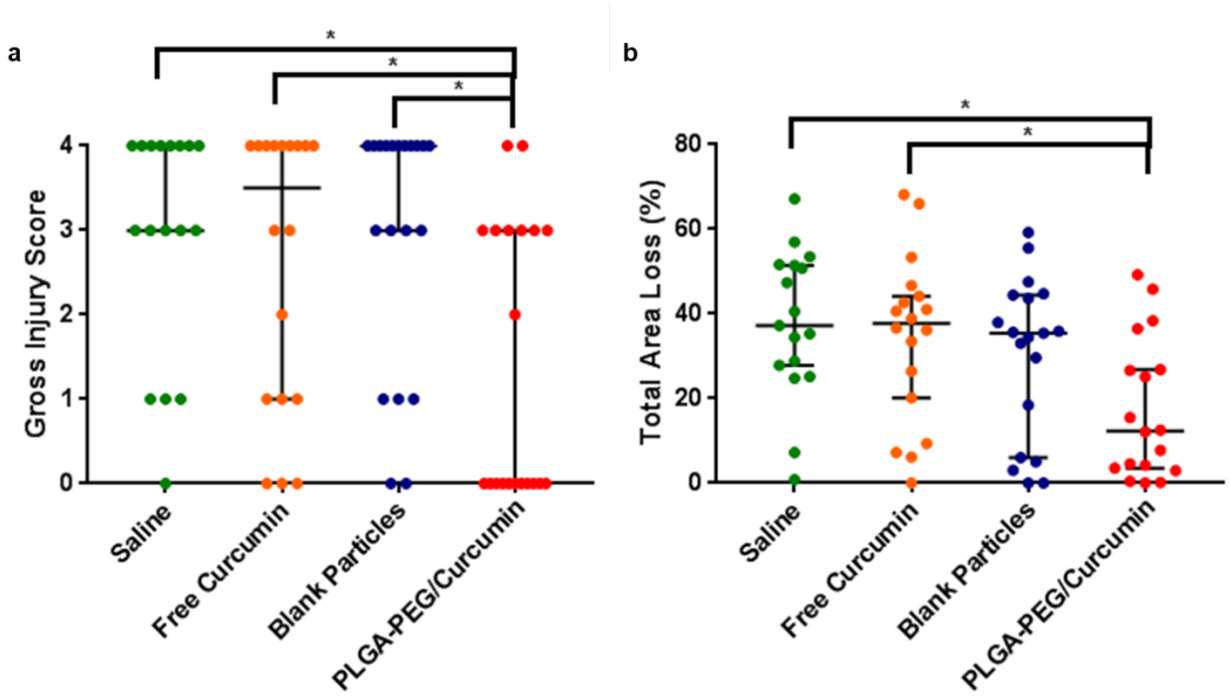

Figure 3.4 PLGA-PEG/curcumin effects on global brain injury and percent area loss in the HI brain.
HI pups were treated 30 min, 24h, and 48h after HI injury with either saline, free curcumin, blank nanoparticles, or PLGA-PEG/curcumin. Pups were sacrificed 72h after HI injury. All analyses were performed in a blinded manner. (A) Median (95% CI) gross injury scores were – saline: 3 (3-4; n = 16), free curcumin: 3.5 (1-4; n = 19), blank PLGA-PEG particles: 4 (3-4; n = 20); PLGA-PEG/curcumin: 0 (0-3; n = 20). Significance was seen between PLGA-PEG/curcumin and saline (p = 0.006), free curcumin (p = 0.03), and blank PLGA-PEG (p = 0.003). (B) Median (95% CI) area losse scores were – saline: 37.2% (27.9-51.4%; n = 16), free curcumin: 37.8% (20.2-44.2%; n = 19), blank PLGA-PEG particles: 35.4% (6.0-44.4%; n = 18); PLGA-PEG/curcumin: 12.3% (3.6-26.8%; n = 19). Significance was seen between PLGA-PEG/curcumin and saline (p = 0.006) and free curcumin (p = 0.04) groups. *Indicates significant difference compared to all other groups.

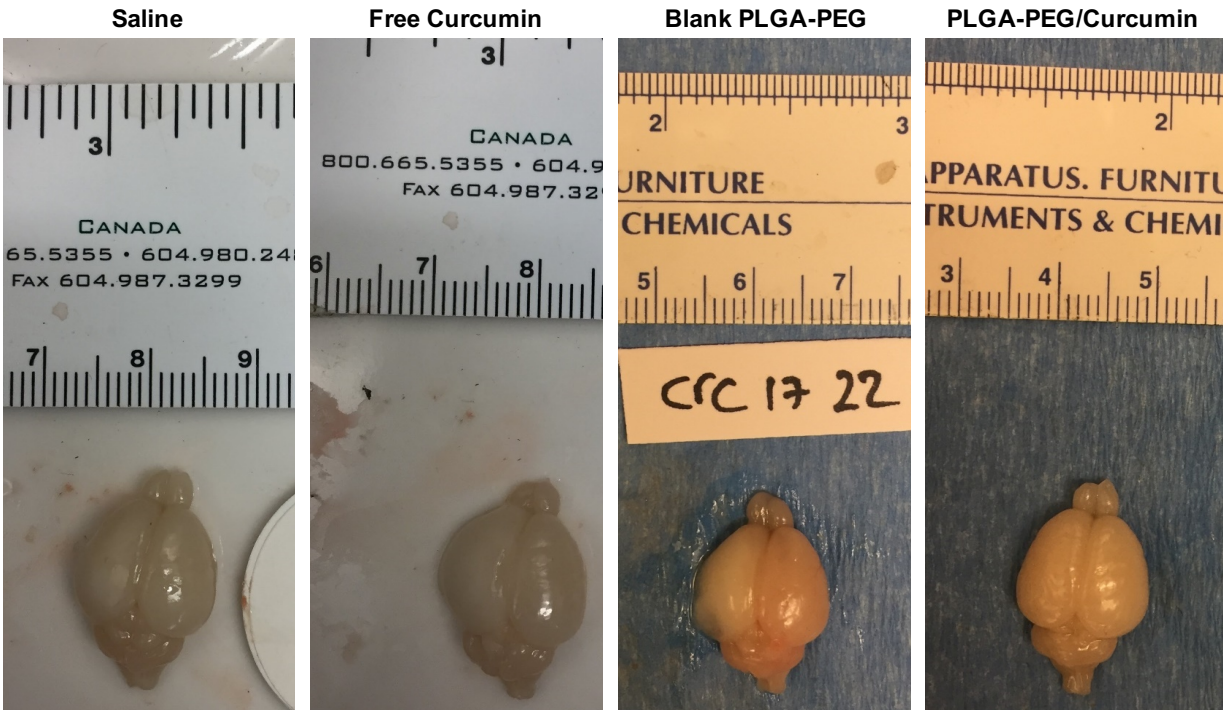

Figure 3.5 Representative gross injury in HI pups.
For each treatment group, a representative picture of the median animal used for gross injury scoring is provided.

Curcumin-loaded PLGA-PEG nanoparticle treatment does not result in region-specific neuroprotection

Marked variation in region-specific response to treatment was seen using histopathological analysis. A plot of region-specific pathology scores by group is presented (Figure 3.6). H&E images showing representative pathology in the different areas assessed are shown in Figure 3.7. Median (95% CI) total pathological score (maximum 16) was 12.5 (10-14.5), 12.3 (9-14.5), and 13.3 (8.5-15) in the saline, free curcumin, and blank PLGA-PEG particles, respectively, and 6.5 (2.5-15.0) in the PLGA-PEG/curcumin group. A similar pattern of decreased median pathology score in the PLGA-PEG/curcumin group was seen in the cortex (Figure 3.6A), thalamus (Figure 3.6B), hippocampus (Figure 3.6C) and striatum (Figure 3.6D); however, none of these differences were statistically significant. A summary of pathology scores, as well as gross injury and area loss analysis across all groups is shown in Table 3.2.

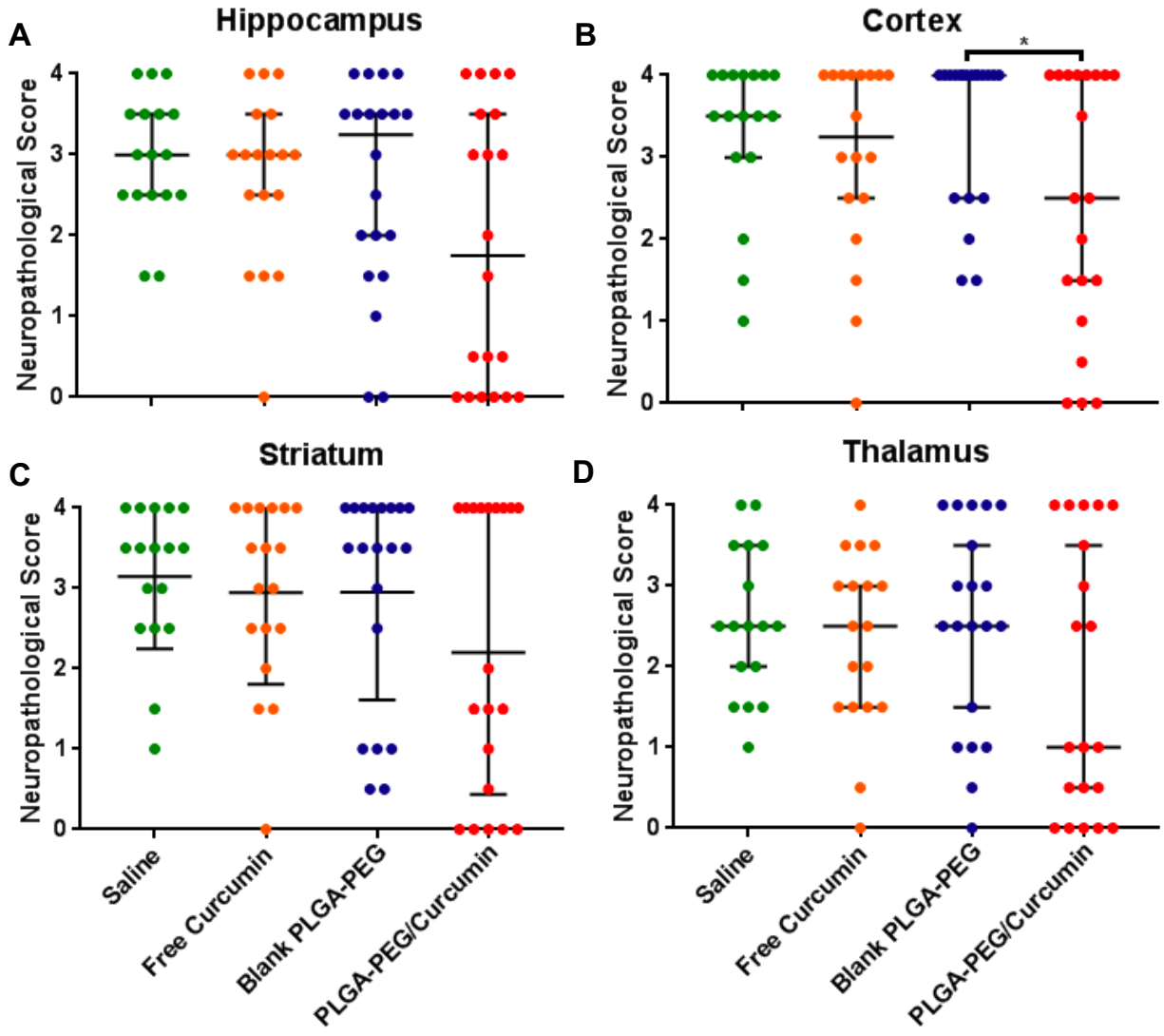

Figure 3.6 Neuropathology following PLGA-PEG/curcumin treatment of HI pups.
HI pups were treated 30 min, 24h, and 48h after unilateral HI injury with either saline, free curcumin, blank PLGA-PEG nanoparticles, or PLGA-PEG/curcumin nanoparticles. Pups were sacrificed on P10, 72h after HI injury. Neuropathological analyses were performed in a blinded manner. Four regions—(A) hippocampus, (B) cortex, (C) striatum, and (D) thalamus—on he unilateral side were scored on a 9-point scale between 0 (least injured) and 4 (most injured). Though median score was lowest in the PLGA-PEG/curcumin group for all measures, significance was only seen in the cortex between blank PLGA-PEG and PLGA-PEG/curcumin ($p = 0.0249$). Groups were compared using a two-tailed Wilcoxon-Mann-Whitney U-test, with Bonferroni correction for multiple comparisons.

Table 3.2 Outcome measures following treatment in neonatal HI rats.
Rats received HI on P7 and treatments (saline, free curcumin, blank PLGA-PEG, and PLGA-PEG/curcumin) were given at 30 min, 24h, and 48h after HI. All outcome measures were assessed 72h after HI injury. For each outcome measure, median (95% CI) gross injury, area loss, and regional and total pathology score across the four treatment groups is provided.

*Indicates significant difference compared to all other groups. #Indicates significant difference compared to saline and free curcumin groups. Groups were compared using a two-tailed Wilcoxon-Mann-Whitney U-test, with Bonferroni correction for multiple comparisons.

		Group (median; 95% CI)			
		Saline	**Free curcumin**	**Blank PLGA-PEG**	**PLGA-PEG/ curcumin**
Injury Assessment	**Gross Injury**	3 (3-4)	3.5 (1-4)	4 (3-4)	0 (0-3)*
	Area Loss (%)	37.2 (27.9-51.4)	37.8 (20.2-44.2)	35.4 (6.0-44.4)	12.3 (3.6-26.8)#
	Pathology scores:				
	Cortex	3.5 (3.0-4.0)	2.4 (2.5-4.0)	2.5 (2.5-4.0)	1.1 (1.5-4.0)
	Hippocampus	3 (2.5-3.5)	3 (2.5-3.5)	3.3 (2.0-3.5)	1.8 (0.0-3.5)
	Striatum	3.5 (2.5-4.0)	3.3 (2.5-4.0)	3.5 (2.5-4.0)	1.8 (0.5-4.0)
	Thalamus	2.5 (2.0-3.5)	2.5 (1.5-3.0)	2.5 (1.5-3.5)	1 (0.5-3.5)
	Total Pathology Score	12.5 (10.0-14.5)	12.3 (9.0-14.5)	13.3 (8.5-15.0)	6.5 (2.5-15.0)

Blank PLGA-PEG, free curcumin and saline treated animals tended to have more severe, extensive necrosis of the anterior cortex and middle cortex (Figure 3.7), often with rarefaction of the neuropil. In the striatum, hippocampus, and thalamus, we observed moderate-to-marked multifocal to coalescing neuronal necrosis and cell loss. In contrast, lesions in more PLGA-PEG/curcumin than blank PLGA-PEG treated animals were more often characterized by mild to moderate columnar necrosis in the cerebral cortex, and mild, patchy neuronal necrosis in the striatum, thalamus and hippocampus. Further, more PLGA-PEG/curcumin treated animals had minimal to no neuropathology, with 8 animals receiving a total neuropathology score lower than 4 (three animals with a score of 0; 2 animals with a score of 2; and 1 animal each with a score of 2.5, 3, and 3.5). In contrast, only 1 animal in each of the blank PLGA-PEG and free curcumin groups scored less than 4, and no saline treated animals received a score lower than 6. Severe injury characterized by variably severe (but generally minimal to mild) involvement of the contralateral hemisphere was observed in all treatment groups (n = 3 saline treated animals; n = 1 free curcumin treated animal; n = 6 blank PLGA-PEG treated animals; and n = 4 PLGA-PEG/curcumin treated animals).

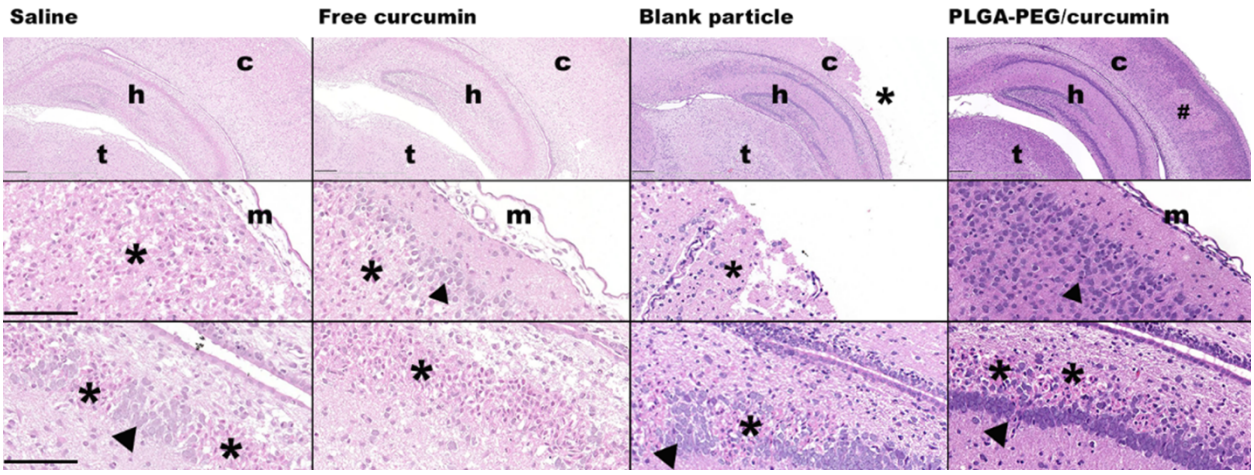

Figure 3.7 Representative histology images of PLGA-PEG/curcumin treated pups. Left column – saline treated animal; Left center – free curcumin treated animal; Right center – blank PLGA-PEG treated animal; Right column –PLGA-PEG/curcumin treated animal. Animals within one point of the treatment group median are pictured. Top row: Lower magnification view of the hippocampus (h) and cerebral cortex (c) at the level of the thalamus (t). In the saline, free curcumin, and blank PLGA-PEG treated animal there is moderate to regionally marked disorganization and neuronal death of the cortex with a portion of ischemic cortex missing (*) in the blank PLGA-PEG treated animal. In the PLGA-PEG/curcumin treated animal, there is mild multifocal columnar neuronal cell necrosis and loss (#). Bar = 0.25 mm. Middle row: Higher magnification of neuronal cell death and loss with disorganization of the cortex (*). Normal neurons are indicated by the triangle. M = meninges. Bar = 100 μm. Bottom row: Hippocampus (CA1 and CA2) with regionally extensive neuronal necrosis and loss (*). Normal neurons are indicated by the triangle. Bar = 100 μm.

Microglia show altered morphology following PLGA-PEG/curcumin nanoparticle treatment

We observed an increase in microglial numbers (Iba-1+ cells), and a change in microglial morphology, in the brains of the saline, free curcumin, and blank nanoparticle treatment groups 72h after HI injury (Figure 3.8A). Microglial morphology was more amoeboid in shape in the dentate gyrus, CA1, and subcortex of the ipsilateral hemisphere in the saline, free curcumin, and blank nanoparticle groups, with no differences in morphology seen between them. However, PLGA-PEG/curcumin treated animals showed reduced microglial numbers, and fewer amoeboid morphological features. In particular, in the CA1 region in the PLGA-PEG/curcumin treated pups, microglia were more elongated. A few cell processes were also present, potentially indicating a return to a more normal ramified state (Figure 3.8B). The morphological changes in microglia were confined to regions of neuronal injury, which included the CA1 region of the hippocampus, subcortex, and the caudate putamen.

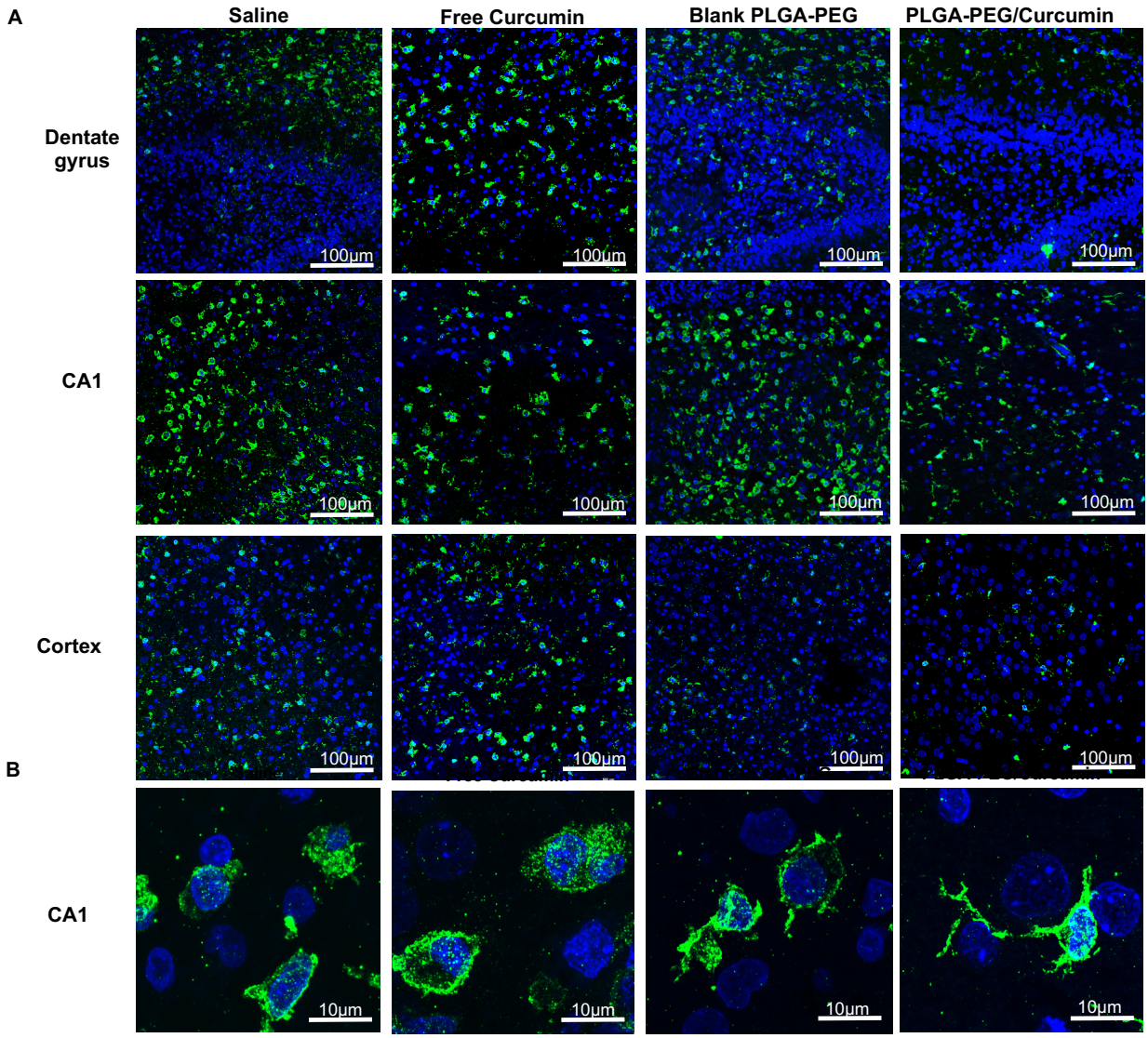

Figure 3.8 Microglial density following HI and PLGA-PEG/curcumin treatment.
The presence of Iba-1+ microglia (green) was evaluated in regions of injury in the HI brain for all treatment groups, including the cortex, CA1, and dentate gyrus. Microglia number is increased in all control groups (saline, free curcumin, and blank PLGA-PEG) and morphology shifted to an amoeboid phenotype. PLGA-PEG/curcumin-treated microglia appear to be fewer in number and partially ramified. Blue: DAPI cell nuclei stain. Scale bars in all images: 100 μm.

3.4 Discussion

PA and resulting HIE are leading causes of morbidity and mortality around the time of birth [54]. Although TH is currently the only validated treatment for HIE, it is not universally neuroprotective. Unfortunately, 40-50% of treated infants with moderate and severe HIE will still die or have significant neurological disability [65]. As the development of TH into a neuroprotective strategy for neonates was based on preclinical research in a number of animal models, there is scope to use these same models to develop pharmacological interventions as

an adjuvant to TH. For instance, Juul *et al.* demonstrated the neuroprotective effects of recombinant human Epo in the Vannucci rat model, which has more recently been translated to clinical trials with term infants and extremely low gestation neonates [70]. Analogous to the pleiotropic neuroprotective effects of both TH and Epo, the present study proposes that curcumin similarly affects the progression of brain injury through multiple pathways, ultimately delivering a neuroprotective effect which is enhanced by using the PLGA-PEG polymeric nanoparticle.

Significant neuroprotection was seen in the PLGA-PEG/curcumin treatment group compared to all control groups (saline, free curcumin, and blank nanoparticle) by gross brain injury scoring. Hemispheric area loss also showed significant neuroprotection ($p<0.05$) in the PLGA-PEG/curcumin treatment group compared to all control groups. However, after adjusting for multiple comparisons, no difference was seen between the PLGA-PEG/curcumin and blank PLGA-PEG groups. This might be due to a therapeutic effect of the PLGA-PEG polymer itself, as others have shown that PEG can suppress reactive oxygen species production after injury by limiting superoxide generation [147]. Despite the significant decrease in global injury measures (gross injury and area loss), no significant decreases in region-specific or total formal pathology score in the PLGA-PEG/curcumin group were seen. This may be due to a lack of resolution in the gross injury score, or the fact that the formal pathology scoring system includes the subcortical structures not seen on the gross injury score.

The difference in efficacy between measures may also give clues as to where the PLGA-PEG/curcumin is exerting its effects. Both area loss and pathology scoring focus on the areas at the center of the unilateral infarct that are most susceptible to the injury [46, 148]. By comparison, gross injury scoring will include the total infarct area, including the penumbral region [149]. The dramatic decrease in gross injury score suggests that PLGA-PEG/curcumin may be most beneficial at the penumbra, and that it is neuroprotective for cells that are less severely affected by the insult. This is also supported by the fact that the median pathology score (both total and region-specific) decreased in the PLGA-PEG/curcumin group, but the upper bounds of the 95% CI did not, suggesting that any neuroprotective effect of PLGA-PEG/curcumin was particularly absent in the most severely-injured animals. This is not an uncommon finding in the field, with TH and other therapies, including xenon, potentially unable to rescue injury once beyond a certain severity [148, 150]. In fact, comparing the pathology scores seen in our current study to similar previous work would suggest that the injury produced in this model was relatively severe [46], with many animals experiencing complete structural loss of the ipsilateral hemisphere, and involvement of the contralateral side [45]. Certain aspects

of the response to injury may also prevent optimal penetration of the particle and delivery of the therapeutic. Edema formation in the most severely-affected animals could reduce penetration of the particle into the core of the infarct. Though nanoparticle penetration into the region of injury was seen, and a therapeutic effect was achieved on gross injury analysis, uniform distribution of a therapeutic from the penumbra to the core is necessary to achieve maximal efficacy [151, 152]. Co-administration of PLGA-PEG/curcumin with therapies that reduce edema formation, such as TH, may augment the effects of the particle, and this combination will be a focus of future work.

Polymeric nanoparticle systems have been widely used to improve biodistribution and bioavailability of therapeutics. Nanoparticles coated with special surfactants, such as P80 [153, 154], Poloxomer 188 (also referred to as Pluronic F68) [153, 155], or with chitosan [156], have also been shown to target the brain following systemic injection, even with an intact BBB, by adhering to and entering endothelial cells of the BBB. However, the nanoparticles coated with P80 or Pluronic F68 in these studies possessed surface charges in the −20 to −40 mV range, and the chitosan-coated particles were 260 nm in diameter, thereby making it unlikely that these specific particles were capable of diffusing into the brain beyond the BBB endothelium [83, 117]. The curcumin-loaded particles used in this study were around 60 nm in diameter and had near-neutral surface charge, both characteristics that enhance penetration of nanotherapeutics within the brain parenchyma. Additionally, PEG copolymerization to PLGA imparts steric stability for improved nanoparticle bioavailability upon systemic administration [157, 158]. The PLGA-PEG nanoparticles used in this study demonstrated a 10-fold higher diffusive ability in the cortex and 20-fold higher diffusivity in the thalamus compared to the PLGA formulation. This is likely due to the “stealth” nature of PEG-coated particles that limits interaction with cells and proteins in the brain extracellular space [118]. Increased diffusive ability is significant because it allows the nanoparticle and curcumin payload to achieve greater dispersion in the brain, a property which is correlated with the efficacy of many therapeutics [73, 159, 160].

Greater drug release from curcumin-loaded PLGA particles was achieved by modifying surface functionality with the PEG polymer. PEG, as an amphiphilic polymer, is able to increase the surface area of the nanoparticle and therefore increase the fraction of curcumin that is adsorbed onto, or weakly bound to, the nanoparticle surface [161]. The early burst release phase is therefore dominated by drug release from near the nanoparticle surface, as seen in the PLGA-PEG/curcumin formulation, which demonstrated higher burst release (40% from PLGA and 49% from PLGA-PEG within 4h) and greater controlled release over 96h (59 vs 99%) compared to the PLGA/curcumin formulation [162].

After being delivered to the injured brain, curcumin can act on HI injury through multiple pathways. Others have demonstrated the therapeutic properties of curcumin, including both antioxidant [163, 164] and anti-inflammatory [165, 166] effects. Curcumin's anti-inflammatory effects are due to inhibition of nuclear factor kappaB signaling, which leads to a reduction in proinflammatory cytokines and enzymes [166, 167]. *In vitro* and *in vivo* studies have shown that curcumin's antioxidant effects arise from direct scavenging via the phenolic structure, as well as modulation of nuclear factor (erythroid-derived 2)-like 2 pathway [164]. Curcumin also inhibits activation of the NMDA receptor for glutamate, which is central to the initiation of the exito-oxidative cascade that results in necrosis and apoptosis from mitochondrial damage after HI injury [168]. Finally, curcumin induces neurogenesis by modulating the canonical Wnt/b-catenin pathway, leading to reversal of cognitive deficits in models Alzheimer disease [169].

PLGA-PEG nanoparticle uptake in the injured brain was observed within 24h in the regions of injury. Nanoparticle uptake and extravasation into regions of injury and proximity close to amoeboid microglia and injured neurons is important because both cell types are implicated in the progression of HI brain injury. During inflammation, microglia proliferate, with a shift in phenotype from ramified healthy surveying microglia to a spectrum of more amoeboid "activated" microglia [25-27]. After 72h of therapy, microglia were fewer in number in the PLGA-PEG/curcumin group, with a more ramified morphology, compared to the control groups. This suggests that PLGA-PEG/curcumin is capable of selectively altering microglial function in areas of injury, which may reduce the long-term inflammatory responses to HI that contribute to the secondary and tertiary phases of injury [16]. However, longer-term outcomes may be needed to discriminate the benefit seen in changing microglial phenotype in the PLGA-PEG/curcumin group.

The brain uptake and region-specific localization of the polymeric nanoparticle platform can play a significant role in targeted delivery, especially if toxicity of a drug is of concern. It is important to emphasize that minimal or no nanoparticle uptake is seen in regions of healthy tissue, which will reduce off-site toxicity and minimize any long-term unwanted effects. Instead, the PLGA-PEG/curcumin particle leverages both BBB breakdown in regions of injury and nanoparticle stealth properties to distribute specifically within the injured brain parenchyma. The ability of the PLGA-PEG/curcumin particle to deliver a broad-acting therapeutic to injured cells for neuroprotection, without associated toxicity, highlights the advantages of using a nanoparticle platform for targeted delivery.

Limitations to this study include the relatively early (72h) assessment of injury, and the absence of behavioral outcomes. For instance, compared to previous work that assessed area

loss at P14, one week after injury [46, 148], area loss at P10 may underestimate final tissue loss due to a shorter time period for the injury to evolve. Future studies with longer follow-up after the injury may allow for greater resolution in terms of comparing injury severity in the different treatment groups. Additionally, due to the limited solubility of curcumin, DMSO was needed in addition to PBS as a delivery vehicle for the free curcumin treatment. Previous studies using DSMO at concentrations ranging from 0.1% (v/v) to 100% to deliver curcumin in cell cultures reported no significant cytotoxicity [170-173]. DMSO was also used to deliver melatonin in the neonatal HI model and no significant neurotoxic effect was found between DMSO and PBS treatment groups [174]. When an effect has been found DMSO at similar concentrations to deliver curcumin in brain injury models, it has instead erred on the side of neuroprotection rather than neurotoxicity [175]. The conflicting literature and need for DMSO to solubilize curcumin further justifies the use of nanoparticle-based delivery platform. Lastly, the experiment was not designed to evaluate sex-based differences. Significant changes in outcome based on sex have been observed in both preclinical models and the clinical setting, and males and females may have different requirements for interventions that modulate oxidative stress [176-181]. To further support the use of curcumin-loaded nanoparticles as a pharmaceutical intervention in perinatal brain injury, PLGA-PEG/curcumin must also be compared to treatments like Epo and NAC, which have demonstrated efficacy in injury models comparable to the Vannucci model [40, 129]. The increased efficacy of the PLGA-PEG/curcumin particle over free curcumin also supports the idea that other potential agents besides curcumin that experience delivery or pharmacokinetic barriers to neuroprotection could be loaded into similar particles. Nevertheless, this is the first study that demonstrates the neuroprotective effect of curcumin, when loaded into brain-penetrating PLGA-PEG nanoparticles, in the treatment of neonatal brain injury.

3.5 Conclusion

One critical yet underserved population for therapeutic development is the neonatal population, for whom PA and subsequent development of HIE is a leading cause of death. We sought to investigate the efficacy of curcumin, a pharmaceutical intervention that works on multiple pathways to reduce inflammation and promote neuronal recovery, in a rat model of neonatal brain injury. Therapeutic delivery mediated by the PLGA-PEG polymeric nanoparticle platform was used to improve efficacy by increasing drug solubility, stability, bioavailability, and targeting of sites of injury. We show that BBB impairment enhances nanoparticle extravasation into the brain parenchyma, and that a dense PEG coating on the PLGA nanoparticles allows for effective penetration within the brain parenchyma. As a result, when administered systemically,

PLGA-PEG/curcumin significantly reduces global injury, but its neuroprotective effect may be most pronounced in the penumbral region, or in less severely injured animals. The neuroprotective effect of curcumin-loaded nanoparticles provides an additional intervention for further study in the treatment of neonatal brain injury.

In the next chapter, we more closely evaluate nanoparticle behavior in the diseased brain environment using an *ex vivo* model of HI injury. We identify features of nanoparticles and of the disease state that promote selective nanoparticle uptake into microglia, which can be desirable for targeted therapeutic delivery and the reduction of off-target effects.

Chapter 4 – Nanoparticle-microglial interaction in the ischemic brain is modulated by injury duration and treatment

A model is a lie that helps you see the truth.
– Howard Skipper

This project was delightfully designed to showcase most of our lab's core tools: nanoparticles, multiple particle tracking, organotypic brain slices, confocal imaging, and image analysis. It gave me an opportunity to work closely with Rick and Mengying in their final year, and also with Mike, Hawley, and Jeremy. Putting all our expertise together, we developed a brain slice model of hypoxic-ischemia to "help us see the truth" of nanoparticle behavior in diseased tissue.

4.1 Introduction

Cerebral ischemia is a major cause of death in both neonates and adults [182, 183]. Unfortunately, treatments for both neonatal HI and adult stroke provide only modest benefits in mortality and morbidity [184, 185]. Investigation of effective treatments for HI continues to be a critical area of research. Microglia, the resident immune cells of the brain, are of more recent and special interest for therapeutic targeting in HI [186]. Microglia become activated after ischemic injury, exhibit increased phagocytic behavior, and contribute to neuroinflammatory and ROS stress that may exacerbate damage in the brain [30]. Thus, an opportunity exists to provide neuroprotection after ischemic injury by designing therapeutics to target and modulate microglial behavior.

A promising strategy for microglial-targeted therapeutic development is the delivery of drugs via nano-sized carriers. Although nanoparticle platforms vary widely in composition, shape, and other physical characteristics, several distinct nanoparticle types have shown an ability to overcome biological barriers to drug delivery in the brain. For example, polymeric nanoparticles (size <200nm) with a dense PEG coating can rapidly penetrate within small pores in the brain ECS that restrict the diffusion and broad distribution of most therapeutics [83, 187]. Adequate intracellular trafficking of therapeutics also presents a major drug delivery challenge, but nanoparticles can leverage existing endocytosis pathways in microglial cells for internalization. QDs and poly(amidoamine) (PAMAM) dendrimer nanoparticles, among others, have shown accumulation within activated microglia [112, 113, 132, 133, 188]. Importantly, these transport routes may be altered in the presence of injury. While nanoparticles can facilitate and enhance drug transport in the brain, these effects are dependent on both nanoparticle characteristics and disease state [189], requiring further screening and study.

We investigate the role of injury, treatment, and nanoparticle type in driving nanoparticle-microglial interactions in ischemic conditions. We use *ex vivo* organotypic whole hemisphere

(OWH) brain slices, which have emerged as a facile platform for modeling disease processes and screening therapeutic platforms, including nanoparticles [113, 190, 191]. The ability to obtain multiple OWH slices from a single brain reduces biological variation and enables detailed investigation of disease environments or therapeutic efficacy. OWH slices also preserve functional relationships between neighboring cells and maintain 3D-cytoarchitecture [190]. Importantly, oxygen-glucose deprivation (OGD) has been widely used to model ischemic injury in organotypic slices [192]. OGD brain slice models retain *in vivo* pathological processes including extracellular glutamate release, neuronal damage, and production of cytokines and oxidative stress markers [193-195]. Thus, OGD-exposed OWH slices are a powerful high-throughput screening platform for evaluation of cell interactions with nanoparticle therapeutics in ischemia to study how nanoparticle-based drug delivery can be used to improve therapeutic outcomes.

To establish the degree of injury and microglial response following OGD exposure, we evaluate cytotoxicity and oxidative stress in healthy, OGD-exposed, and azithromycin (AZ)-treated OWH brain slices. AZ is an FDA-approved therapy that can suppress both acute and chronic pathologic microglial activation in response to ischemic stroke injury [196, 197]. Because microglial behavior correlates with disease severity [198, 199], AZ modulation of microglia provides a validated platform to study microglia-nanoparticle interaction in response to treatment [200]. We use a Python-based image analysis technique to quantify the degree of microglial morphological heterogeneity following injury and treatment. We next investigate how injury alters nanoparticle diffusion within the brain, an important factor for maximal distribution and microglial cell interaction. Lastly, we quantify nanoparticle uptake in microglia based on injury and treatment with flow cytometry and immunofluorescent imaging. We compare 3 distinct nanoparticle platforms, PS-PEG, PAMAM dendrimers, and cadmium selenide/ cadmium sulfide (CdSe/CdS) core/shell QDs, to determine the influence of nanoparticle physical characteristics on microglial uptake. By using nanotechnology to probe microglial changes after disease and treatment, our study informs the design of nanoparticles to leverage the brain microenvironment and target microglial cells for enhanced therapeutic outcome in ischemic conditions.

4.2 Results

OGD time-dependent severity

HI duration can drastically change disease outcomes [201]. Therefore, we first investigated the impact of OGD time on cell viability and the oxidative stress environment. Compared to NC slice cytotoxicity of 11.2%, 0.5h, 1.5h, and 3h OGD exposure times resulted in significant increases

in cytotoxicity of 54.3%, 33.8%, and 32.9% respectively (Figure 4.1A). The 0.5h OGD cytotoxicity was also significantly higher than that of 1.5h or 3h OGD. 0.5h, 1.5h, and 3h OGD exposure times also yielded significantly decreased GSH concentrations of 1.7-fold, 4.1-fold, and 2.3-fold reductions respectively (Figure 4.1B).

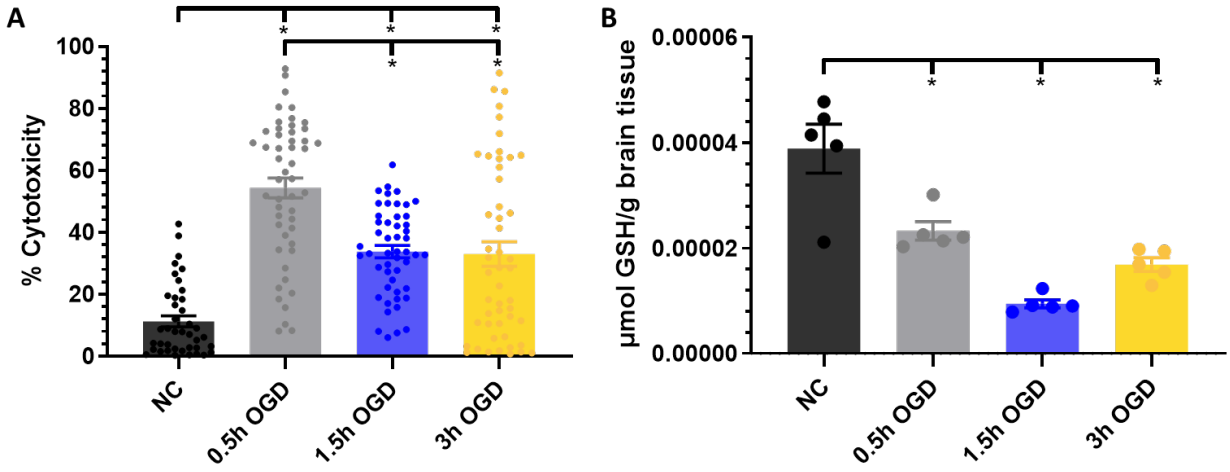

Figure 4.1 OGD exposure-dependent effect on cell death and oxidative stress environment.
(A) Percent cytotoxicity as determined by PI-positive/DAPI-positive cell ratio (n=40-50 per condition) and (B) GSH concentration (n=5) for NC, 0.5h, 1.5h, and 3h OGD-exposed brain slices.

Prior to investigating AZ effects on nanoparticle interaction with microglia, we evaluated AZ and SOD effect on OGD-induced cytotoxicity to confirm therapeutic effects seen in literature. We have previously demonstrated that SOD can attenuate excitotoxic damage in OWH brain slices [190]. SOD addition to 3h OGD-exposed slices significantly reduced cytotoxicity to 17.1% ($p=0.036$) (Figure 4.2A). Having observed the greatest cytotoxicity induced by 0.5h OGD compared to NC, we proceeded to investigate the cytotoxicity effect of AZ on 0.5h OGD-exposed slices. AZ treatment significantly reduced cytotoxicity to 14.0% ($p<0.001$) (Figure 4.2B). AZ treatment also significantly increased GSH concentration 1.5-fold compared to that of 0.5h OGD ($p=0.013$) (Figure 4.2C).

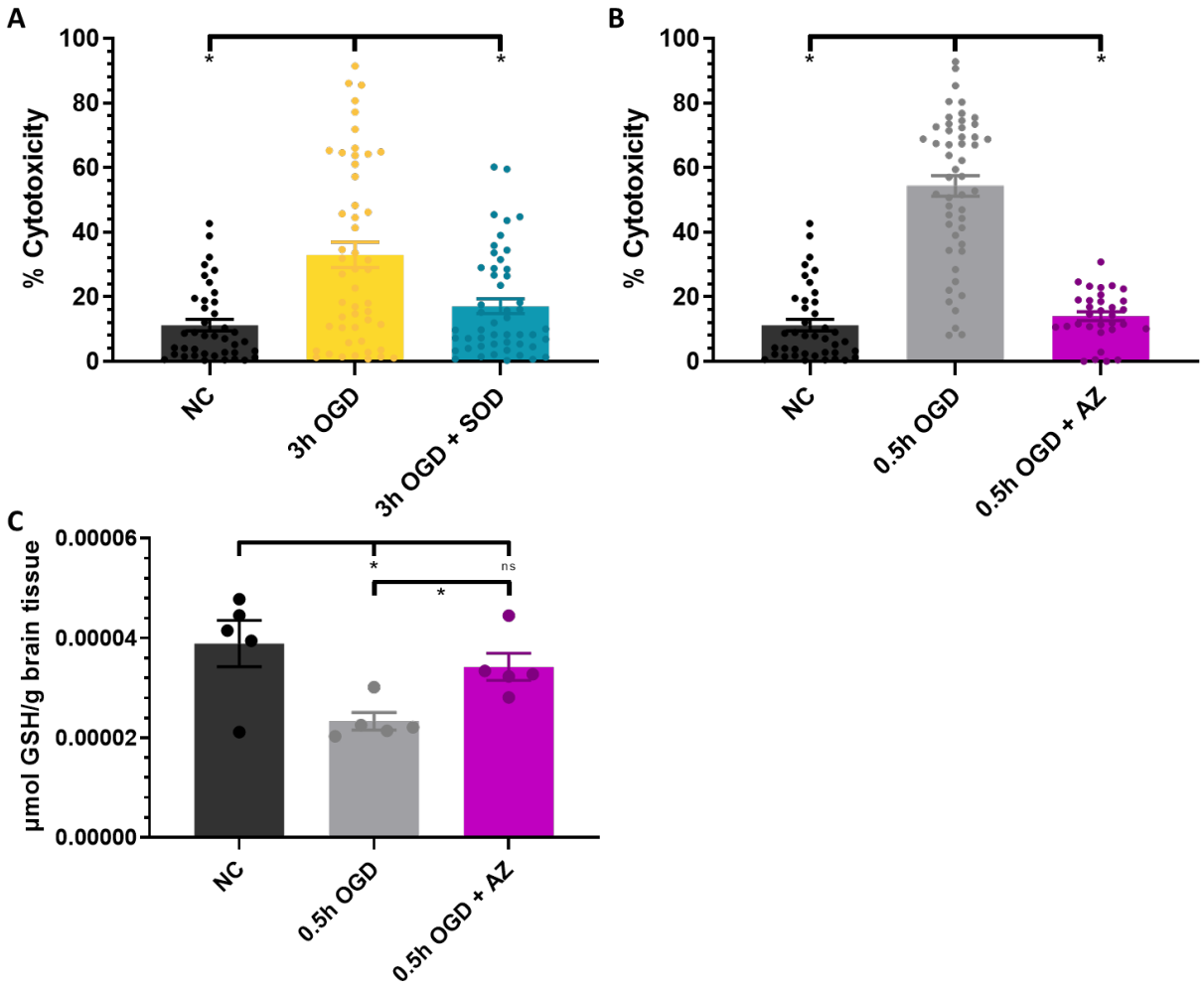

Figure 4.2 Therapeutic effects on OGD exposure-induced injury.
Percent cytotoxicity of (A) NC, 3h OGD, and 3h OGD+SOD (n=40-50 per condition) and (B) NC, 0.5h OGD, and 0.5h OGD+AZ (n=33-50 per condition) measured by PI-positive/DAPI-positive cell ratio. (C) GSH concentrations of NC, 0.5h OGD, and 0.5h OGD+AZ (n=5). NC, 0.5h OGD, and 3h OGD conditions are the same as presented in Figure 4.1.

OGD and AZ effects on microglial shape as determined by VAMPIRE

To better understand microglial response to OGD injury, we characterized microglial morphological heterogeneity across disease states. Microglial morphology and heterogeneity are dependent on disease environment and are one indicator of microglial phenotype and function [202, 203]. VAMPIRE package determined 5 distinct microglial shape modes and subsequently classified all imaged microglia into shape modes [121]. Figure 4.3A displays the frequency of the 5 shape modes for each group, where frequency is the percentage of microglia that exhibited the given shape mode. 0.5h OGD+AZ treatment resulted in a shape mode distribution similar to that of NC microglia: shape modes 3, 4, 5, 1, and 2 in order of increasing

frequency. Overall, 0.5h OGD showed a reduced spread in shape mode frequencies, indicating an increase in microglial shape heterogeneity since all 5 shape modes were more equally represented. The absolute difference of shape mode frequency from NC shape mode frequency was 4.5% and 2.2% for 0.5h and 0.5h OGD+AZ respectively, although the difference between the two groups was not statistically significant (p=0.083) (Figure 4.3B). Circularity was calculated directly from individual microglia. Upon 0.5h OGD exposure, microglia exhibited a significantly increased circularity of 0.69 compared to NC circularity of 0.50 (p<0.001) (Figure 4.3C). AZ treatment reversed the extent of microglial circularity to 0.53, significantly lower than that of 0.5h OGD (p<0.001). NC and OGD+AZ circularity were also significantly different (p<0.001). Furthermore, circularity did not correlate to shape mode, with a greater circularity for the 0.5h OGD condition for each of the 5 shape modes (Table 4.1).

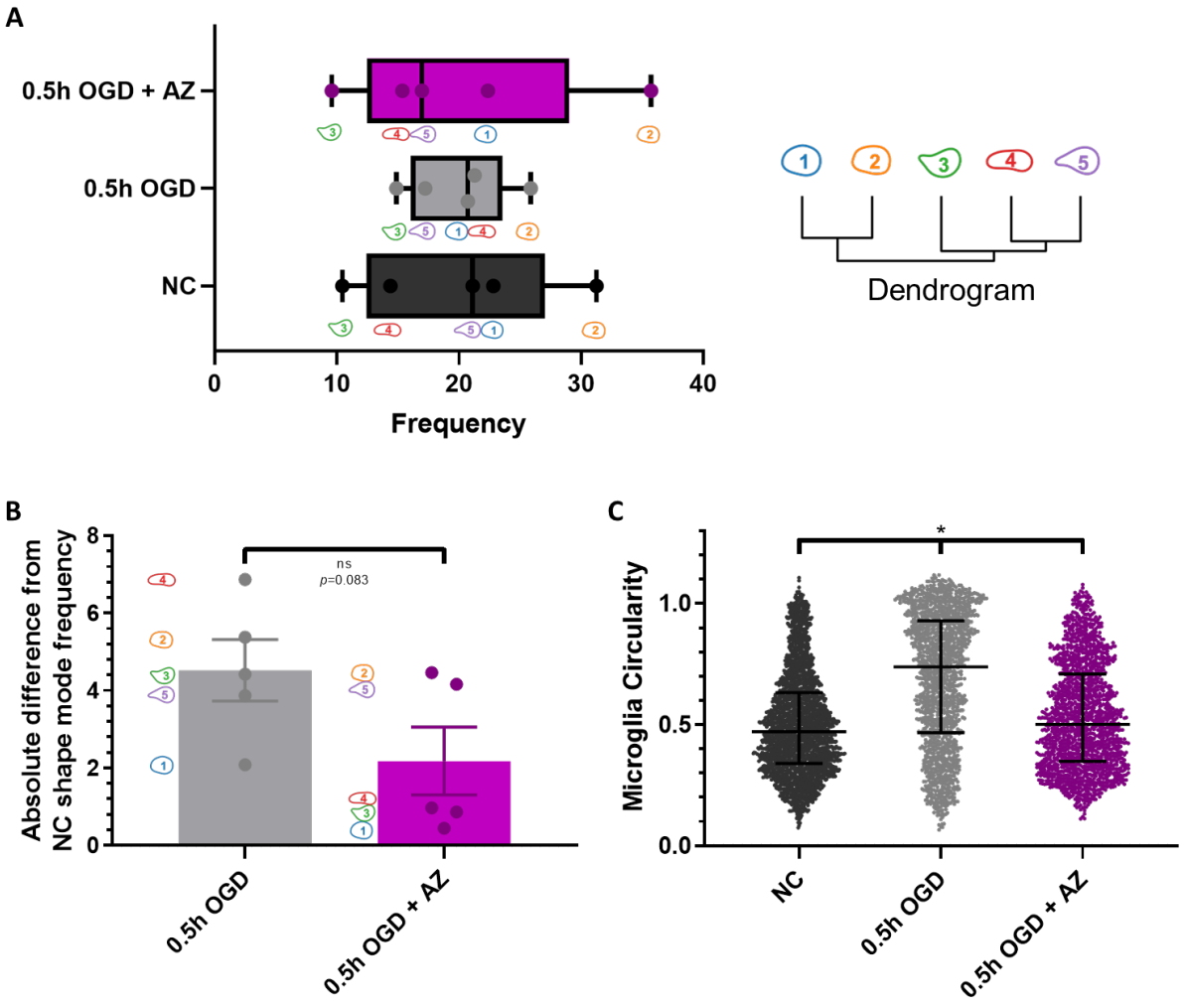

Figure 4.3 AZ reverses microglial heterogeneity and circularity after 0.5h OGD.
(A) Frequency of 5 shape modes of microglia for NC, 0.5h OGD, and 0.5h OGD+AZ groups as generated from the VAMPIRE package. (B) Absolute difference in shape mode frequencies of

0.5h OGD and 0.5h OGD+AZ from that of NC. (C) Microglial circularity of NC (n=2954 microglia from 4 slices), 0.5h OGD (n=1539 microglia from 5 slices), and 0.5h OGD+AZ (n=1612 microglia from 3 slices) conditions.

Table 4.1 Average circularity of microglia by shape mode for a given experimental condition.

Experimental Condition	Shape Mode					
	1	2	3	4	5	Average
NT	0.53	0.48	0.50	0.53	0.47	0.50
OGD	0.63	0.59	0.78	0.85	0.61	0.69
OGD+AZ	0.55	0.48	0.57	0.57	0.49	0.53

OGD enhances nanoparticle diffusion through the brain ECS

Nanotherapeutics must be able to reach target cells from the point of entry in the brain. To probe disease-mediated changes to the brain ECS and the effect on a nanoparticle's ability to move, we performed MPT with 40nm PS-PEG nanoparticles in ex vivo slices after OGD. Particle characteristics compared to a non-PEG coated particle are provided in Table 4.2. Mean squared displacements (MSD) were calculated for each particle trajectory from each video, and the geometrically ensemble-averaged MSD (<MSD>) for each experimental group was generated as a function of lag time (Figure 4.4A). Regardless of OGD duration, nanoparticles showed greater displacement, indicating an elevated ability to diffuse, compared to the NC group. Extraction of D_{eff} values using the Einstein-Smoluchowski Equation revealed a 16.7-, 16.5-, and 16.6-fold increase in nanoparticle diffusive ability in the 0.5h, 1.5h, and 3h OGD groups, respectively, compared to that of the NC group (Figure 4.4B). The <MSD> curves were then fit using the anomalous diffusion equation to obtain values of the anomalous diffusion exponent, α. Trajectories were classified as either superdiffusive (α>1.25), normal ($0.75 \leq \alpha \leq 1.25$), or subdiffusive ($\alpha$<0.75) (Figure 4.4C). All durations of OGD increased superdiffusive and decreased subdiffusive transport. The proportion of superdiffusive trajectories increased by 6.1% while subdiffusion decreased by 10.8% between the NC and 3h OGD groups. Changes in diffusion were region-dependent, however, with more severe disease-mediated effects in striatum than cortex (Figure 4.4D). The 0.5h, 1.5h, and 3h OGD exposure increased diffusion by 5.8-, 4.3-, and 4.5-fold, respectively, in the cortex compared to 27.8-, 38.0-, and 45.8-fold, respectively, in the striatum (Figure 4.4E). The regional and combined median D_{eff} and trajectory counts are presented in Table 4.3.

Table 4.2 Physicochemical properties of PS-PEG used in MPT and nanoparticle uptake studies.

Nanoparticles (n=3) were characterized in terms of hydrodynamic diameter, mean surface charge (ζ-potential), and the polydispersity index (PDI) by dynamic light scattering at 25°C and pH 7.2 in 10 mM NaCl. A non-PEG coated PS particle is included for comparison.

Nanoparticle Type	Number Mean ± SEM (nm)	Intensity Mean ± SEM (nm)	PDI	ζ-potential ± SEM (mV)
PS-COOH	39.1 ± 0.49	53.2 ± 0.58	0.044	-37.5 ± 0.74
PS-PEG	51.4 ± 0.96	66.9 ± 0.40	0.027	-0.59 ± 0.10

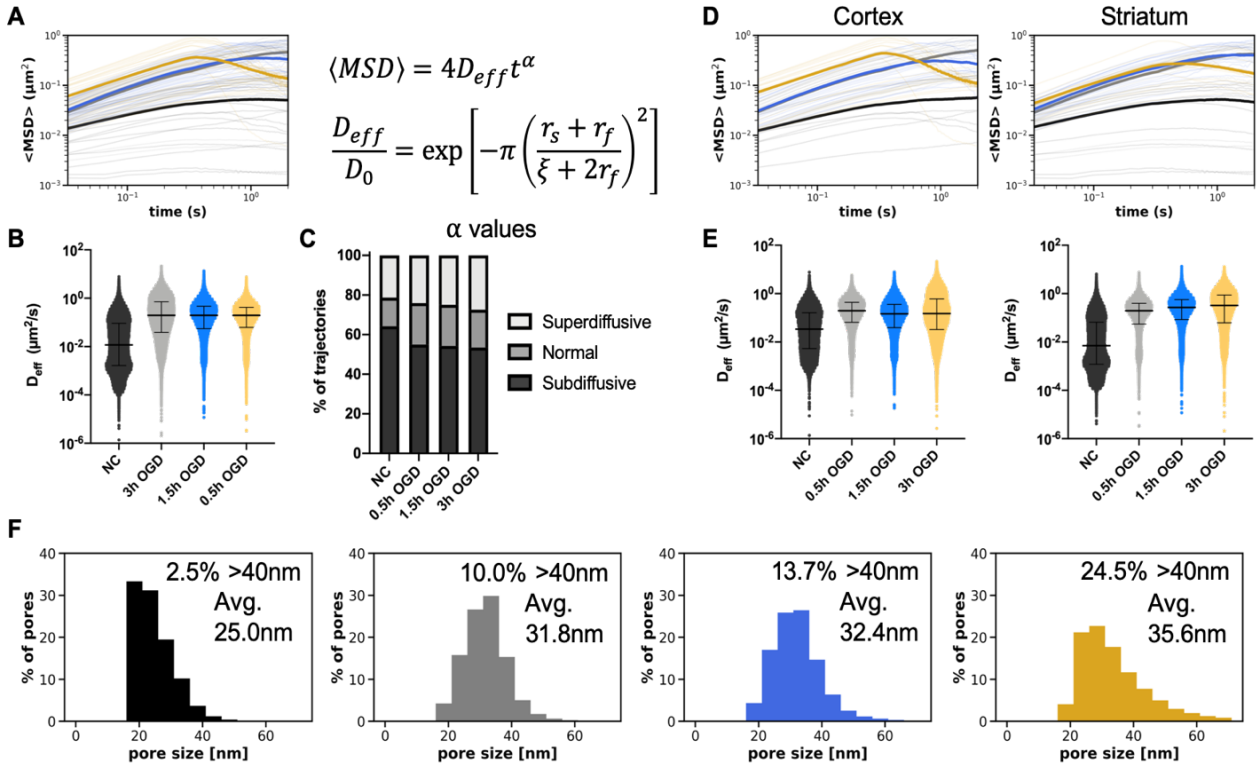

Figure 4.4 Characterization of nanoparticle diffusive behavior after OGD.
(A) Geometrically ensemble-averaged MSD vs lag time for NC (black), 0.5h (grey), 1.5h (blue), and 3h OGD (gold) conditions. Faint lines represent averages of each video (30 per group) and the bolded line represents the mean of all videos. (B) D_{eff} values extracted from each trajectory from all videos (n=10) in all slices (n=3) per group (1 dot = 1 trajectory). (C) The anomalous exponent α was calculated by fitting trajectory MSDs to the anomalous diffusion equation. α was used to classify trajectories as either superdiffusive, normal, or subdiffusive. (D) <MSD> vs lag time split by brain region (left: cortex, right: striatum). (E) D_{eff} values split by brain region: (left=cortex, right=striatum). (F) Effective ECS pore size distributions in NC and 0.5h, 1.5h, and 3h OGD slices from left to right. % of pores >40nm and average pore size are indicated by text. Data for B & E are reported as median ± interquartile range.

Table 4.3 Summary of multiple particle tracking in OGD slices.
D_{eff} in rat brain tissue were extracted at τ=0.303s from nanoparticle trajectories in the cortex (n=5 videos per slice) and striatum (n=5 videos per slice) in n=3 slices per group.

Treatment	Trajectories in Cortex	D_{eff} in Cortex ($\mu m^2/s$)	Trajectories in Striatum	D_{eff} in Striatum ($\mu m^2/s$)	Median D_{eff} ($\mu m^2/s$)
NC	24,382	0.0338	64,840	0.00707	0.0118
0.5h OGD	65,305	0.197	42,378	0.196	0.197
1.5h OGD	43,520	0.146	38,787	0.269	0.195
3h OGD	103,415	0.151	51,285	0.324	0.195

To estimate the distribution of effective ECS pores in each group, we fit the Amsden obstruction scaling model for entangled and cross-linked hydrogels [204] to the D_{eff} data in Figure 4.4B. As exposure to OGD increased, the distribution of pore sizes shifted to larger pores (Figure 4.4F). The percentage of pores larger than 40nm increased from 2.5% in the NC to 10.0%, 13.7%, and 24.5% in the 0.5h, 1.5h, and 3h OGD groups, respectively. Similarly, average pore size increased from 25.0nm (NC) to 31.8, 32.4, or 35.6nm (0.5h, 1.5h, and 3h OGD, respectively). Two final geometric features were calculated to better characterize nanoparticle behavior in the diseased brain microenvironment: trajectory boundedness and efficiency (Figure 4.5). Boundedness reflects the proportion of a trajectory which is restricted within a circular area, while efficiency reflects the ability of a nanoparticle to maximize displacement while minimizing distance traveled. 0.5h OGD caused a 1.1-fold decrease in boundedness and 6.1-fold increase in efficiency compared to that of NC. 1.5h and 3h OGD also increased efficiency by 6.4- and 5.4-fold, respectively, but elicited no fold-change on boundedness compared to that of NC.

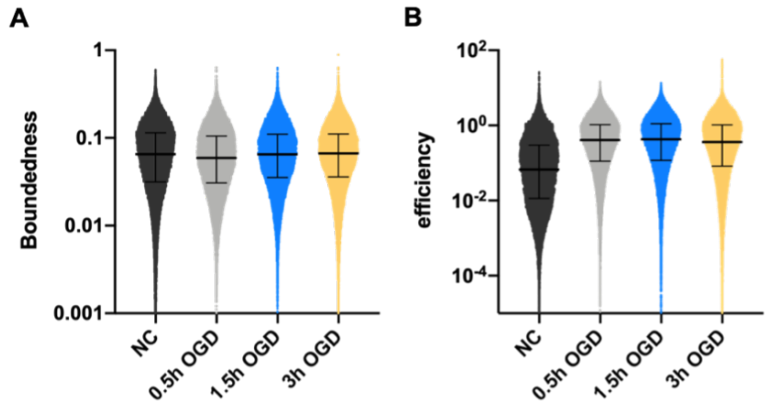

Figure 4.5 Supplemental geometric feature analysis of nanoparticle trajectories. Nanoparticle boundedness (A) and efficiency (B) calculated for each trajectory from all videos (n=10) in all slices (n=3) per group (1 dot = 1 trajectory).

Microglial uptake of nanoparticles is influenced by disease state and nanoparticle properties

We have confirmed OGD slice health can be recovered following AZ treatment and that particles up to 40nm in size can readily move within the OGD brain environment. Therefore, we next sought to understand how injury and treatment influence the interaction of PS-PEG, D-Cy5, and QD nanoparticles that reach microglial cells. Using flow cytometry, we determined the proportion of microglia which were nanoparticle-positive in each treatment condition. We showed a significant increase in microglial uptake of PS-PEG after OGD (PS-PEG: 0.47% NC vs 0.5h OGD 1.50%, p=0.016), and that AZ treatment reverted microglia to low-uptake behavior (PS-PEG: 0.59%) (Figure 4.6A). Application of 100x higher concentration PS-PEG showed similar trends, with 27.3%, 67.5%, and 40.4% uptake in microglial cells for NC, 0.5h OGD, and 0.5h OGD+AZ conditions (Figure 4.7). Microglial uptake of D-Cy5 (Figure 4.6B) and QDs (Figure 4.6C) however, did not exhibit significant differences across all three disease states. Importantly, QDs were internalized at much higher proportions than the other nanoparticle types across all treatment groups: median values for the 0.5h OGD group were 1.42%, 0.68%, and 25.0% for PS-PEG, D-Cy5, and QDs, respectively. Confocal images confirm that microglial uptake of nanoparticles occurred for all nanoparticle types and disease states.

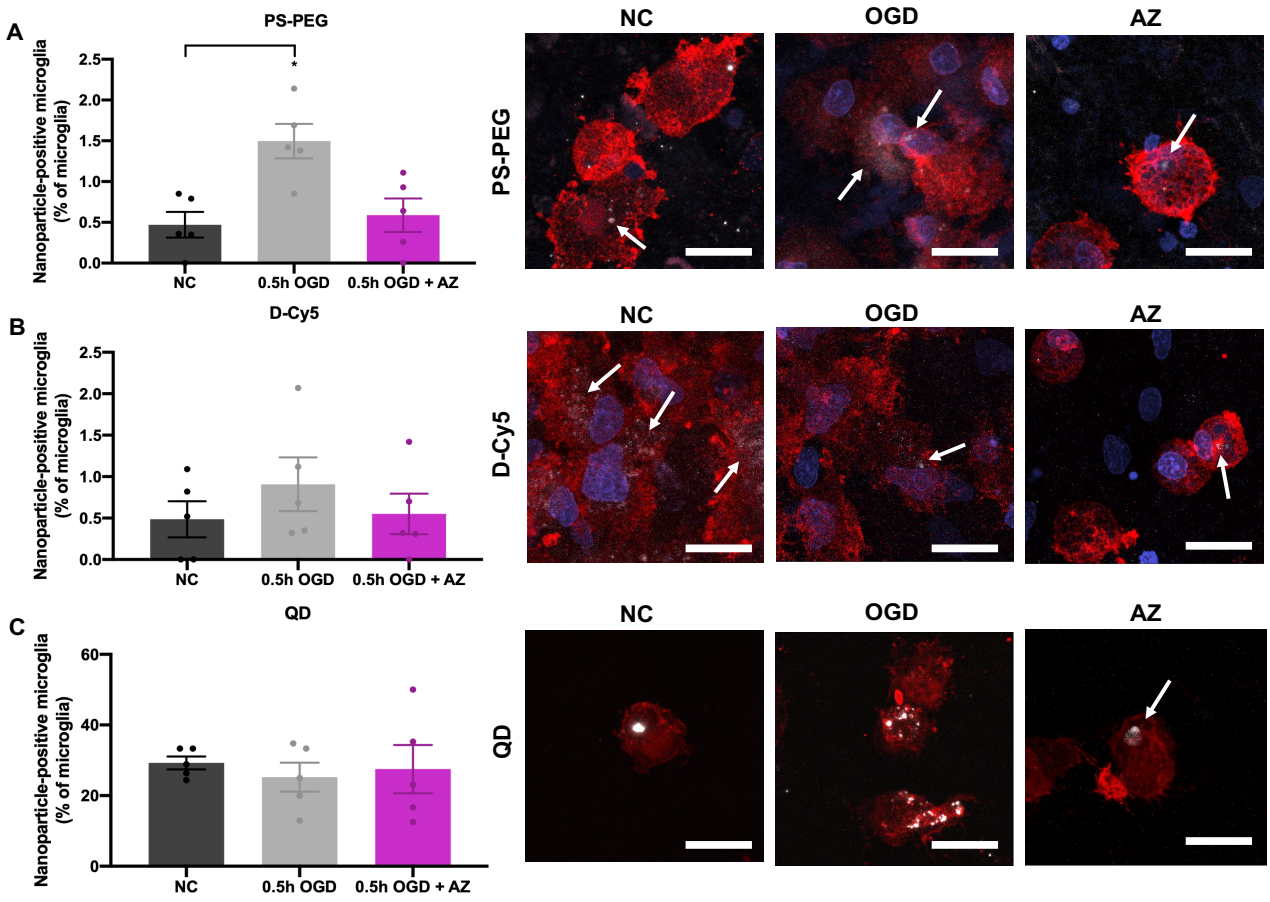

Figure 4.6 Microglial uptake of PS-PEG, D-Cy5, and QD nanoparticles at 5h for NC, 0.5h OGD, and 0.5h OGD+AZ conditions.
Flow cytometry results of (A) PS-PEG-positive, (B) D-Cy5-positive, and (C) QD-positive microglia as a proportion of all microglia in NC, 0.5h OGD, and 0.5h OGD+AZ groups. Co-localization of (A) PS-PEG nanoparticles (white), (B) D-Cy5 nanoparticles (white), and (C) QD nanoparticles (white) with NC, 0.5h OGD, and 0.5h OGD+AZ microglia (red) and cell nuclei (blue). All scale bars represent 20μm.

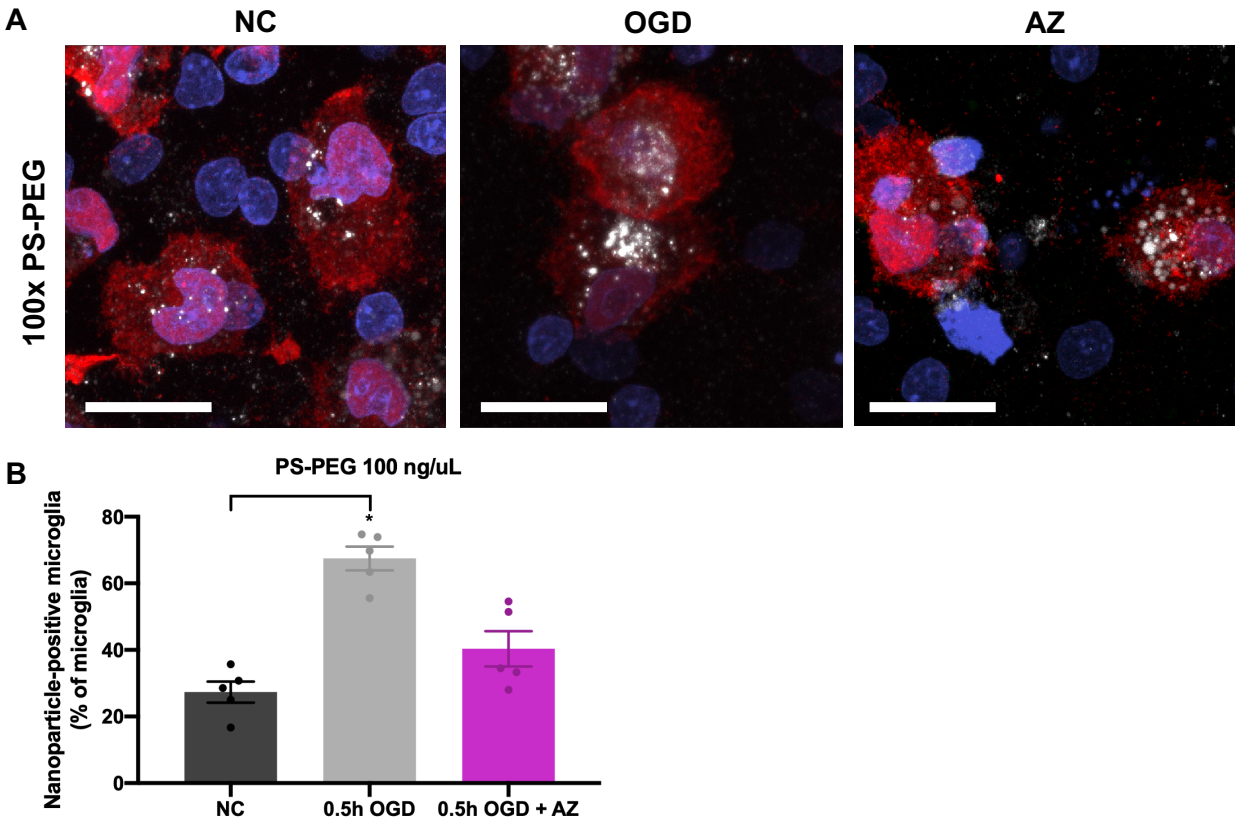

Figure 4.7 Supplemental analysis of microglial uptake of PS-PEG at a 100-fold increased dose.
(A) Representative confocal images of PS-PEG (white) and microglia (red) after administration of 100ng/μL (a 100-fold higher dose than the representative data in Figure 4.6). All scale bars represent 20 μm and cell nuclei (blue) are also shown. (B) Flow cytometry results indicate nanoparticle-positive microglia as a proportion of all microglia in each treatment group.

One important result from flow cytometry was the change in microglial number after injury in treatment. While microglia made up 20.33% of live cells in a NC slice, their proportion was significantly reduced after 0.5h OGD (3.99%), measured 5 hours after the end of injury ($p=0.016$). However, treatment with AZ increased microglial proportion to 14.70% ($p=0.016$ versus 0.5h OGD) (Figure 4.8A). Lower microglial percentage out of all live cells after 0.5h OGD was sustained for at least 25h (NC: 15.49%, 0.5h OGD: 4.00%, $p=0.024$) as determined by flow cytometry (Figure 4.8B), which was further supported by quantitation of microglial area to total cell number in confocal images at 24h after injury (Figure 4.8C). Interestingly, we observed a regional difference in microglial vulnerability. In the cortex, area covered by microglia did not change significantly across disease states (Figure 4.8D), but microglial area in the thalamus was significantly reduced after OGD ($p<0.001$). Treatment with AZ increased microglial coverage ($p=0.031$ compared to OGD), although still to a reduced level from NC

(p<0.001) (Figure 4.8E). Representative confocal images from each region are shown in Figure 4.6F.

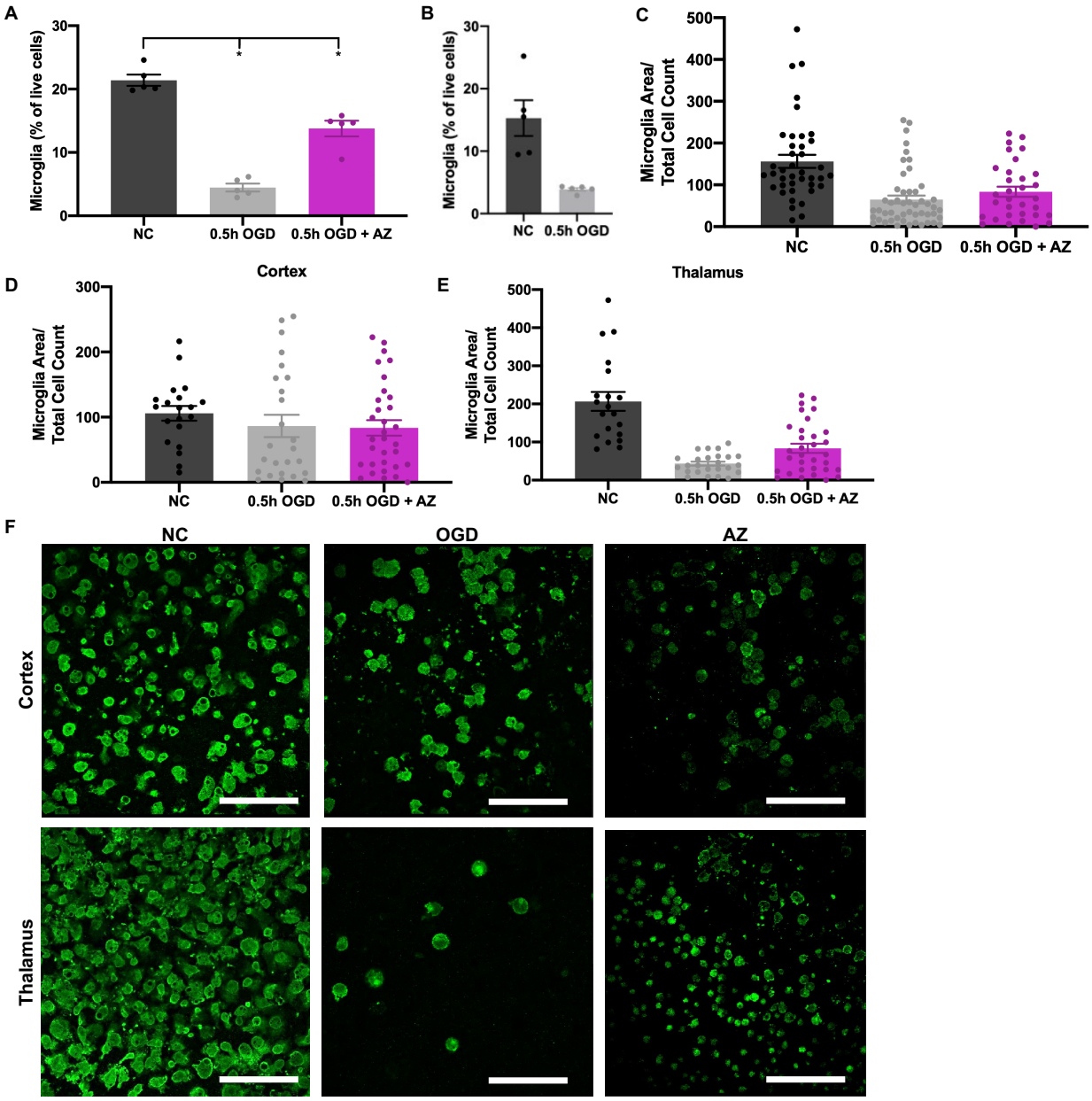

Figure 4.8 Microglial number decreases after OGD and is restored with AZ.
(A) Flow cytometry results of microglia as a proportion of all live cells in the NC, 0.5h OGD, and 0.5h OGD+AZ groups 5h after injury and (B) in the NC and 0.5h OGD groups 25h after injury. (C) Microglial area of NC, 0.5h OGD, and 0.5h OGD+AZ slices normalized to DAPI-positive cell count from images at 24h after injury for all images, (D) cortex alone, and (E) thalamus alone. (F) Representative images of microglia (green) in the cortex and thalamus of NC, 0.5h OGD, and 0.5h OGD+AZ slices. All scale bars represent 100μm.

4.3 Discussion

In this study, we investigated the nanoparticle- and disease-dependent nature of nanoparticle-cell interactions in the brain microenvironment using an OWH brain slice model of ischemic brain injury. Our first goal was to modulate ischemic brain injury severity by increasing OGD exposure times. There was an increase in cytotoxicity for all OGD exposure times compared to that of NC. Surprisingly, 1.5h and 3h OGD exposure times resulted in lower cytotoxicity than 0.5h OGD exposure. Previous studies have demonstrated an increase in cytotoxicity from 0.5h to 1h of OGD *ex vivo*, and 60min is regarded as the timeframe of OGD-induced neuronal swelling followed by apoptotic and necrotic death [205-208]. In our study, exposure to 0.5h OGD was sufficient to induce significantly different outcomes than the NC condition, in agreement with other findings [193, 209, 210]. Considering OGD mediates damage via oxidative stress, we measured the concentration of the redox buffering molecule GSH as another measure of slice health [211]. All OGD exposure times reduced GSH concentrations, representing an oxidatively stressed, unhealthy environment [212].

Microglia are potent cellular targets for drug delivery, due to their role in propagating neuroinflammation after ischemic injury. Previous studies have demonstrated microglia-specific drug delivery with PAMAM dendrimers, which was attributed to the increased phagocytic behavior of microglia in an activated state [30, 133, 213]. Increased microglial uptake of dendrimers is also present after HI in mice *in vivo*, retinal HI injury in mice *in vivo*, and *in vivo*-induced cerebral palsy rabbits *ex vivo* [112, 214, 215]. In all three studies, microglia exhibited robust activation and proliferation, which was associated with an amoeboid cell shape, pro-inflammatory phenotype, and increased phagocytic behavior. However, in our study, dendrimer uptake was not significantly changed and no microglial proliferation occurred compared to that of the NC condition. In fact, microglial area from confocal images and microglial counts from FACS indicate a decrease in microglial number after OGD. One key difference is the lack of a global inflammatory response in our *ex vivo* slice preparation process. Without systemic inflammatory contributions such as peripheral immune cell invasion, OGD alone may be insufficient to mediate microglial proliferation [216-219]. Thus, one major limitation of inducing injury *ex vivo* is the inability to fully represent complex pathological processes such as neuroinflammation. Future studies may overcome this limitation by incorporating a strong inflammatory stimulus *in vivo* before brain extraction.

Microglial phenotypes in slice culture models are different than those represented *in vivo* [220] and several studies have shown that nanoparticle uptake is correlated to microglial phenotype [221, 222]. Accumulating evidence shows the importance of shape in characterizing

microglial phenotype [223, 224], supporting further microglial characterization using shape modes, surface marker presentation, transcriptomics, or cytokine expression. Improving microglial characterization is essential to understanding microglial-nanoparticle interactions, especially as the classical M1 and M2 microglial polarization phenotype schema progressively phases out [225]. To better characterize the range of microglial morphologies in our OGD slice model, we used computer-aided morphological analysis. These results showed that 0.5h OGD induced changes in microglial shape modes, which were reversed back to NC shape mode distributions upon AZ treatment. AZ has previously been shown to promote an anti-inflammatory phenotypical change of macrophages and microglia [196]. Although some variation in frequency for the 5 shape modes remained after AZ treatment, the ranking of shape mode frequencies from least (3) to greatest (2) followed the same ranking as the NC microglia shape mode frequencies. The VAMPIRE package enables in-depth morphological analysis and detection of nuances in microglial shapes that encompass the heterogeneity of microglia that the human eye cannot detect. However, extracting intuitive shape characteristics of microglia from VAMPIRE as opposed to broad trends is non-trivial given the complexity in interpreting the large dataset "machine-vision" classifications of the VAMPIRE package [121]. Independent of shape mode, one readily interpretable morphological distinction between groups was that of microglial circularity, where high circularity corresponds to microglia assuming a non-branching amoeboid morphology characteristic of a pro-inflammatory activated state [224]. Although a value of 1 describes a perfect circle, some circularity values (1.2% of NC, 14.3% of 0.5h OGD, and 1.6% of 0.5h OGD+AZ) are slightly above 1 (1.12 max) due to errors in computer estimation of pixel perimeters [226]. We found that 0.5h OGD increased microglial circularity while AZ prevented amoeboid morphology, reducing circularity levels to closer to that of NC microglia. Further work may better determine the association between nanoparticle uptake and microglial morphological phenotype by analyzing additional cell features, such as degree of branching, branching polarization, length of branching, and soma size, especially for nanoparticle-containing cells.

In contrast to dendrimers, PS-PEG nanoparticles exhibited increased microglial accumulation after OGD, and QDs were internalized at roughly equal proportions regardless of disease state. It is remarkable that QDs were able to achieve orders of magnitude higher microglial accumulation after administration at the same dose as PS-PEG and D-Cy5. Our results indicate that microglial phagocytosis is highly dependent on nanoparticle platform, and disease-induced changes in microglial behavior are not leveraged equally among all nanoparticle types. These platforms differ in size, rigidity, and chemical composition which can influence nanoparticle-cell interactions [227, 228] suggesting that nanoparticle physicochemical

parameters must be well-tuned to achieve accumulation in target cells at sites of injury. For example, rigid lipid nanoparticles can more easily penetrate cell membranes compared to less rigid nanoparticles [229]. Previous work also supports microglial uptake of high-rigidity nanoparticles, namely gold nanoparticles *in vitro* and silica and QD nanoparticles *ex vivo* and *in vivo* [113, 230, 231].

Nanoparticle diffusive ability also plays a role in reaching target microglial cells and in achieving maximal therapeutic impact [232, 233]. As evidenced by the MPT results after exposure to OGD, PS-PEG nanoparticles exhibited more than 16-fold higher diffusive ability compared to the NC condition. Although we only directly confirmed diffusivity for PS-PEG, PEGylated QDs and PAMAM dendrimers have also been shown to move effectively within the brain parenchyma in healthy [83] and diseased states [132, 133]. After OGD, PS-PEG nanoparticle trajectories were more efficient and the population of particles behaving subdiffusively decreased. This shift in diffusive transport modes may be associated with other disease-mediated changes. For example, OGD-induced cytotoxicity might reduce cell density and therefore decrease the likelihood of subdiffusive transport, which is characteristic of nanoparticles closely interacting with cellular compartments. Macroscopic ECS changes after *ex vivo* ischemic injury have also been previously reported, including an increase in striatal tortuosity and decrease in ECS volume fraction of brain tissue in the hippocampus and cortex [234, 235]. For example, the formation of dead-space domains may explain both an increase in estimated ECM pore size and tortuosity [236]. OGD also potentially increases the expression of ECM-degrading matrix metalloproteinases (MMPs), as demonstrated in models of cerebral ischemia [237]. The increase in ECM-degrading enzymes can lead to larger pore sizes and subsequently increase nanoparticle diffusion in the ECS. In this study, the distribution of ECS pore sizes did in fact shift to larger pores following OGD, which could be leveraged by the PEGylated nanoparticles for effective diffusive transport through injured tissue.

The proportion of pores greater than 40nm increased with increasing exposure of OGD. Interestingly, an appreciable percentage of pores were predicted to be smaller than 40nm, the particle diameter. Neutrally charged 40nm PS-PEG nanoparticles can evade many of the mechanisms by which ECM hinders extracellular movement [83], making diffusion predominantly influenced by steric interactions. While it is likely that some populations of particles are truly immobilized within pores, the Amsden obstruction model may be underestimating pore size by assuming nanoparticles are completely inert. PEGylated nanoparticles may interact with microglia, other cell types, and various components of the ECM. Regardless, the model was applied equally across all experimental groups and therefore still

provides insight into the differences existing between them. Additionally, the range of pore sizes identified in this study is similar to previous findings using MPT analysis in brain slices [117]. Furthermore, since we only measured diffusion of 40nm particles compared to the 40nm, 100nm, and 200nm particles used by Nance *et al*. [83], we likely underestimated the true size of pores >40nm. Nanoparticle probe size, different culturing conditions, and DIV can each alter MPT analysis and the application of the Amsden obstruction model, requiring further investigation in the OGD model.

One benefit of the OWH slice platform for furthering these studies is the ability to study regional variability in response to injury. After both 1.5h and 3h OGD, nanoparticles in the striatum had consistently faster D_{eff} compared to those in the cortex. Microglial area coverage also indicated a greater injury response in the midbrain. Only the thalamus, not the cortex, showed a decrease in microglial area coverage after 0.5h OGD. Although we did not probe for a mechanism to explain regional differences, such investigation can have important implications for therapeutic development. One recent study investigated the injury-resistant nature of the hypothalamus region and identified that slow neuronal depolarization in the region may be one native mechanism of neuroprotection [238]. Enhanced therapeutic penetration within specifically diseased brain regions could reduce requisite dose amount and frequency and avoid inadvertent cytotoxicity on healthy tissue. Due to the intricate balance of pro- and anti-inflammatory activity in the brain microenvironment after disease, over-scavenging of reactive oxygen species or excessive inhibition of inflammatory processes could interrupt healthy cellular function or exacerbate damage [239-241]. Given that ischemic injury manifests in multiple phases and in regional patterns [49, 108], the continued investigation of regional variations in the brain could inform therapeutic strategies for specific regional targets, which would be highly advantageous in combating immediate and ongoing disease sequelae.

Further cross-platform investigation will be important to elucidate advantageous nanoparticle characteristics, in addition to diffusive ability, size, rigidity, and surface functionalization, for microglial-targeted drug delivery after injury. Microglial uptake of additional nanoparticle platforms, such as nanocrystals or polymeric micelles, has been understudied yet may elucidate new therapeutic avenues. Importantly, immediate AZ treatment of OGD-injured slices returned microglial uptake behavior of all nanoparticle types closer to that of NC conditions, suggesting that modulated microglia of recovered brain tissue behave similarly to healthy microglia. While this work primarily studied AZ modulation of slice health and microglial behavior, we also demonstrated that application of SOD or AZ is neuroprotective after ischemic injury. Brain slices treated with either therapeutic had significantly reduced cell death over 24h,

and AZ additionally prevented a decrease in GSH concentration, indicative of an inhibition of oxidative stress and cell damage. SOD efficacy is due to its scavenging of superoxide anion which is implicated in excitotoxicity, but the exact mechanism of AZ therapeutic efficacy remains to be elucidated in the brain [242, 243]. Regardless of therapeutic mechanism, therapeutic reversion of OGD-induced microenvironment offers promising implications for drug delivery strategies. If SOD or AZ were delivered via rigid carriers similar to PS-PEG nanoparticles that exhibited increased diffusion and microglial uptake after OGD exposure, drug distribution would favorably accumulate in diseased regions. After therapeutic release and reduction of disease phenotype, subsequently administered nanoparticle doses would preferentially sequester in ongoing injury sites compared to recovering or healthy tissue environments. Further investigation of strategies to modulate nanoparticle diffusivity and microglial uptake may result in more effective methods of nanoparticle-mediated therapeutic delivery.

4.4 Conclusion

In this work, we probed the effect of OGD-induced disease and AZ treatment on nanoparticle interactions with microglia in the brain microenvironment. First, we determined the effect of OGD exposure on cell death and oxidative stress, markers of injury severity. We observed significant injury responses after 0.5h OGD exposure: 54.3% increase in cytotoxicity, 1.7-fold decrease in GSH concentration, and larger pore distribution in the ECS. From image analysis, we observed an OGD-induced shift in microglial morphology towards more heterogeneity in shapes with overall increased circularity and a decrease in microglial density. Nanoparticle interactions with microglia were dependent on both the nanoparticle platform as well as injury state. After 0.5h OGD, microglial internalization of PS-PEG was increased, but uptake of QDs or dendrimers was not enhanced, indicating an important role of nanoparticle material identity in determining extent of phagocytosis after injury. PS-PEG nanoparticles exhibited a 16.7-fold increase in diffusion after 0.5h OGD compared to that of NC. Treatment with AZ not only effectively reduced OGD cytotoxicity and GSH depletion, but also reverted nanoparticle uptake behavior of PS-PEG and microglial morphology towards that of NC. This study shows OWH slices enable region-dependent nanoscale probing of live tissue to identify cellular and microstructural changes in diseased and recovering brain microenvironments that can be leveraged for cell-specific uptake of nanoparticles. Additionally, we demonstrate that in ischemic conditions, nanoparticle fate is platform-dependent, providing insights into therapeutic strategy for targeting microglial cells to combat neurological disease.

In the next chapter, we continue our investigation of brain-targeted polymeric nanoparticles, but return to the biodegradable platform introduced in Chapter 3. We explore whether modulation of surfactant type in the PLGA-PEG nanoparticle formulation process can influence nanoparticle uptake into the brain, microglia, and neurons. Nanoparticles with improved brain-penetrating properties can be broadly applied to the treatment of many neurological disorders.

Chapter 5 – Surfactant effects drive nanoparticle penetration and cellular uptake in the brain

If the brain were so simple we could understand it, we would be so simple we couldn't.
– Lyall Watson

When I began this project five years ago, I thought we were asking a simple question: are some surfactants better than others, in the context of nanoparticle drug delivery to the brain? What began as *ex vivo* screening, as in Chapter 4, became more interesting when we looked *in vivo*, and required a better understanding of the nanoparticles *in vitro*, which we did in collaboration with Scott (mass spectrometry) and Daniel (surface analysis). This project has brought me more failed experiments & manuscript rejections than any other thesis chapter, but it has also been where I've learned the most as a scientist.

5.1 Introduction

The brain's uniquely restrictive biological barriers, including the BBB and brain parenchyma, make target cells within the brain inaccessible to nearly all therapeutic molecules. While invasive delivery techniques like intraparenchymal injection can increase therapeutic accumulation in the brain, a need remains for noninvasive delivery strategies. Nanotechnology is one promising avenue for systemic delivery of neurotherapeutics since nano-sized particles can overcome transport barriers and achieve accumulation within the brain [244, 245]. Recently, drug-loaded nanoparticles have demonstrated efficacy in models of glioblastoma [246], neurodegenerative disorders [247], and neonatal hypoxic-ischemia [248], among other brain injuries [249, 250].

For effective therapeutic delivery in the brain, nanoparticles must be designed to have biologically advantageous properties. As described in previous chapters, PLGA-PEG nanoparticles present advantages of biodegradability, reduced protein adsorption, and enhanced nanoparticle diffusivity in the brain ECS. Since nanoparticle surfaces mediate interactions between the nanoparticle and biological environment, further surface functionality can be added to PLGA-PEG nanoparticles to improve cell penetration or cell-specific targeting.

One important class of molecules present at nanoparticle surfaces are surface acting agents, referred to as surfactants. During the formulation process of PLGA-PEG nanoparticles, surfactants are commonly introduced to reduce surface tension at the interface between the organic polymer solution and the aqueous phase. Although nanoparticles can be formulated without surfactants [251], these molecules promote nanoparticle formation and stabilization. Additionally, studies have shown that surfactant coatings can alter nanoparticle-cell interactions. Tween surfactants, especially Tween 80 (or polysorbate 80, P80), can specifically enhance nanoparticle accumulation in the brain [252]. Pluronic surfactants, including poloxamer 188

(Pluronic® F68, F68) and poloxamer 407 (Pluronic® F127, F127), are able to inhibit P-glycoprotein efflux transporters [253-255]. However, nearly all prior studies have evaluated surfactant effects after incubating previously-formulated nanoparticles in fresh surfactant solutions to produce a dense surface coating. Moreover, none have investigated nanoparticle diffusion past the BBB, which has dependence on surface presentation of PEG [256]. We hypothesized that nanoparticles formulated with PEG and surfactants may be optimally designed for transport to and within the brain.

In the present study, we compared PLGA-PEG formulations with surfactants P80, F68, and F127 to a control formulation without surfactant in deionized (DI) water. We also studied the surfactants poly(vinyl alcohol) (PVA), the most commonly used surfactant for nanoparticle stabilization [257], and cholic acid (CHA), an anionic surfactant [114]. With each formulation, we evaluated nanoparticle transport in the brain at multiple time and length scales, i.e. molecular-level diffusion as well as cellular- and whole organ-scale nanoparticle accumulation. Our results provide insight into nanoparticle design for improved penetration of biological barriers for therapeutic delivery in the brain.

5.2 Results

Surfactants and PEG enhance nanoparticle stability and diffusive ability

To isolate the role of surfactant on biodistribution, cellular uptake, and diffusive ability, we controlled for nanoparticle size and surface charge. Based on previous work, colloidally stable nanoparticles with hydrodynamic diameters below 114 nm and near-neutral zeta ζ-potential can transport efficiently to and within the brain [83, 258]. The formulations used in this study had average diameters between 55-69 nm and ζ-potentials between -6.5 and -3.0 mV (Table 5.1). The PEG layer and surfactant molecules decrease nanoparticle aggregation and increase stability, which is indicated by low polydispersity indices (PDI < 0.20) of formulations with both PEG and surfactant. However, nanoparticles without PEG (PLGA/F127) or surfactant (PLGA-PEG/DI) had elevated PDIs of 0.20 and 0.22, respectively. Using mass spectrometry, we confirmed that surfactant molecules compose a low weight percent of the PLGA-PEG/P80 (0.01%) and PLGA-PEG/CHA (0.005%) formulations (Supplementary Figure 1). Although we expect surfactant concentration to be similarly low in the other formulations, we were unable to quantify those contributions due to limitations of mass spectrometry with polydisperse polymer species [259].

To probe molecular-scale interactions in the brain microenvironment, we characterized the diffusive ability of each nanoparticle formulation in 300 μm brain slices prepared from

healthy rats. More extensive analysis of nanoparticle diffusion is presented in the following sections, but ensemble-averaged effective diffusion coefficients (D_b), its fold-change compared to theoretical nanoparticle diffusion in artificial cerebrospinal fluid (D_{aCSF}), and the number of analyzed trajectories are included as summary statistics in Table 5.1. The results indicate rapid transport of nanoparticles with anionic surfactant molecules (PLGA-PEG/CHA, D_b=21.7x10^{-4} μm^2/s) or without surfactant (PLGA-PEG/DI, D_b=12.9x10^{-4} μm^2/s). Diffusion of non-PEGylated nanoparticles with surfactant (PLGA/F127, D_b=1.02x10^{-4} μm^2/s) is significantly hindered, in alignment with previous studies on the importance of a PEG layer for enhanced diffusive behavior [117].

Table 5.1 Physicochemical properties and diffusivity of PLGA-PEG nanoparticles formulated with biocompatible surfactants.
Nanoparticles were characterized in terms of hydrodynamic diameter, mean surface charge (ζ-potential), and the polydispersity index (PDI) by dynamic light scattering at 25°C and pH 7.2 in 10 mM NaCl. All values are reported as mean ± standard error of the mean (SEM) (n=3). Effective diffusion coefficients in rat brain tissue (D_b) were extracted at a τ = 0.8 s from nanoparticle trajectories over fifteen videos across three brain slices for each formulation, and compared to theoretical nanoparticle diffusion in artificial cerebrospinal fluid (aCSF) based on the Stokes-Einstein equation and mean particle diameter.

Polymer/ Surfactant	Number Mean ± SEM (nm)	PDI	ζ-potential ± SEM (mV)	Ensemble D_b (x10^{-4} μm^2/s)	D_{aCSF}/D_b	Number of Trajectories
PLGA/ 1% F127	68.2 ± 4.0	0.20	-6.28 ± 0.3	1.02	94,000	557
PLGA-PEG/ 1% P80	59.6 ± 1.5	0.08	-3.63 ± 0.8	4.72	23,000	568
PLGA-PEG/ 5% F68	65.5 ± 4.1	0.09	-4.33 ± 0.4	5.98	17,000	569
PLGA-PEG/ 1% F127	59.7 ± 1.3	0.08	-4.06 ± 1.4	7.50	15,000	839
PLGA-PEG/ 5% PVA	65.3 ± 2.4	0.11	-3.24 ± 0.9	8.48	12,000	339
PLGA-PEG/ DI H_2O	55.0 ± 2.9	0.22	-4.58 ± 0.6	12.9	9,000	590
PLGA-PEG/ 3% CHA	56.2 ± 3.0	0.17	-6.11 ± 0.6	21.7	5,000	308

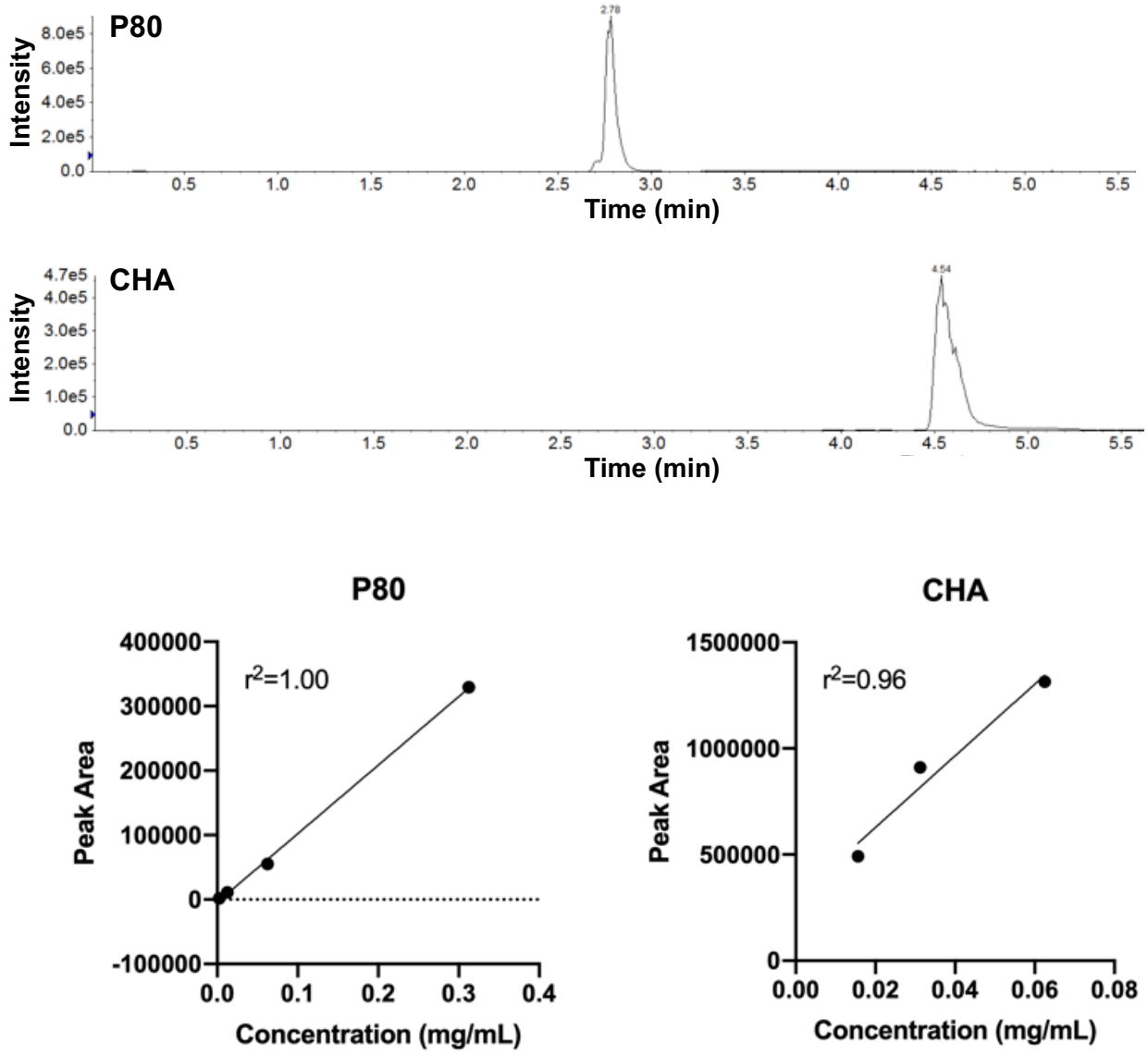

Figure 5.1 Mass spectrometry analysis of surfactants P80 and CHA.
Surfactants P80 and CHA were quantified by comparison of peak area to a calibration curve of known standards.

Nonionic surfactants result in decreased cellular uptake and diffusivity ex vivo

Organotypic brain slices enable high-throughput assessment of nanoparticle behavior in the brain, as slices retain multicellular complexity and 3D architecture without *in vivo* barriers which limit nanoparticle penetration to the brain [260]. We first quantitatively assessed nanoparticle uptake into microglia within 4h of exposure by flow cytometry (Figure 5.1A). The results showed uptake of PLGA-PEG/DI nanoparticles in 25.2% of microglia, and significantly reduced internalization rates 11.0%, 13.2%, 8.6%, 10.1%, 12.1%, and 12.9% for PLGA-PEG/CHA, F68,

F127, P80, PVA, and PLGA/F127, respectively. No significant differences exist between nanoparticles formulated with surfactant. We investigated cytotoxicity as a potential confounding factor in nanoparticle uptake studies, since cells exposed to a high surfactant dose would undergo cell death [261] and therefore not be counted in flow cytometry analysis. Using propidium iodide staining (Figure 5.1B) and lactate dehydrogenase release (Figure 5.2A) as two measures of cell death after four hours of nanoparticle incubation, all samples were within a normal 5-25% cytotoxicity range. Figure 5.2 also shows qualitative confirmation of nanoparticle uptake within neurons and microglia in the 4h experimental window.

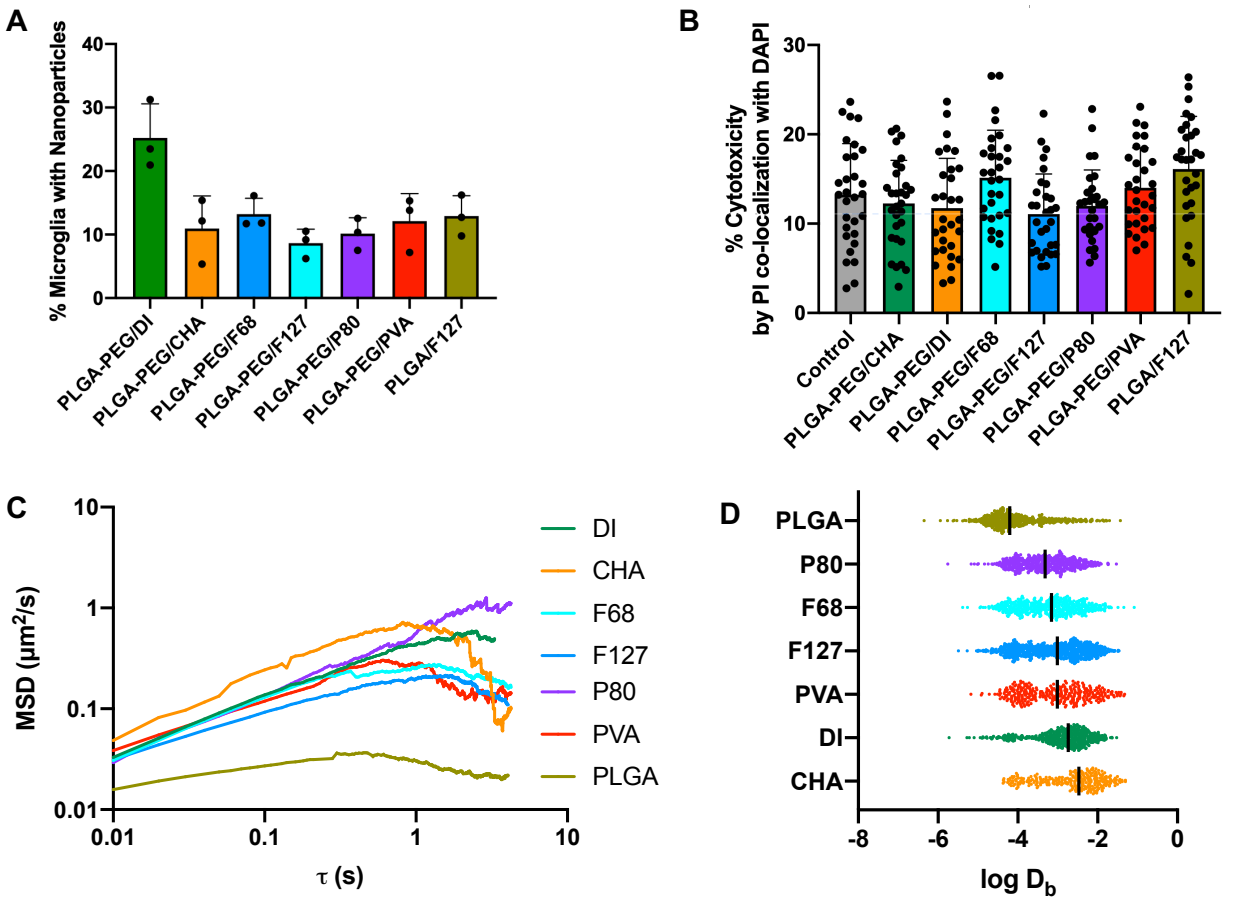

Figure 5.1 Assessment of surfactant effects on nanoparticle transport in organotypic brain slices.
(A) Flow cytometry analysis indicate that all formulations with surfactant demonstrated similar levels of microglial uptake within 4 h, while PLGA-PEG/DI achieved significantly elevated levels of uptake. (B) Propidium iodide (PI)-positive cell counts, as a proportion of total cells, demonstrate no significant differences in cytotoxicity across all treatment conditions. (C) Nanoparticle trajectories were analyzed to calculate ensemble-averaged mean squared displacement at time lags up to 6.5 s. (D) Log of D_b at 0.8 s were extracted for each trajectory (1 dot = 1 trajectory).

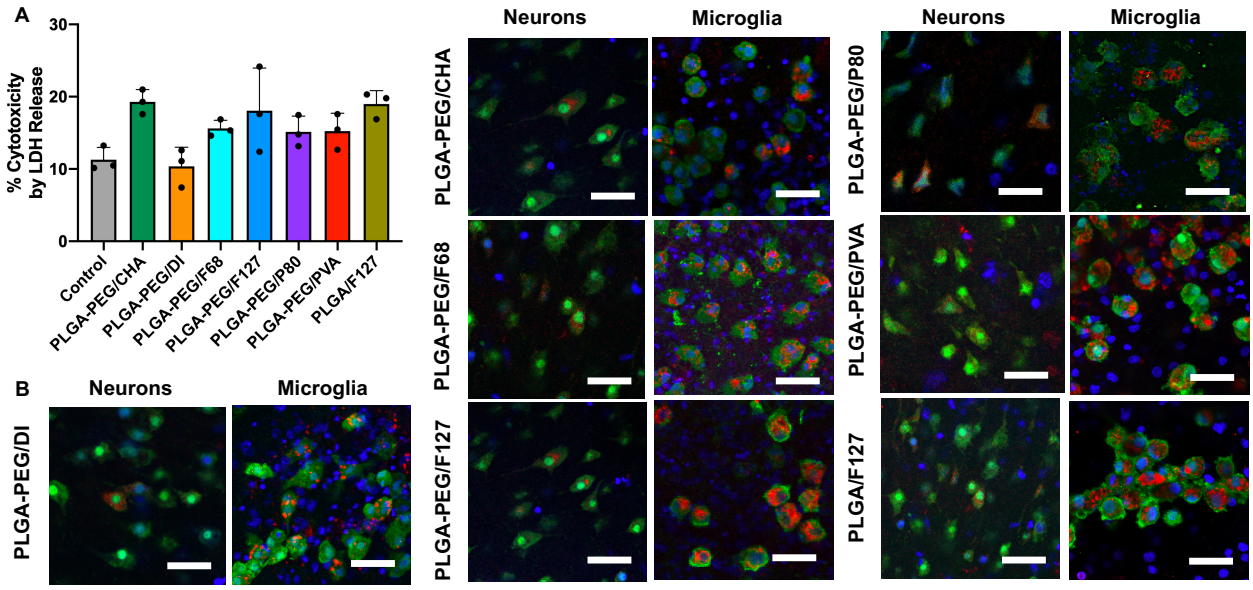

Figure 5.2 Supplementary assessments of nanoparticle transport in organotypic brain slices.
(A) Lactate dehydrogenase (LDH) release indicates no toxic effect of nanoparticle exposure; cytotoxicity is within a normal 5-25% range. (B) All nanoparticle formulations (red) are observed in neurons (left, green) and microglia (right, green). All cell nuclei (blue) are stained with DAPI and all scale bars represent 20 μm.

We applied each nanoparticle formulation to organotypic brain slices and subsequently analyzed several hundred nanoparticle trajectories to extract diffusion information. At shorter length and time scales, nanoparticle transport is governed by diffusion. Each PLGA-PEG formulation demonstrates a positive slope of ensemble-averaged mean squared displacement (<MSD>) over time, while the PLGA/F127 formulation shows more stagnant growth (Figure 5.1C), indicating limited diffusive ability. At a time interval of 0.8 seconds, D_b were extracted for each trajectory (Figure 5.1D). The ensemble-averaged D_b for each formulation at this time scale are available in Table 5.1. The D_b distributions indicate significantly enhanced diffusive ability of PLGA-PEG nanoparticles with the anionic surfactant CHA compared to no surfactant ($p<0.0001$). However, the presence of nonionic surfactants reduced diffusive ability: compared to PLGA-PEG/DI nanoparticles, we observed 1.52-fold, 1.72-fold, 2.16-fold, and 2.73-fold slower diffusion with the PLGA-PEG/PVA, PLGA-PEG/F127, PLGA-PEG/F68, and PLGA-PEG/P80 formulations, respectively. Although the reductions were statistically significant ($p<0.001$ for all), the effect of surfactant incorporation was much smaller than the effect of the PEG layer. Without a PEG layer, nanoparticles appeared immobilized in the brain: PLGA-PEG/F127 nanoparticles exhibited 7-fold increased diffusive ability compared to PLGA/F127 nanoparticles ($p<0.0001$).

Individual trajectories were then analyzed for geometric features to distinguish between subtypes of diffusive transport. Characterization of the <MSD> curves showed that PLGA/F127 trajectories exhibited subdiffusive behavior more frequently than any other formulation, while the PLGA-PEG/DI and PLGA-PEG/CHA formulations were more likely to demonstrate superdiffusive behavior (Figure 5.3A). These results were closely aligned with extraction of α, the anomalous diffusion coefficient, for each nanoparticle trajectory. The plurality of PLGA/F127 trajectories were classified as subdiffusive ($\alpha<1$) while most PLGA-PEG/DI and PLGA-PEG/CHA trajectories had normal ($\alpha=1$) diffusive behavior (Figure 5.3B). Average trappedness, a geometric feature which describes the probability of the nanoparticle being trapped within a given radius, was highest for the PLGA/F127 nanoparticles and lowest for PLGA-PEG/DI nanoparticles (Figure 5.3C). Conversely, PLGA/F127 nanoparticles were least efficient – that is, each time step resulted in small net displacements – while PLGA-PEG/DI nanoparticles were most efficient (Figure 5.3D). For each geometric feature, all formulations with surfactants existed on a continuum between the immobilized PLGA/F127 nanoparticles and the diffusive PLGA-PEG/DI nanoparticles. Therefore, the results of multiple particle tracking (MPT) indicate that the inclusion of nonionic surfactants in nanoparticle formulations will increase the likelihood of cellular interaction – indicated by increasing subdiffusion, trappedness, and decreasing efficiency – at short length and time scales.

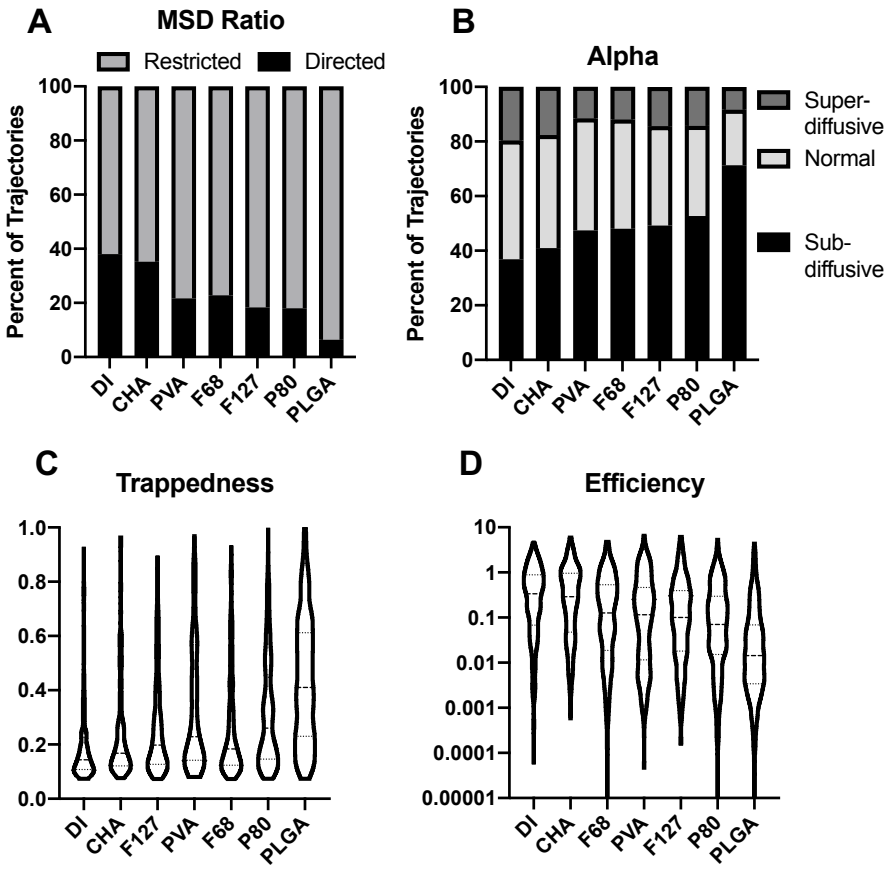

Figure 5.3 Geometric analysis of nanoparticle diffusion trajectories.
(A) The aspect ratio of the MSD curve for each trajectory was extracted and classified as subdiffusive (<0) or superdiffusive (>0). (B) The anomalous exponent α was extracted for each trajectory and classified as superdiffusive (>1), normal (1), or subdiffusive (<1). The (C) trappedness and (D) efficiency of each trajectory was calculated and plotted as violin plots.

Nonionic surfactants enhance BBB permeation and accumulation in the brain

Beyond diffusion and cellular internalization, nanoparticle fate in the brain is dependent on favorable circulation kinetics, biodistribution, and transport across the BBB. These outcomes must be assessed *in vivo*. We administered each PLGA-PEG formulation in healthy rat pups by intravenous tail vein injection. Four hours after administration, only PLGA-PEG/P80 nanoparticles were able to extravasate across the healthy BBB and uptake in neurons and microglia (Figure 5.4). To quantify nanoparticle penetration across the BBB, we used a capillary depletion technique on homogenized brain tissue which separated brain capillaries from the parenchyma [127]. Results are presented as the percent of injected dose (%ID) per gram brain parenchyma or brain capillary (Figure 5.4A). Only PLGA-PEG/P80 nanoparticles achieved a significantly higher concentration in the brain parenchyma compared to brain capillaries (17.8 vs 7.4 %ID per g tissue, p=0.028). However, all nonionic surfactants improved BBB permeation

compared to the no-surfactant control: without a surfactant, nanoparticle concentration in brain capillaries was 14.9-fold higher than in the parenchyma; F68, F127, P80, and PVA reduced this value to 3.2-, 0.9-, 0.4-, and 1.2-fold, respectively. Interestingly, the formulation with anionic CHA demonstrated nearly no accumulation in either the brain capillaries or parenchyma.

We then sought to understand the fate of nanoparticles once within the brain parenchyma. Using confocal imaging, we found evidence of PLGA-PEG/P80 uptake in microglia and neurons within the hippocampus (Figure 5.4B). In contrast, PLGA-PEG nanoparticles formulated without surfactant or with CHA, F68, F127, or PVA showed greater association with blood vessel structures (Figure 5.4C). Staining of tight junction protein zona occludens 1 (ZO-1) confirmed these regions as brain capillaries (Figure 5.5A). The accumulation of nanoparticles at the healthy BBB persists at least for 24 hours: patterns of PLGA-PEG/PVA nanoparticle localization in brain capillaries appear consistent at both 4 hours and 24 hours after administration, with no visible additional neuronal or microglial uptake of nanoparticles (Figure 5.5B-D). Comparison with the PLGA/F127 formulation after 24 hours indicates that the absence of a PEG layer does not enable increased BBB transcytosis or cellular uptake (Figure 5.5C-D). Finally, analysis of nanoparticle biodistribution across serum and major organs supports that a large fraction of nanoparticles are still in circulation at 4h (Figure 5.4D). The liver and spleen also demonstrate nanoparticle accumulation, while more limited uptake was found in the kidney, heart, and lungs.

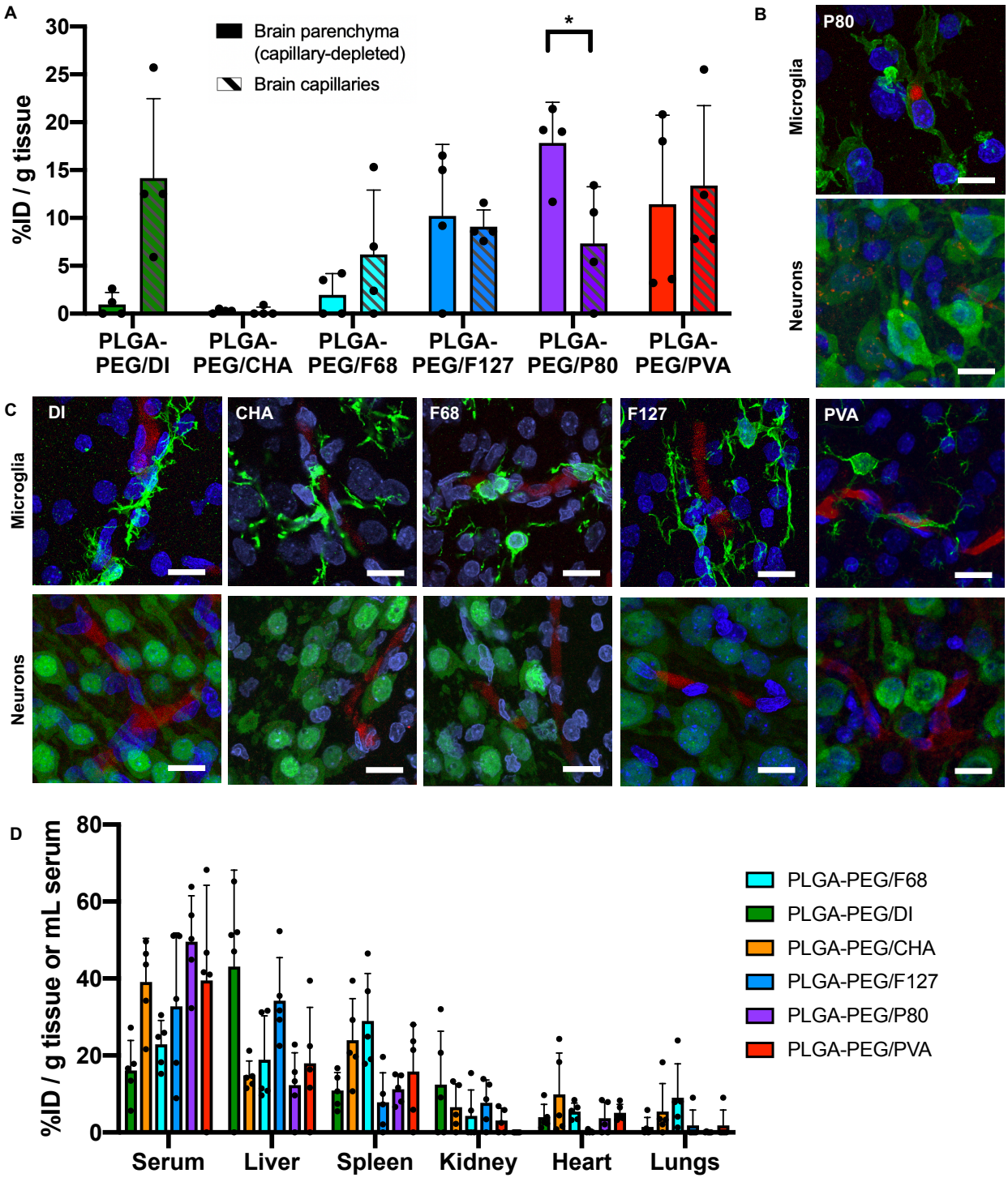

Figure 5.4 Distribution of biodegradable, PEGylated nanoparticles (red) in the brain and major organs at t=4h.

(A) PLGA-PEG/P80 nanoparticles, unlike all other formulations, exhibit significantly higher accumulation (p=0.0280) in the brain parenchyma (left bars, solid fill) compared to brain capillaries (right bars, hashed). (B) PLGA-PEG/P80 nanoparticles can internalize within some microglia (green, top) and neurons (green, bottom) in the brain parenchyma. (C) PLGA-PEG/DI, PLGA-PEG/CHA, PLGA-PEG/F68, PLGA-PEG/F127, and PLGA-PEG/PVA nanoparticles do

not exhibit patterns of microglial (top row) or neuronal (bottom row) uptake, and instead appear associated within the vasculature. (D) Nanoparticles demonstrate accumulation in the serum, liver, and spleen, with minimal signal from the kidney, heart, and lungs. (A, D): Each dot represents one pup for a total of n=4 (brain) or n=5 (major organs). (B-C): All cell nuclei (blue) are stained with DAPI and all scale bars represent 20 μm.

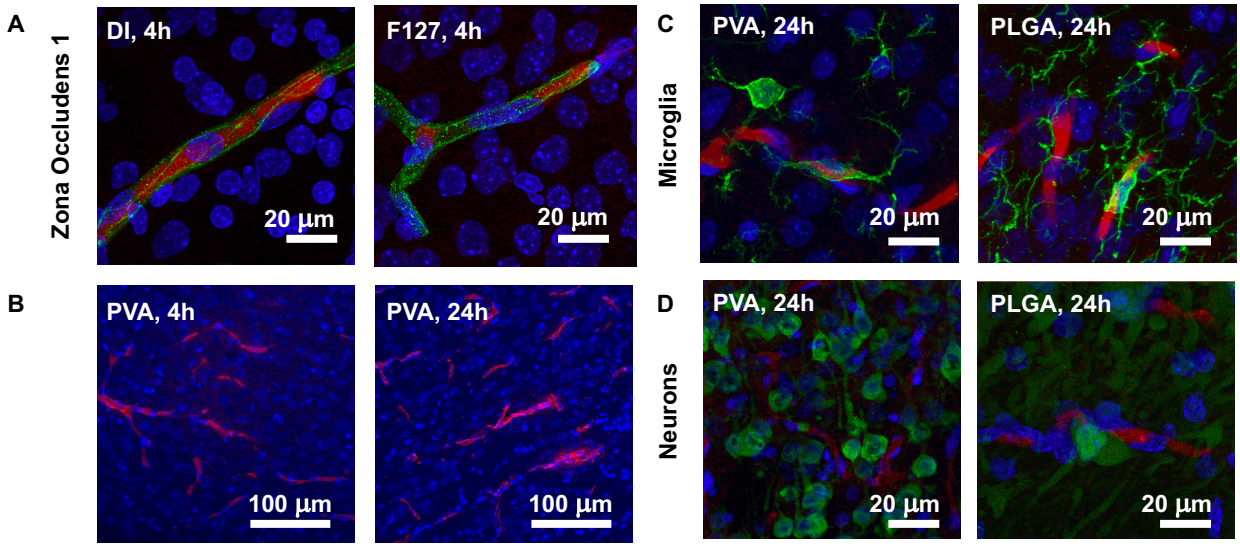

Figure 5.5 Supplementary assessments of in vivo nanoparticle localization at 4h and 24h. (A) Staining of ZO1 (green) confirms nanoparticle localization within blood vessels. (B) PLGA-PEG/PVA nanoparticles appear stuck within blood vessel walls at both 4h and 24h post-administration. (C) No microglial uptake of PLGA-PEG/PVA or PLGA/F127 nanoparticles was observed 24h after administration. (D) No neuronal uptake of PLGA-PEG/PVA or PLGA/F127 nanoparticles was observed 24h after administration.

Polysorbate 80 is surface-associated and influences serum protein adsorption

Surfactants, including P80, may achieve favorable nanoparticle fate in the brain by facilitating plasma protein adsorption or desorption to the nanoparticle surface as the “protein corona” biolayer develops [262]. However, this phenomenon is poorly studied for nanoparticles with both PEG and surfactants. We first used time-of-flight secondary ion mass spectrometry to establish that P80 is present on the nanoparticle surface. Positive and negative ion control spectra were taken from PLGA-PEG/DI nanoparticles and the P80 surfactant to determine unique peaks for each material. These peaks were then used to create a peak ratio A/(A+B) where A = sum of all P80 peaks and B = sum of all nanoparticle peaks. Figures 5.6A and 5.6B show the positive and negative ion peak ratios respectively from the ToF-SIMS data. Table 5.2 shows the proposed chemical identifications of the selected peaks for each material. As seen in Figures 5.6A and 5.6B, the PLGA-PEG/P80 nanoparticles show a higher relative intensity of the P80 peaks relative to the PLGA-PEG/DI nanoparticles ($p=0.001$ and $p<0.0001$ for the positive and negative ion peaks, respectively) confirming the presence of P80.

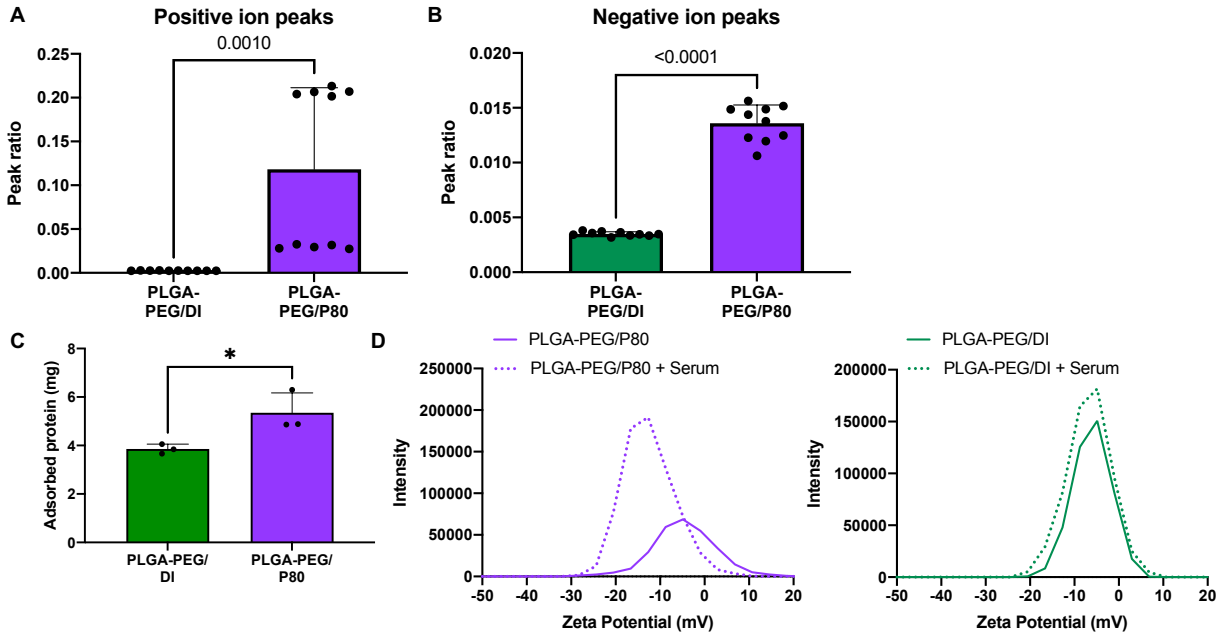

Figure 5.6 PLGA-PEG/P80 surface analysis and serum protein adsorption.
Positive ion (A) and negative ion (B) peak ratio from PLGA-PEG/DI and PLGA-PEG/P80 ToF-SIMS data indicate a statistically significant presence of P80 on the surface of PLGA-PEG/P80 nanoparticles. (C) Compared to the PLGA-PEG/DI control, PLGA-PEG/P80 nanoparticles exhibited increased protein adsorption (p=0.0382). (D) PLGA-PEG/P80 demonstrated a negative shift in ζ-potential after plasma incubation, which was not observed with the PLGA-PEG/DI control.

Table 5.2 Proposed chemical identifications of selected ToF-SIMS peaks from nanoparticle and P80 control samples.

Positive ion peaks: PLGA-PEG/DI		**Positive ion peaks: P80**		**Negative ion peaks: PLGA-PEG/DI**		**Negative ion peaks: P80**	
m/z	**Label**	**m/z**	**Label**	**m/z**	**Label**	**m/z**	**Label**
56.03	C_3H_4O	155.10	$C_9H_{15}O_2$	47.01	CH_3O_2	61.03	$C_2H_5O_2$
87.01	$C_3H_3O_3$	171.14	Unknown	73.00	C_2HO_3	105.06	$C_4H_9O_3$
88.01	$C_3H_4O_3$	197.15	$C_{12}H_{21}O_2$	75.01	$C_2H_3O_3$	127.07	$C_7H_{11}O_2$
100.02	$C_4H_4O_3$	199.13	Unknown	87.01	$C_3H_3O_3$	139.11	$C_9H_{15}O$ possible
101.02	$C_4H_5O_3$	211.16	Unknown	89.03	$C_3H_5O_3$	141.09	$C_8H_{13}O_2$
102.03	$C_4H_6O_3$	213.15	Unknown	103.01	$C_3H_3O_4$	141.13	$C_9H_{17}O$
112.02	Unknown	223.15	$C_{14}H_{23}O_2$ possible	115.00	$C_4H_3O_4$	153.10	$C_9H_{13}O_2$
113.03	$C_5H_5O_3$ possible	225.17	Unknown	116.01	$C_4H_4O_4$	155.11	$C_9H_{15}O_2$
114.04	$C_5H_6O_3$	239.20	$C_{16}H_{31}O_2$ possible	117.02	$C_4H_5O_4$	157.13	$C_9H_{17}O_2$
115.01	$C_4H_3O_4$ possible	281.25	$C_{18}H_{33}O_2$ possible	129.02	$C_5H_5O_4$	169.13	$C_{10}H_{17}O_2$ possible
116.01	Unknown	283.27	$C_{18}H_{35}O_2$ possible	131.00	$C_4H_3O_5$	171.11	$C_9H_{15}O_3$ possible

127.05	Unknown	309.30	$C_{20}H_{37}O_2$ possible	131.03	Unknown or $C_5H_7O_4$	183.14	$C_{11}H_{19}O_2$
128.05	Unknown	323.29	Unknown	133.02	Unknown or $C_4H_5O_5$	185.12	$C_{10}H_{17}O_3$ possible
130.03	$C_5H_6O_4$	339.33	Unknown	143.04	$C_6H_7O_4$ possible	195.14	$C_{12}H_{19}O_2$
131.04	$C_5H_7O_4$			145.02	Unknown or $C_5H_5O_5$	197.16	$C_{12}H_{21}O_2$
158.02	$C_6H_6O_5$ possible			147.04	Unknown or $C_5H_7O_5$	199.18	$C_{12}H_{23}O_2$
159.03	$C_6H_7O_5$ possible			159.04	Unknown or $C_6H_7O_5$ or $C_{10}H_7O_2$	209.16	$C_{13}H_{21}O_2$
172.04	$C_7H_8O_5$ possible			161.05	Unknown or $C_6H_9O_5$ or $C_{10}H_9O_2$	220.16	$C_{14}H_{20}O_2$
173.00	Unknown			175.03	Unknown	223.18	$C_{14}H_{23}O_2$
175.02	Unknown			189.05	Unknown	227.20	$C_{14}H_{27}O_2$
186.05	$C_8H_{10}O_5$ possible					235.23	Unknown
187.02	Unknown					237.25	$C_{16}H_{29}O$ possible
188.03	Unknown					253.22	$C_{16}H_{29}O_2$
189.04	$C_7H_9O_6$ possible					255.24	$C_{16}H_{31}O_2$
199.06	$C_9H_{11}O_5$ possible					263.25	Unknown
200.07	Unknown					265.27	$C_{15}H_{37}O_3$ possible
201.04	Unknown					269.26	$C_{17}H_{33}O_2$
203.05	Unknown					281.25	$C_{18}H_{33}O_2$
216.03	$C_8H_8O_7$ possible					297.27	$C_{19}H_{37}O_2$ possible
230.04	$C_9H_{10}O_7$ possible						
233.03	Unknown						
243.05	$C_{10}H_7O_7$ possible						
244.05	Unknown						
245.03	Unknown						
247.04	Unknown						
257.07	$C_{11}H_{13}O_7$ possible						
258.07	Unknown						
259.05	Unknown						
273.06	Unknown						
274.03	Unknown						
275.05	Unknown						
288.04	Unknown						

316.07	Unknown
330.07	Unknown

We next incubated PLGA-PEG/DI and PLGA-PEG/P80 nanoparticles in rat plasma for four hours at 37°C and subsequently quantified the amount of plasma proteins adsorbed to the nanoparticles (Figure 5.6C). Our results show significantly increased levels of protein adsorption in the PLGA-PEG/P80 ($p=0.0382$) compared to nanoparticles without surfactant. We further found evidence that elevated serum protein adsorption alters the nanoparticle surface charge: after the serum incubation, a significant negative shift in ζ-potential was observed for PLGA-PEG/P80 nanoparticles (-3.6 to -11.2 mV, $p=0.0002$) but not for PLGA-PEG/DI nanoparticles (Figure 5.6D). This shift was not associated with a change in nanoparticle stability or polydispersity (Figure 5.7A) and is larger than the shift experienced by any other surfactant-formulated nanoparticle (Figure 5.7B).

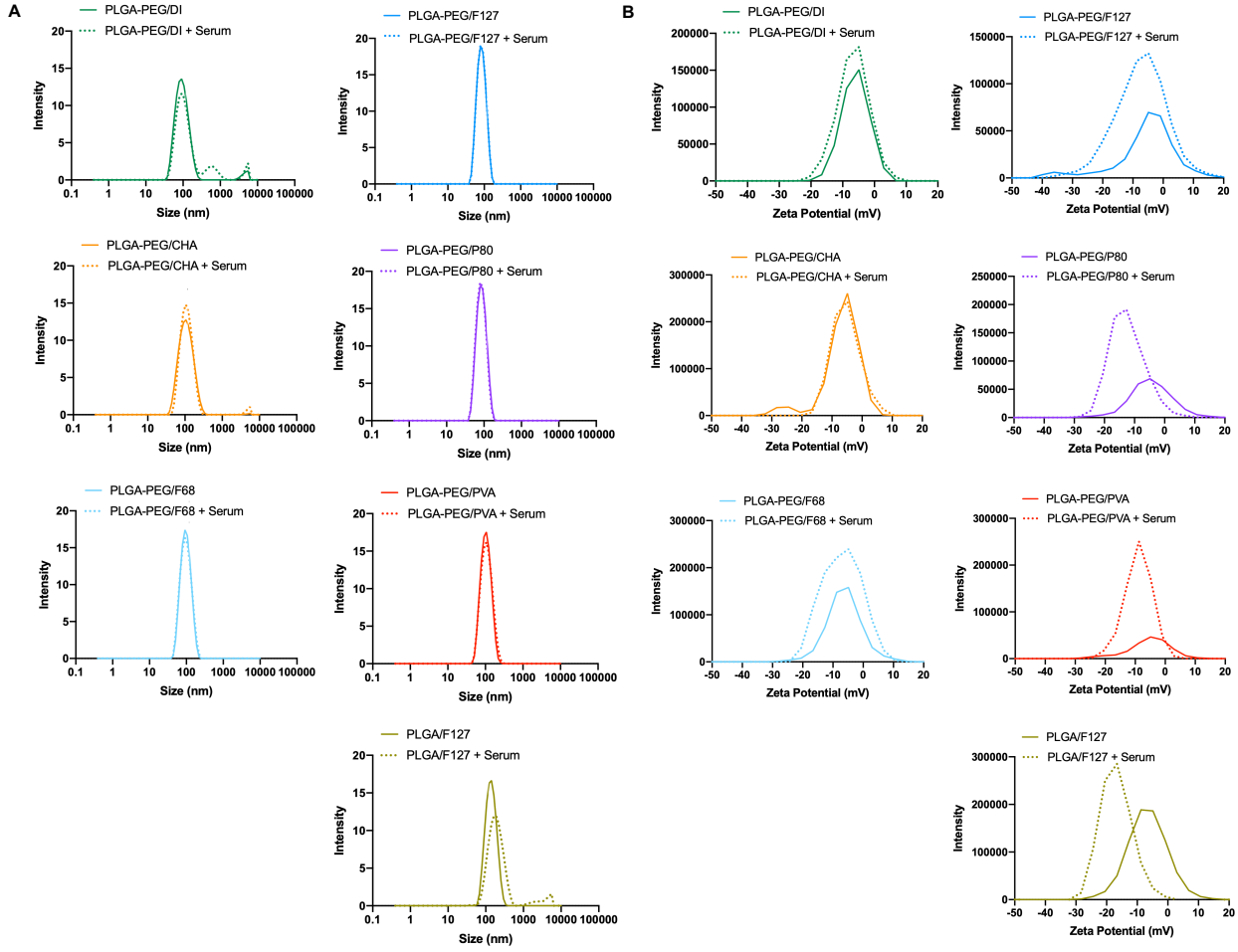

Figure 5.7 Supplementary analysis: size and surface charge characterization for all nanoparticle formulations after 4-hour incubation in plasma.

(A) All formulations except PLGA-PEG/DI and PLGA/F127 maintain stability and low polydispersity after plasma incubation. (B) PLGA-PEG/P80 and PLGA/F127 show the largest negative shifts in surface charge after plasma incubation.

5.3 Discussion

In this study, we have evaluated the influence of surfactant on nanoparticle biodistribution, transport within the brain, and cellular fate. The results suggest that surfactant molecules increase interactions between nanoparticles and the brain microenvironment. This was demonstrated by improved BBB penetration, decreased diffusive ability through the brain ECS, and increased uptake within neurons and microglia for formulations with surfactant compared to a non-surfactant control. Importantly, surfactants were able to alter nanoparticle behavior solely after incorporation into the formulation process, without any additional incubation steps for surface coating or adsorption performed in previous studies. This suggests that complete surface coverage is not necessary to achieve surfactant-mediated interactions with components of the brain microenvironment.

One important surfactant-mediated interaction confirmed in this study was that between P80 and cells of the BBB. PLGA-PEG/P80 nanoparticles, unlike the other formulations administered *in vivo*, extravasated beyond brain capillary cells and localized within neurons and microglia in the healthy brain. Previous studies support the ability of a P80 surface coating to enhance nanoparticle accumulation in the brain [263-265]. The mechanism of this enhanced transport has been attributed to receptor-mediated transcytosis: P80 promotes the adsorption of apolipoprotein B and E, which in turn bind to low-density lipoprotein receptors on brain endothelial cells [253]. A similar phenomenon has been described with F68-coated PLGA formulations [75], and several previous studies have concluded that both F68- and P80-coated PLGA nanoparticles enhance drug penetration in the brain [155, 266]. In comparison to these studies, which used fluorescence imaging to qualitatively show BBB penetration, our study used capillary depletion to quantify fluorescence signal in capillary-rich and capillary-depleted brain fractions. This method is robust for bright fluorophores like AlexaFluor but is sensitive to *in vivo* processing parameters including perfusion quality, similar to other methods for determining BBB permeability [267]. Our results suggest that surfactant-mediated BBB penetration can still occur with low surfactant amounts (i.e. without specific coating steps) and despite nanoparticle PEGylation. Additionally, the subsequent cellular internalization of PLGA and PLGA-PEG nanoparticles had not previously been characterized, despite the importance of intracellular drug delivery for many neurological disease targets. Thus, the ability of PLGA-PEG/P80 nanoparticles to localize within neurons and microglia in this study is notable. This result aligns

with one previous study demonstrating neuronal uptake of P80-coated human serum albumin nanoparticles [268] and motivates further investigation of the mechanism driving nanoparticle fate beyond BBB penetration. The influence of brain region on nanoparticle fate may also be important for future studies, since it is well known that brain regions differ in degree of vascularization [269] and cellular composition [270].

Enhanced brain accumulation of PEGylated nanoparticles formulated with nonionic surfactants is likely influenced by surfactants at the nano-biointerface, particularly with the formation of a protein corona. We demonstrate that, even on well-PEGylated nanoparticles, surfactant choice influences the extent of plasma protein adsorption. Based on previous studies evaluating the protein corona of biodegradable, polymeric nanoparticles, the major adsorbed proteins are likely albumin, fibrinogen, immunoglobulin G and its light chains, and the apolipoproteins ApoA-I and ApoE [157]. However, the exact composition of the protein corona likely differs between our different surfactant formulations and is known to change upon transport across the BBB [262]. Our results suggest that differences in the *in vivo* fate of biodegradable nanoparticles reflect differences in the protein corona, given that formulations with enhanced brain uptake (PLGA-PEG/F127, P80, and PVA) presented higher levels of adsorbed protein compared to those that had low brain uptake (PLGA-PEG/CHA and F68). The in-depth characterization of surfactant effects on nanoparticle protein coronas, especially considering dynamic changes as the nanoparticle transports through various brain compartments, is an important area for future work.

Even at very short scales of length and time, surfactants still impart influence on nanoparticle transport in the brain. From multiple particle tracking analysis, we showed that the presence of nonionic surfactant molecules hinders PLGA-PEG nanoparticle diffusion compared to control nanoparticles without surfactant. The heterogeneous surface produced by the incorporation of nonionic surfactant molecules within a PEG layer may increase viscous drag in the brain extracellular space, slowing diffusive behavior. In contrast, the inclusion of an anionic surfactant like CHA increased diffusive behavior. We speculate that the small size of CHA likely minimizes interference with surface PEG chains, allowing more efficient PEG coverage and greater inert behavior of the nanoparticle. Additionally, individual CHA molecules may contribute to enhanced diffusion due to electrostatic repulsion effects with negatively charged extracellular matrix (ECM) proteins [271]. These results are further evidence that surfactant molecules increase interactions between the nanoparticle and its biological environment, which aligns with a previous study on the hindrance effect of PVA on nanoparticle diffusion through cervico-vaginal mucus [257]. Every formulation with surfactant, even the highly diffusive PLGA-

PEG/CHA nanoparticles, exhibited more constrained trajectory features compared to the PEGylated formulation without surfactant. Based on the extracted geometric features, surfactant-mediated hindered transport specifically results in reduced diffusive efficiency and decreased random sampling of the brain microenvironment, which limit the nanoparticle's ability to traverse the brain parenchyma after BBB extravasation. The features also suggest a mechanism of hindered diffusion: subdiffusive and trapped classifications are associated with nanoparticles which have been compartmentalized within cells. Although trajectories were too short to capture complete endocytosis, our results suggest that formulations with surfactant molecules have an increased likelihood of localizing within cellular compartments compared to formulations without surfactant.

In alignment with previous studies across animal species, nanoparticles without a PEG layer are immobilized in brain tissue. Not only was the average diffusive ability of a PLGA nanoparticle more than 7-fold slower than its PEGylated counterpart, but extracted trajectory features also described nanoparticles which were more subdiffusive, constrained, trapped, and less efficient than any other formulation. Only one previous study has reported these trajectory features for nanoparticles diffusing within a biological environment; gold nanoparticles exhibited both super- and sub-diffusion within fibroblasts *in vitro* [119]. As quantifying and classifying nanoparticle diffusion becomes more widespread in the drug delivery literature, it will be important to create further distinctions between specific nanoparticle transport modes, such as superdiffusion by an ATP-driven transport process versus intracellular flow gradients. It is also important to maintain biological complexity when tracking diffusion: our *ex vivo* platform maintains the brain ECM, which can itself confine or trap nanoparticles [83]. While the PEG layer minimizes nanoparticle interactions with ECM proteins, the PLGA formulation was likely significantly hindered by them. Incorporation of a Pluronic® surfactant, F127, into the PLGA nanoparticle formulation process did not result in diffusive behavior comparable to PLGA-PEG nanoparticles. This result highlights the importance of PEGylation in the development of nanotherapeutics for the brain. Compared to the ECS of other organs, the brain ECS is more tortuous and has more narrow pores, increasing the relative importance of an inert surface coating [272, 273]. Our results suggest that the incorporation of surfactants into PLGA-PEG formulations results in nanoparticles that balance diffusive ability and cellular interaction.

Following successful penetration of the BBB and diffusion through the ECS, nanoparticle fate in the brain is dependent on its ability to internalize within target brain cells. We observed surfactant-mediated nanoparticle interactions with neurons and microglia in an *ex vivo* environment. Neuronal- or microglial-specific delivery of nanotherapeutics enables drugs to

bypass transporters which may be involved in pathological processes [188], and instead provide direct intracellular therapeutic effects with limited extracellular consequences. Based on qualitative imaging, we found that all formulations can achieve both neuronal and microglial uptake when applied topically to cultured brain slices. Neurons and microglia utilize different transport pathways for nanoparticle internalization: neuronal uptake largely occurs through clathrin-mediated endocytosis [274], but microglia can additionally leverage phagocytosis and macropinocytosis pathways associated with macrophage cells [230]. While the effect of PEGylation on decreasing phagocytic uptake is well-known, studies on the effect of surfactant have only involved non-PEGylated formulations [155, 265, 266]. In those experiments, hydrophilic poly(ethylene oxide) (PEO) segments of surfactant molecules mimicked a PEG layer to reduce protein adhesion and nonspecific cellular uptake [275]. Our results show that, when present together, surfactants act cooperatively with PEG to further reduce phagocytic uptake. This finding lays in contrast to conclusions from the diffusion experiments, where surfactants acted antagonistically with the PEG layer to increase cell interactions and slow diffusive transport. We hypothesize that time scale can determine how surfactants and PEG will interact with each other: surfactant disruptions to the PEG layer may be significant at the short time scales relevant to diffusion; at longer scales relevant to cell uptake, surfactants may enhance PEG's nanoparticle shielding ability.

One limitation of this study was the inability to characterize the amount or distribution of surfactant at the nanoparticle surface. While mass spectrometry determined that surfactant contributions to the PLGA-PEG/CHA and PLGA-PEG/P80 were small (less than 0.01% by weight), it could not be used for larger, polymeric surfactants and did not provide any information on the spatial distribution of these molecules. ToF-SIMS determined that P80 surfactant molecules were present at the nanoparticle surface but could not quantify the extent of surface coverage or distribution throughout the nanoparticle. Determination of these additional parameters would provide additional insight to the minimum effective dose of surfactant required to achieve biological effects. However, these measurements have not previously been done for biodegradable polymeric nanoparticles and are challenging due to chemical similarities between surfactant molecules and the PLGA-PEG polymer itself. Development of this technique would enable the formulation of nanoparticles with varying degrees of surface presentation of surfactant, which is likely a key determinant of nanoparticle behavior in the brain. Additionally, the exact role of surfactant length and hydrophobicity may be elucidated by focusing investigations to certain classes of surfactants, like the Pluronics® or Tweens. Such effects have been preliminarily identified for example on *in vitro* macrophage

uptake [276], but characterization in the unique brain microenvironment is currently lacking. The continued study of the biological roles of surfactant molecules can inform the design of nanoparticles for effective transport into and within the brain.

5.4 Conclusion

We have shown that the incorporation of surfactant molecules in PLGA-PEG formulations enhances nanoparticle interaction within the brain microenvironment. Nonionic surfactants mediate enhanced BBB penetration after intravenous administration: PLGA-PEG/F68, PLGA-PEG/F127, PLGA-PEG/PVA, and PLGA-PEG/P80 nanoparticles exhibit 2- 11-, 12-, and 19-fold greater uptake in the brain parenchyma, respectively, compared to PLGA-PEG nanoparticles without surfactant. We observed decreased microglial uptake *ex vivo* and hindered diffusive transport of nanoparticles containing surfactants, demonstrating the role of surfactants in increasing short-term interactions with cells while reducing longer-term uptake processes. Charged surfactants, such as the anionic CHA, enable faster overall nanoparticle diffusion likely due to electrostatic interactions with brain ECM components. Overall, the presence of a surfactant influences the ability of nanoparticles to overcome biological barriers in the brain. Additional studies on key nanoparticle design parameters, including surfactant spatial distribution and surface coverage for effective delivery to the brain, will enable future development, implementation, and clinical translation for polymer nanoparticles in treating neurological disorders.

In the next chapter, we use the brain-penetrating PLGA-PEG/P80 platform to deliver a therapeutic enzyme, catalase, to the injured neonatal brain. Catalase, as a large hydrophilic protein, presents distinct nanoparticle loading challenges from the small, hydrophobic curcumin molecule presented in Chapter 3. Successful encapsulation of both drugs in the PLGA-PEG/P80 platform would demonstrate its broad therapeutic potential for neurological applications.

Chapter 6 – Catalase-loaded nanoparticles for neuroprotection against neonatal brain injury

Look deep into nature, and then you will understand everything better.
– Albert Einstein

A couple years ago, Chris came to me with the idea behind this project: could hydrophobic ion-pairing improve enzyme loading in our nanoparticles? He could use computational simulations to "look deep" into the molecular interactions between enzymes, polymers, and solvents, while I would test the hypothesis experimentally. After some initial success, this project quickly grew to be a huge collaborative effort—bringing in the Neonatology team—and an incredibly enjoyable way to conclude my thesis.

Note: molecular simulations for this project, performed by Chris and Jim, will be included in the submitted manuscript but are not presented in this thesis chapter.

6.1 Introduction

Neonatal HIE is a devastating neurological condition that affects 1.3-4.7 in 1000 live births in the United States [3, 277]. The current standard-of-care, TH, is only clinically implemented in cases of moderate or severe HIE and still leaves more than 30% of infants dead or with severe disability [278]. One strategy to improve neonatal outcomes is to use a pharmaceutical agent as an adjuvant to TH. For example, erythropoeitin (Epo) is a promising therapeutic which was successfully translated from the Vannucci model of HIE in rats to non-human primates and is now in clinical trials [70, 279]. Another promising therapeutic may be catalase, an antioxidant enzyme which converts hydrogen peroxide to water and molecular oxygen. By ameliorating hypoxia and reducing oxidative stress, catalase has demonstrated efficacy against a range of pathologies including solid tumors [280, 281], inflammatory bowel disease [282], and vascular oxidative stress [283]. For neurological applications, catalase can attenuate neuroinflammatory and apoptotic pathways *in vitro* [284, 285], but its application *in vivo* has been limited due to its short half-life, proteolytic degradation, immunogenicity, and inability to penetrate the brain [286, 287].

Nanoparticles serve as vehicles that can improve drug biodistribution and bioavailability. Drug-loaded biodegradable nanoparticles composed of PLGA-PEG have been shown to improve drug solubility, stability, circulation time, release kinetics, and transport to and within the brain parenchyma [73, 288]. Enzymes can particularly benefit from nanoparticle encapsulation as the polymer matrix provides protection from immune clearance and systemic degradation [289]. However, the hydrophilic nature of enzymes limits their encapsulation into the hydrophobic core of PLGA-PEG nanoparticles. Hydrophobic ion-pairing (HIP) is a recent technique developed to increase the lipophilicity of peptides and proteins [290, 291]. In this

technique, complexes are formed by electrostatic interactions between ionizable groups on the protein and ion-pairing agent. Complexes are reversible and can dissociate in ionic solutions, but they are also lipophilic due to hydrophobic groups on the ion-pairing agent [292]. HIP has previously been used for PLGA nanoparticle encapsulation of small peptides, antibodies, and proteins as large as bovine serum albumin (BSA, 60 kDa) [292-295]. Complexation of large enzymes such as catalase (240 kDa), and subsequent nanoparticle formulation and evaluation, has not yet been reported.

In this study, we determine the effects of ion-pairing agent, molar ratio, pH, and buffer ion on catalase HIP complexation efficiency. Using an optimized catalase complex, we next develop a PLGA-PEG nanoparticle formulation which provides high catalase activity and protection in degradative conditions. Finally, we assess the efficacy of the catalase-loaded PLGA-PEG nanoparticles in the Vannucci model of HIE in neonatal rats.

6.2 Results

Effect of ion-pairing agent, molar ratio, pH, and buffer ion on complexation efficiency

We first optimized the HIP complexation of catalase by investigating three common sulfated ion-pairing agents, taurocholic acid (TA), sodium dodecyl sulfate (SDS), and dextran sulfate (DS), across a range of molar ratios. Phosphate buffer at pH 4.7 was used for all initial experiments. For each ion-pairing agent, catalase binding efficiency increased with increasing molar ratio. Catalase incubation with TA at ion-to-protein molar ratios of 32, 64, 128, and 256 resulted in 8.6, 16, 20, and 31% binding efficiencies, respectively (Figure 6.1A). For SDS, molar ratios 16, 32, 64, and 128 led to 27, 30, 31, and 40% binding efficiencies (Figure 6.1B), and molar ratios of dextran sulfate (DS) at 0.5, 1, 2, 5, and 10 led to 32, 36, 41, 42, and 50% binding efficiencies (Figure 6.1C).

To further optimize complexation, we investigated the role of pH on catalase binding efficiency using DS as the ion-pairing agent. Lower pHs led to greater binding efficiency: at pH 4.2, 4.7, 5.2, and 7.0, we observed binding efficiencies of 48, 42, 35, and 10%, respectively (Figure 6.1D). However, lower pH was also associated with higher catalase degradation, as measured by a loss of activity. When normalized to catalase activity in phosphate buffer at pH 7, catalase at pH 4.2, 4.7, and 5.2 retained 65, 87, and 90% of its activity, respectively (Figure 6.1E).

At acidic pHs, phosphate has a reduced buffering capacity. We therefore investigated DS-catalase complexation with citrate buffer, which has a working range of pH 3.0-6.2. At ion-to-protein molar ratios of 0.5, 1, 2, 5, and 10, we observed binding efficiencies of 19, 55, 62, 67,

and 68%, respectively (Figure 6.1F). In comparison to phosphate buffer, citrate buffer achieved significantly higher binding efficiencies at every molar ratio above 0.5 ($p<0.05$ for all).

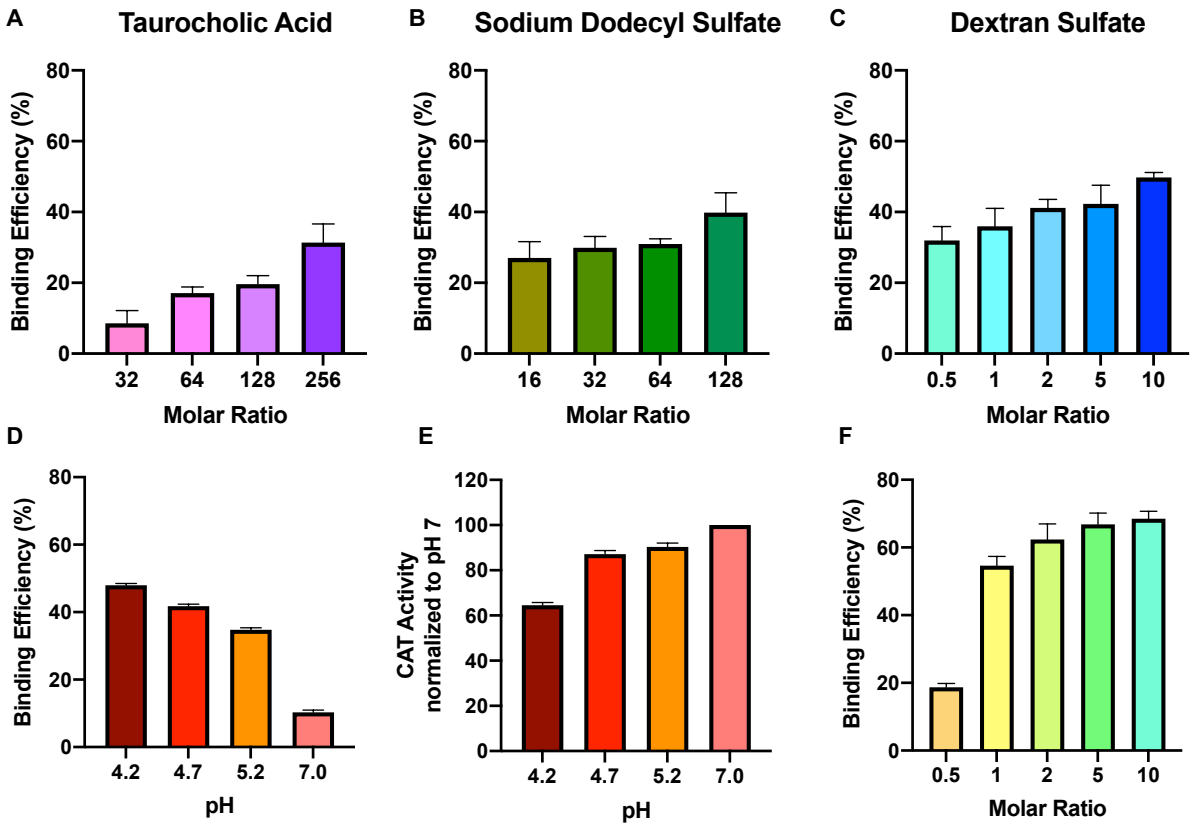

Figure 6.1 Effect of molar ratio on catalase complexation efficiency with different ion-pairing agents.
(A) TA, (B) SDS, and (C) DS demonstrated an increasing trend of catalase binding efficiency with respect to increasing molar ratio. For DS-CAT complexes, more acidic pHs are associated with (D) increased binding efficiency but (E) increased loss of activity. (F) Binding efficiency in citrate buffer increases with increasing molar ratio. Values are represented as mean ± SD (n=3).

Effect of nanoparticle formulation method on catalase loading and protection

We next incorporated DS-catalase complexes into PLGA-PEG nanoparticles using previously published methods for nanoprecipitation and solid/oil/water (S/O/W) emulsion [293, 295]. Dynamic light scattering results are summarized in Table 6.1. By nanoprecipitation, catalase-loaded nanoparticles had an average diameter of 115.8 nm, PDI of 0.17, and ζ-potential of -2.3 mV. By emulsion, catalase-loaded nanoparticles had an average diameter of 125.4 nm, PDI of 0.25, and ζ-potential of -5.6 mV. Table 6.1 also includes size and surface charge characterization of a blank formulation, used as a control for in vivo studies described in the following section. For these nanoparticles, DS was complexed with BSA at a molar ratio of 5 and pH 3.8.

Table 6.1 Characterization of nanoparticles loaded with HIP complexes.
Nanoparticles were characterized in terms of hydrodynamic diameter, mean ζ-potential, and the PDI by dynamic light scattering at 25°C and pH 7.2 in 10 mM NaCl. All values are reported as mean ± standard error of the mean (SEM) (n=3).

Protein	Formulation method	Number Mean ± SEM (nm)	PDI	ζ-potential ± SEM (mV)
Catalase	Nanoprecipitation	115.8 ± 1.9	0.17	-2.3 ± 0.2
Catalase	S/O/W emulsion	125.4 ± 5.2	0.25	-5.6 ± 0.4
Bovine serum albumin	Nanoprecipitation	106.5 ± 5.4	0.13	-2.6 ± 0.1

To compare the two catalase nanoparticle formulations, we assessed catalase loading by activity and mass. In terms of catalase activity, both formulations achieved similar loading: nanoprecipitation particles had 383 active units (AU) of catalase per mL nanoparticles, while emulsion particles had 393 AU/mL (Figure 6.2A). In terms of catalase loading by mass, however, nanoprecipitation particles (76 µg/mL) had significantly less catalase than emulsion particles (298 µg/mL, p=0.0003) (Figure 6.2B). Together, these two results indicate higher catalase deactivation by the emulsion process. Catalase activity after nanoprecipitation averages around 5,000 AU/mg (as supplied by Sigma); emulsion results in catalase activity of 1320 AU/mg. The emulsion process therefore corresponds to 74% deactivation of catalase.

Next, we assessed nanoparticle protection of catalase in biological media. To mimic degradative serum conditions in vivo, we incubated nanoparticles in a 0.2% pronase solution and measured catalase activity at 0, 1, 2,4, and 24h. Activity was normalized to the 0h timepoint. No significant differences were observed between formulations at each timepoint, and 20% of initial catalase activity is retained by both formulations through the 24h experimental window (Figure 6.2C).

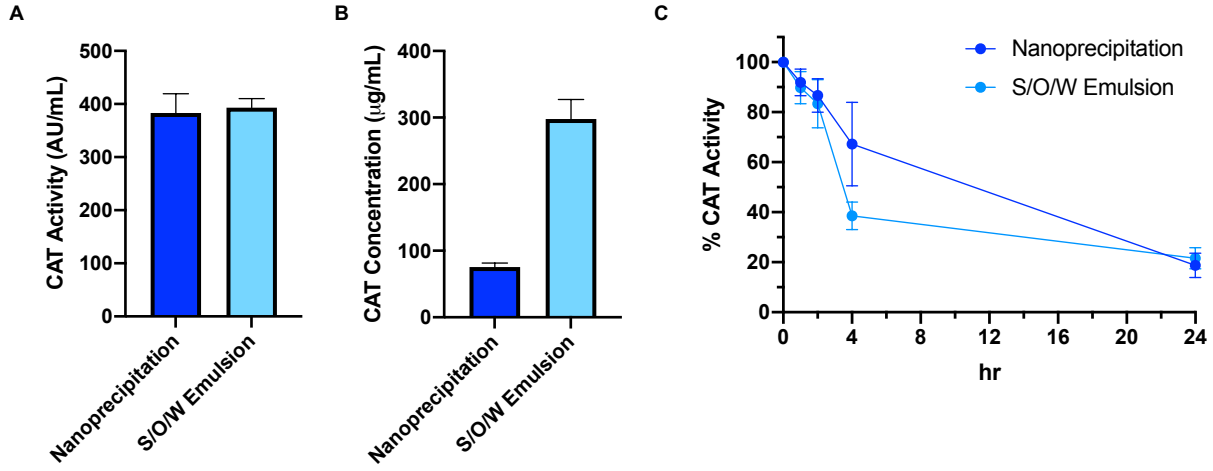

Figure 6.2 Catalase loading and protection in PLGA-PEG nanoparticles by formulation method.
(A) Nanoprecipitation and emulsion nanoparticles achieve non-significantly different catalase loading by activity, but (B) nanoprecipitation nanoparticles have significantly lower catalase

loading by mass (p=0.0003). (C) Both methods result in retention of catalase activity over 24h in 0.2% pronase solution. Values are represented as mean ± SD (n=4 for A and B; n=3 for C).

Effect of catalase-loaded nanoparticles on brain injury severity in neonatal rats

We assessed the efficacy of catalase-loaded nanoparticles in the Vannucci model of HIE with P10 rat pups. Treatments of saline, blank nanoparticles (3300 AU BSA/kg), or catalase nanoparticles (3300 AU catalase/kg) were administered intraperitoneally 30 min, 24h, and 48h after injury. At the 72h endpoint, we found a significant reduction in gross injury scores after catalase-loaded nanoparticle treatment (median score 0, 95% CI 0-2) compared to saline treatment (median score 0.5, 95% CI 0-3, p=0.0392) (Figure 6.3A). Treatment with blank nanoparticles (median score 2, 95% CI 0-3.5) did not have a significant effect on gross injury. Total area loss measurements supported these results (Figure 6.3B). The median (and 95% CI) injury after saline treatment was 13% (10-31%), which was significantly reduced in catalase nanoparticle-treated pups to 4.9% (0.61-27%) but was not significantly affected by treatment with blank nanoparticles (median 23%, 95% CI 16-41%). Representative gross injury and area loss images from the median pup in each group are shown in Figure 6.3C.

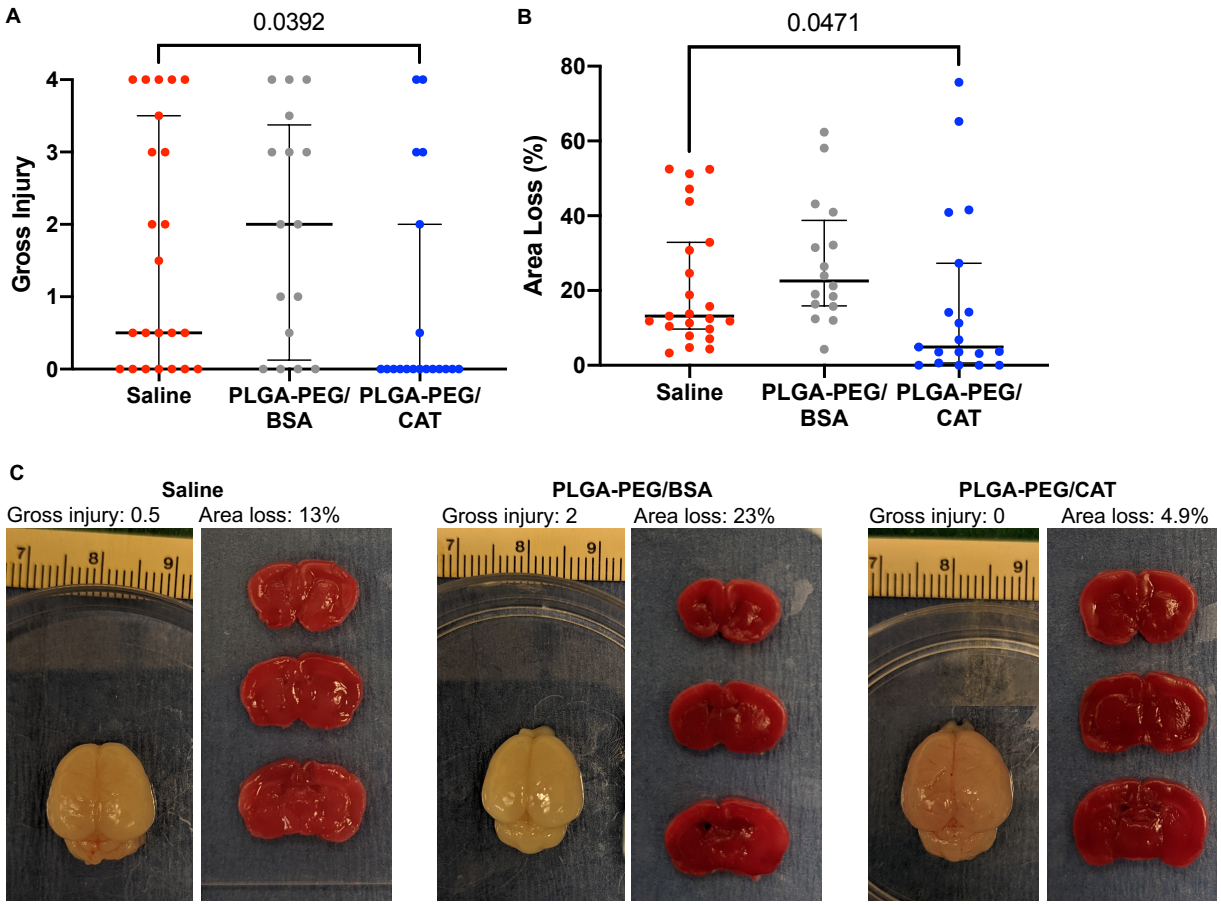

Figure 6.3 Global brain injury is significantly reduced by treatment with catalase-loaded nanoparticles.
(A) Median (95% CI) gross injury scores in the saline, PLGA-PEG/BSA, and PLGA-PEG/catalase (CAT) nanoparticle groups are 0.5 (0-3), 2 (0-3.5), and 0 (0-2). (B) Median (95% CI) area loss measurements in the saline, blank nanoparticle, and catalase nanoparticle groups are 13% (10-31%), 23% (16-41%), and 4.9% (0.61-27%). For both assessments, treatment with catalase is significantly neuroprotective compared to saline ($p=0.0392$ and $p=0.0471$) while blank nanoparticles have no significant effect. (C) Representative gross injury and area loss images from each group.

6.3 Discussion

In this study, we used hydrophobic ion pairing to increase the lipophilicity of catalase, promoting its encapsulation in PLGA-PEG nanoparticles for therapeutic application. We first optimized catalase binding efficiency across ion-pairing agents, molar ratios, pH, and buffer ion. For all variations, catalase complexed quickly with TA, SDS, and DS; the solution immediately turned cloudy with insoluble precipitates. This is in good agreement with previous studies investigating these ion-pairing agents with a number of proteins including lysozyme, conalbumin, insulin, and ovalbumin [296-298]. Catalase, however, is the largest by far among these enzymes. Its large molecular weight may explain the lower binding efficiencies observed in our study (<50% in phosphate buffer, <70% in citrate buffer) compared to previous work (>90%) [293, 295]. Hydrophobic and ionic interactions may be sterically limited in a large tetramer like catalase with complex tertiary and quaternary structure [292, 299]. Despite this, we still observed successful complexation, encouraging further study of HIP with large enzymes.

HIP complexation is driven by electrostatic interactions. At pH 4.7, catalase (pI 5.4) is positively charged while the ion-pairing agents are negatively charged due to their sulfate groups (pKa<2). The ion-to-protein charge ratio was approximately 1:1 for experimental trials TA 128, SDS 128, and DS 5, where binding efficiency was 20, 31, and 42% respectively. Lower binding efficiency with TA and SDS may be attributable to their higher hydrophobicity and lower charge density compared to DS [293]. At pH 4.2, catalase becomes further positively charged and we observed higher binding efficiency with DS 5 (48%). The cost is a loss of catalase function, in alignment with previous work describing deactivation of catalase below pH 4 [300]. In contrast, when catalase is more neutrally charged and fully active at pH 7, hydrophobic interaction-driven binding resulted in only 10% efficiency. Our study also highlights the importance of buffer stability at acidic pHs; using citrate buffer (stable between pH 3.2-6.0), we observed significantly higher binding efficiencies at most DS molar ratios compared to phosphate buffer. Additionally, we could not produce BSA-DS complexes in phosphate buffer at molar ratios and pHs which easily formed complexes in citrate buffer. Although phosphate buffer

has been previously studied in HIP complexation [295], our study supports the use of citrate buffer for complexation with large proteins.

We found improved binding efficiency by increasing the molar ratio for each ion-pairing agent. Previous reports have found a limit to this behavior, where further molar ratio increments past a critical point result in decreased binding [293, 295]. The proposed mechanism is that excess ion-pairing agents form micelles which provide a hydrophobic environment in which complexes can be solubilized or dissociate [301]. A large molecular-weight protein like catalase may require higher molar ratios to exhibit this behavior, or the large protein may interfere with micellization completely. Further work must be done to fully understand the limits of molar ratio to increase catalase binding efficiency. Other parameters, including increased incubation time [293] or larger molecular weight ion-pairing agents [302], may also be worth investigating for improved catalase binding efficiency.

The water-insoluble catalase complexes were then used to improve enzyme loading in PLGA-PEG nanoparticles. Nanoparticle loading of HIP complexes has been previously demonstrated [302], although never with complexes of large enzymes. The conventional method for nanoparticle enzyme encapsulation, water in oil in water (W/O/W) double emulsion, depends on protein partitioning into an organic polymer matrix during a first emulsion. However, hydrophilic protein molecules rapidly penetrate to the external aqueous phase during the second emulsion, leading to poor encapsulation [292, 303]. Additionally, high-energy sonication with PEG and DCM may result in byproducts which exacerbate oxidative stress in models of neurological injury [304]. In contrast, the nanoprecipitation technique involves low-energy mixing of organic and aqueous phases, but results in poor catalase encapsulation as evidenced by rapid loss of catalase activity in degradative conditions [304]. We hypothesized that hydrophobic catalase-DS complexes would demonstrate improved partitioning with PLGA-PEG and improved catalase protection in degradative conditions. Our results supported this hypothesis. Both S/O/W and nanoprecipitation particles retained 20% of their initial catalase activity over 24h in a pronase solution. In a previous study, catalase-loaded W/O/W and nanoprecipitation nanoparticles only retained 6.1% and 5.4% activity, respectively, over 24h [304]. We also showed a pronounced protein deactivation effect with the emulsion method: while both S/O/W and nanoprecipitation particles had similar activity (400 AU/mL), emulsion particles loaded approximately 4-fold higher catalase mass. We therefore proceeded to *in vivo* evaluation with catalase-DS loaded nanoparticles formulated by nanoprecipitation.

In the P10 Vannucci rat model of neonatal HIE, we observed a robust neuroprotective effect in the catalase-loaded nanoparticle treatment group compared to the saline control group.

No neuroprotective effect was observed in the nanoparticle control group using BSA-DS complexes. Catalase scavenging of hydrogen peroxide may combat HIE progression in multiple ways: it alleviates ROS burden in the injured brain [305], serves as an alternate source of oxygen in hypoxic tissue [306], and can mitigate long-term inflammatory processes [307]. Nanoparticle delivery of catalase has previously proved efficacious after MCAO and traumatic brain injury in adult mice [306, 307] and thromboembolic stroke in adult rats [305]. Compared to adults, neonates have relatively immature antioxidant defenses and a reduced ability to regenerate antioxidants under HI conditions [10, 11]. To our knowledge, this study is the first investigation of catalase to provide antioxidant relief after neonatal brain injury. Coadministration of catalase with superoxide dismutase, another antioxidant enzyme which converts oxygen radicals to hydrogen peroxide, may further enhance neuroprotection in this model and is a focus of future work.

One limitation of our *in vivo* study is that overall injury severity is relatively low. Gross injury scores from the saline group show a bimodal injury distribution which is characteristic of this model. However, our median area loss was only 13%, compared to around 25-35% achieved in similar, previous studies [308-311]. Increased animal numbers or longer hypoxia incubation may address this limitation. Increased animal numbers would also enable the assessment of sex-based differences in response to treatment. Significant changes in outcome based on sex have been observed in both preclinical models and in clinical settings [312, 313], and males may potentially display decreased antioxidant defenses compared to females [181, 314]. Our results encourage the further study of catalase-loaded nanoparticles as a pharmaceutical intervention in perinatal brain injury.

6.4 Conclusion

We have shown the successful HIP complexation of catalase with dextran sulfate, which was optimized to achieve 68% binding efficiency using citrate buffer at pH 4.7 at an ion-to-protein ratio of 10. In general, binding efficiency increased with increasing molar ratio and decreasing pH, as expected for a process driven by ionic and hydrophobic molecular interactions. We next demonstrated catalase loading of 76 and 298 μg/mL in PLGA-PEG nanoparticles formulated by nanoprecipitation and emulsion, respectively, although both formulations had similar catalase activity approaching 400 AU/mL. Both formulations also showed similar catalase protection in a degradative environment. Using the nanoparticles formulated by nanoprecipitation, given their lower content of deactivated enzyme, we demonstrated a significant neuroprotective effect in a P10 rat model of neonatal HIE. Further study of catalase as a therapeutic against neonatal brain

injury, and of the PLGA-PEG/P80 nanoparticle platform to enhance therapeutic delivery to the brain, is supported by this work.

In the next chapter, all research completed during this thesis is summarized.

Chapter 7 – Research summary

For the following publications or manuscripts in preparation for submission, the corresponding author is indicated by an asterisk (*) and equal contributions by authors is indicated by a hash symbol (#).

7.1 Determining dominant driving forces affecting controlled protein release from polymeric nanoparticles

Josh Smith[#], Kayla Sprenger[#], Rick Liao, Andrea Joseph, Elizabeth Nance*, and Jim Pfaendtner*. *Biointerphases* (2017) **volume 12**, 02D412.

Enzymes play a critical role in many applications in biology and medicine as potential therapeutics. One specific area of interest is enzyme encapsulation in polymer nanostructures, which have applications in drug delivery and catalysis. A detailed understanding of the mechanisms governing protein/polymer interactions is crucial for optimizing the performance of these complex systems for different applications. Using a combined computational and experimental approach, this study aims to quantify the relative importance of molecular and mesoscale driving forces to protein release from polymeric nanoparticles. Classical molecular dynamics (MD) simulations have been performed on bovine serum albumin (BSA) in aqueous solutions with oligomeric surrogates of poly(lactic-co-glycolic acid) copolymer, poly(styrene)-poly(lactic acid) copolymer, and poly(lactic acid). The simulated strength and location of polymer surrogate binding to the surface of BSA have been compared to experimental BSA release rates from nanoparticles formulated with these same polymers. Results indicate that the self-interaction tendencies of the polymer surrogates and other macroscale properties may play governing roles in protein release. Additional MD simulations of BSA in solution with poly(styrene)-acrylate copolymer reveal the possibility of enhanced control over the enzyme encapsulation process by tuning polymer self-interaction. Last, the authors find consistent protein surface binding preferences across simulations performed with polymer surrogates of varying lengths, demonstrating that protein/polymer interactions can be understood in part by studying the interactions and affinity of proteins with small polymer surrogates in solution.

7.2 Curcumin-loaded polymeric nanoparticles for neuroprotection in neonatal rats with hypoxic-ischemic encephalopathy

Andrea Joseph, Thomas Wood, Chih-Chung Chen, Kylie Corry, Jessica M. Snyder, Sandra E. Juul, Pratik Parikh, Elizabeth Nance*. *Nano Research* (2018) **volume 11**, pages 5670–5688

Hypoxic-ischemic encephalopathy (HIE) is the leading cause of permanent brain injury in term newborns, and currently has no effective cure. Inflammatory processes play a key role in the progression of this disease and may be amenable to a targeted pharmaceutical intervention. Curcumin is a dietary compound with potent anti-inflammatory, antioxidant, and anti-apoptotic properties, but is limited in therapeutic applications due to its low aqueous solubility, low bioavailability, and rapid first-pass hepatic metabolism. To address these limitations, loading curcumin into poly(lactic-co-glycolic acid)-poly(ethylene glycol) (PLGA-PEG) nanoparticles may increase relevant pharmacokinetic parameters and allow for effective drug delivery to the brain. Using the Vannucci model of unilateral hypoxic-ischemic brain injury in neonatal rats, we studied the *in vivo* effect of curcumin-loaded PLGA-PEG nanoparticles on brain uptake, diffusion, and neuroprotection. The curcumin-loaded nanoparticles were able to overcome the impaired blood-brain barrier, diffuse effectively through the brain parenchyma, localize in regions and cells of injury, and deliver a protective effect in these areas. This novel application of curcumin and PLGA-PEG nanoparticle-mediated delivery to a clinically-relevant model of neonatal brain injury provides greater opportunity for clinical translation of targeted therapies for HIE.

7.3 Pharmacokinetics of nanotechnology-based formulations in pediatric populations

Venkata Yellepeddi*, Andrea Joseph, and Elizabeth Nance*. *Advanced Drug Delivery Reviews* (2019) **volume 151**, pages 44-55

The development of therapeutics for pediatric use has advanced in the last few decades. However, off-label use of adult medications in pediatrics remains a significant clinical problem. Furthermore, the development of therapeutics for pediatrics is challenged by the lack of pharmacokinetic (PK) data in the pediatric population. To promote the development of therapeutics for pediatrics, the United States Pediatric Formulation Initiative recommended the investigation of nanotechnology-based delivery systems. Therefore, in this review, we provided comprehensive information on the PK of nanotechnology-based formulations from preclinical and clinical studies in pediatrics. Specifically, we discuss the relationship between formulation parameters of nanoformulations and PK of the encapsulated drug in the context of pediatrics. We review nanoformulations that include dendrimers, liposomes, polymeric long-acting injectables (LAIs), nanocrystals, inorganic nanoparticles, polymeric micelles, and protein nanoparticles. In addition, we describe the importance and need of PK modeling and simulation approaches used in predicting PK of nanoformulations for pediatric applications.

7.4 Nanoparticle-microglial interaction in the ischemic brain is modulated by injury duration and treatment

Andrea Joseph[#], Rick Liao[#], Mengying Zhang, Hawley Helmbrecht[1] Michael McKenna, Jeremy Filteau, and Elizabeth Nance*. *Bioengineering & Translational Medicine* (2020) **volume 5**, e10175

Cerebral ischemia is a major cause of death in both neonates and adults, and currently has no cure. Nanotechnology represents one promising area of therapeutic development for cerebral ischemia due to the ability of nanoparticles to overcome biological barriers in the brain. Ex vivo injury models have emerged as a high-throughput alternative that can recapitulate disease processes and enable nanoscale probing of the brain microenvironment. In this study, we used oxygen-glucose deprivation (OGD) to model ischemic injury and studied nanoparticle interaction with microglia, resident immune cells in the brain that are of increasing interest for therapeutic delivery. By measuring cell death and glutathione production, we evaluated the effect of OGD exposure time and treatment with azithromycin (AZ) on slice health. We found a robust injury response with 0.5 hours of OGD exposure and effective treatment after immediate application of AZ. We observed an OGD-induced shift in microglial morphology towards increased heterogeneity and circularity, and a decrease in microglial number, which was reversed after treatment. OGD enhanced diffusion of polystyrene-poly(ethylene glycol) (PS-PEG) nanoparticles, improving transport and ability to reach target cells. While microglial uptake of dendrimers or quantum dots (QDs) was not enhanced after injury, internalization of PS-PEG was significantly increased. For PS-PEG, azithromycin (AZ) treatment restored microglial uptake to normal control levels. Our results suggest that different nanoparticle platforms should be carefully screened before application and upon doing so, disease-mediated changes in the brain microenvironment can be leveraged by nanoscale drug delivery devices for enhanced cell interaction.

7.5 Governing transport principles for nanotherapeutic application in the brain

Hawley Helmbrecht, Andrea Joseph, Michael McKenna, Mengying Zhang, and Elizabeth Nance*. *Current Opinion in Chemical Engineering* (2020) **volume 30**, pages 112-119

Neurological diseases account for a significant portion of the global disease burden. While research efforts have identified potential drugs or drug targets for neurological diseases, most therapeutic platforms are still ineffective at reaching the target location selectively and with high yield. Restricted transport, including passage across the blood–brain barrier, through the brain parenchyma, and into specific cells, is a major cause of ineffective therapeutic delivery. However, nanotechnology is a promising, tailorable platform for overcoming these transport barriers and improving therapeutic delivery to the brain. We provide a transport-oriented analysis of nanotechnology's ability to navigate these transport barriers in the brain. We also provide an opinion on the need for technology development for increasing our capacity to characterize and quantify nanoparticle passage through each transport barrier. Finally, we highlight the importance of incorporating the effect of disease, metabolic state, and regional dependencies to better understand transport of nanotherapeutics in the brain.

7.6 Surfactants influence polymeric nanoparticle fate within the brain

Andrea Joseph, Georges Motchoffo Simo, Torahito Gao, Norah Alhindi, Dan Graham, Lara Gamble, and Elizabeth Nance*. *In preparation.*

Drug delivery to the brain is limited by poor penetration of pharmaceutical agents across the blood-brain barrier (BBB), within the brain parenchyma, and into specific cells of interest. Nanotechnology can overcome these barriers, but its ability to do so is dependent on nanoparticle physicochemical properties including surface chemistry. Surface chemistry can be determined by a number of factors, including by the presence of stabilizing surfactant molecules introduced during the formulation process. Nanoparticles coated with poloxamer 188 (F68), poloxamer 407 (F127), and polysorbate 80 (P80) have demonstrated uptake in BBB endothelium cells and enhanced accumulation within the brain. However, the impact of surfactants on nanoparticle fate, and specifically on brain extracellular diffusion or intracellular targeting, must be better understood to design nanotherapeutics to efficiently overcome drug delivery barriers in the brain. Here, we evaluated the effect of the surfactants cholic acid (CHA), F68, F127, P80, and poly(vinyl alcohol) (PVA) on poly(lactic-co-glycolic acid)-poly(ethylene glycol) (PLGA-PEG) nanoparticle transport to and within the brain. These surfactants were chosen as they are all biocompatible surfactants commonly used for nanoparticle stabilization. We show that PLGA-PEG/P80 nanoparticles demonstrate enhanced penetration across the BBB and subsequent internalization within neurons and microglia in vivo. The inclusion of surfactant molecules decreases ex vivo microglial uptake and diffusive ability, reflecting the surfactant's role in encouraging cellular interaction at short length scales while reducing nonspecific cellular uptake at longer scales. Thus, surfactants incorporated into the formulation of PLGA-PEG nanoparticles play an important role in determining the nanoparticles' fate within the brain.

7.7 Formulation and efficacy of catalase-loaded nanoparticles for the treatment of neonatal hypoxic-ischemic encephalopathy

Andrea Joseph[#], Chris Nyambura[#], Danny Bondurant, Kylie Corry, Denise Beebout, Olivia White, Olivia Brandon, Lily Farid, Nuo Xu, Ana Rios, Megan Wong, Tommy Wood, Jim Pfaendtner, and Elizabeth Nance*. *Pharmaceutics,* invited submission by May 31, 2021

Neonatal hypoxic-ischemic encephalopathy (HIE) is the most common cause of death and disability in term newborns. Initiation of oxidative stress pathways leads to the buildup of reactive oxygen species and hydrogen peroxide, which may be mitigated by exogenous administration of the antioxidant enzyme catalase. However, the translation of protein therapeutics has been limited due to rapid clearance by serum proteases and circulating macrophages as well as limited passage across the blood-brain barrier. Polymeric nanoparticle encapsulation provides a non-invasive strategy for the controlled delivery of enzymatic cargo but is still limited by poor partitioning of protein into the hydrophobic polymer matrix. In this manuscript, we use the hydrophobic ion-pairing (HIP) method to formulate biodegradable, brain-penetrating nanoparticles loaded with catalase. We optimize HIP complexation across the following variables: three ion-pairing agents: dextran sulfate, sodium dodecyl sulfate, and taurocholic acid; molar ratio; pH; and buffer ion. We use molecular dynamics simulations to probe the molecular driving forces of complexation. Finally, we load catalase complexes in poly(lactic-co-glycolic acid)-poly(ethylene glycol) (PLGA-PEG) nanoparticles and evaluate their efficacy in a neonatal rat model of HIE. Our results support the further investigation of catalase for neuroprotection after neonatal brain injury, and the broad application of HIP for a wide variety of therapeutic enzymes and disease applications.

References

[1] P. Parikh, S.E. Juul, Neuroprotective Strategies in Neonatal Brain Injury, J Pediatr, 192 (2018) 22-32.
[2] C.J. Murray, A.D. Lopez, Global mortality, disability, and the contribution of risk factors: Global Burden of Disease Study, Lancet, 349 (1997) 1436-1442.
[3] J.J. Kurinczuk, M. White-Koning, N. Badawi, Epidemiology of neonatal encephalopathy and hypoxic-ischaemic encephalopathy, Early Hum Dev, 86 (2010) 329-338.
[4] C.M. Robertson, M. Perlman, Follow-up of the term infant after hypoxic-ischemic encephalopathy, Paediatr Child Health, 11 (2006) 278-282.
[5] T. Wood, On the Physiology of Experimental Hypoxic-Ischaemic Brain Injury, Division of Physiology, University of Oslo, 2016.
[6] M.V. Johnston, A. Fatemi, M.A. Wilson, F. Northington, Treatment advances in neonatal neuroprotection and neurointensive care, Lancet Neurol, 10 (2011) 372-382.
[7] K. Blomgren, H. Hagberg, Free radicals, mitochondria, and hypoxia-ischemia in the developing brain, Free Radic Biol Med, 40 (2006) 388-397.
[8] J.S. Beckman, W.H. Koppenol, Nitric oxide, superoxide, and peroxynitrite: the good, the bad, and ugly, Am J Physiol, 271 (1996) C1424-1437.
[9] A.J. Kole, R.P. Annis, M. Deshmukh, Mature neurons: equipped for survival, Cell Death Dis, 4 (2013) e689.
[10] F.F. Gonzalez, D.M. Ferriero, Neuroprotection in the newborn infant, Clin Perinatol, 36 (2009) 859-880, vii.
[11] E.M. Brekke, T.S. Morken, M. Wideroe, A.K. Haberg, A.M. Brubakk, U. Sonnewald, The pentose phosphate pathway and pyruvate carboxylation after neonatal hypoxic-ischemic brain injury, J Cereb Blood Flow Metab, 34 (2014) 724-734.
[12] J.W. McDonald, M.V. Johnston, Physiological and pathophysiological roles of excitatory amino acids during central nervous system development, Brain Res Brain Res Rev, 15 (1990) 41-70.
[13] C.E. Williams, A. Gunn, P.D. Gluckman, Time course of intracellular edema and epileptiform activity following prenatal cerebral ischemia in sheep, Stroke, 22 (1991) 516-521.
[14] M. Thoresen, J. Penrice, A. Lorek, E.B. Cady, M. Wylezinska, V. Kirkbride, C.E. Cooper, G.C. Brown, A.D. Edwards, J.S. Wyatt, et al., Mild hypothermia after severe transient hypoxia-ischemia ameliorates delayed cerebral energy failure in the newborn piglet, Pediatr Res, 37 (1995) 667-670.
[15] A. Bainbridge, I. Tachtsidis, S.D. Faulkner, D. Price, T. Zhu, E. Baer, K.D. Broad, D.L. Thomas, E.B. Cady, N.J. Robertson, X. Golay, Brain mitochondrial oxidative metabolism during and after cerebral hypoxia-ischemia studied by simultaneous phosphorus magnetic-resonance and broadband near-infrared spectroscopy, Neuroimage, 102 Pt 1 (2014) 173-183.
[16] K.J. Hassell, M. Ezzati, D. Alonso-Alconada, D.J. Hausenloy, N.J. Robertson, New horizons for newborn brain protection: enhancing endogenous neuroprotection, Arch Dis Child Fetal Neonatal Ed, 100 (2015) F541-552.
[17] C. Peeters-Scholte, E. van den Tweel, F. Groenendaal, F. van Bel, Redox state of near infrared spectroscopy-measured cytochrome aa(3) correlates with delayed cerebral energy failure following perinatal hypoxia-ischaemia in the newborn pig, Exp Brain Res, 156 (2004) 20-26.
[18] S.N. Reinke, B.H. Walsh, G.B. Boylan, B.D. Sykes, L.C. Kenny, D.M. Murray, D.I. Broadhurst, 1H NMR derived metabolomic profile of neonatal asphyxia in umbilical cord serum: implications for hypoxic ischemic encephalopathy, J Proteome Res, 12 (2013) 4230-4239.
[19] M.H. Faria, L.R. Muniz, P.R. Vasconcelos, Ketone bodies metabolism during ischemic and reperfusion brain injuries following bilateral occlusion of common carotid arteries in rats, Acta Cir Bras, 22 (2007) 125-129.

[20] C.E. Ahearne, N.M. Denihan, B.H. Walsh, S.N. Reinke, L.C. Kenny, G.B. Boylan, D.I. Broadhurst, D.M. Murray, Early Cord Metabolite Index and Outcome in Perinatal Asphyxia and Hypoxic-Ischaemic Encephalopathy, Neonatology, 110 (2016) 296-302.
[21] C.J. Ek, B. D'Angelo, A.A. Baburamani, C. Lehner, A.L. Leverin, P.L. Smith, H. Nilsson, P. Svedin, H. Hagberg, C. Mallard, Brain barrier properties and cerebral blood flow in neonatal mice exposed to cerebral hypoxia-ischemia, J Cereb Blood Flow Metab, 35 (2015) 818-827.
[22] A.J. Gunn, T.R. Gunn, M.I. Gunning, C.E. Williams, P.D. Gluckman, Neuroprotection with prolonged head cooling started before postischemic seizures in fetal sheep, Pediatrics, 102 (1998) 1098-1106.
[23] H. Hagberg, C. Mallard, B. Jacobsson, Role of cytokines in preterm labour and brain injury, BJOG, 112 Suppl 1 (2005) 16-18.
[24] S. Girard, H. Kadhim, M. Roy, K. Lavoie, M.E. Brochu, A. Larouche, G. Sebire, Role of perinatal inflammation in cerebral palsy, Pediatr Neurol, 40 (2009) 168-174.
[25] J.P. O'Callaghan, K. Sriram, D.B. Miller, Defining "neuroinflammation", Ann N Y Acad Sci, 1139 (2008) 318-330.
[26] H. Hagberg, P. Gressens, C. Mallard, Inflammation during fetal and neonatal life: implications for neurologic and neuropsychiatric disease in children and adults, Ann Neurol, 71 (2012) 444-457.
[27] D.L. Vargas, C. Nascimbene, C. Krishnan, A.W. Zimmerman, C.A. Pardo, Neuroglial activation and neuroinflammation in the brain of patients with autism, Ann Neurol, 57 (2005) 67-81.
[28] S.C. Zhang, B.D. Goetz, J.L. Carre, I.D. Duncan, Reactive microglia in dysmyelination and demyelination, Glia, 34 (2001) 101-109.
[29] H. Neumann, M.R. Kotter, R.J. Franklin, Debris clearance by microglia: an essential link between degeneration and regeneration, Brain, 132 (2009) 288-295.
[30] M.L. Block, L. Zecca, J.S. Hong, Microglia-mediated neurotoxicity: uncovering the molecular mechanisms, Nat Rev Neurosci, 8 (2007) 57-69.
[31] R.L. Haynes, R.D. Folkerth, R.J. Keefe, I. Sung, L.I. Swzeda, P.A. Rosenberg, J.J. Volpe, H.C. Kinney, Nitrosative and oxidative injury to premyelinating oligodendrocytes in periventricular leukomalacia, J Neuropathol Exp Neurol, 62 (2003) 441-450.
[32] V.H. Perry, J.A. Nicoll, C. Holmes, Microglia in neurodegenerative disease, Nat Rev Neurol, 6 (2010) 193-201.
[33] S.W. Barger, M.E. Goodwin, M.M. Porter, M.L. Beggs, Glutamate release from activated microglia requires the oxidative burst and lipid peroxidation, J Neurochem, 101 (2007) 1205-1213.
[34] M.V. Sofroniew, Molecular dissection of reactive astrogliosis and glial scar formation, Trends Neurosci, 32 (2009) 638-647.
[35] M.V. Sofroniew, Astrocyte barriers to neurotoxic inflammation, Nat Rev Neurosci, 16 (2015) 249-263.
[36] N.J. Maragakis, J.D. Rothstein, Mechanisms of Disease: astrocytes in neurodegenerative disease, Nat Clin Pract Neurol, 2 (2006) 679-689.
[37] W.W. Chen, X. Zhang, W.J. Huang, Role of neuroinflammation in neurodegenerative diseases (Review), Mol Med Rep, 13 (2016) 3391-3396.
[38] M.A. Yenari, H.S. Han, Influence of hypothermia on post-ischemic inflammation: role of nuclear factor kappa B (NFkappaB), Neurochem Int, 49 (2006) 164-169.
[39] X. Fan, F. van Bel, Pharmacological neuroprotection after perinatal asphyxia, J Matern Fetal Neonatal Med, 23 Suppl 3 (2010) 17-19.
[40] M. Jatana, I. Singh, A.K. Singh, D. Jenkins, Combination of systemic hypothermia and N-acetylcysteine attenuates hypoxic-ischemic brain injury in neonatal rats, Pediatr Res, 59 (2006) 684-689.
[41] S. Levine, Anoxic-ischemic encephalopathy in rats, Am J Pathol, 36 (1960) 1-17.

[42] J.E. Rice, 3rd, R.C. Vannucci, J.B. Brierley, The influence of immaturity on hypoxic-ischemic brain damage in the rat, Ann Neurol, 9 (1981) 131-141.
[43] R.C. Vannucci, S.J. Vannucci, A model of perinatal hypoxic-ischemic brain damage, Ann N Y Acad Sci, 835 (1997) 234-249.
[44] J. Towfighi, J.Y. Yager, C. Housman, R.C. Vannucci, Neuropathology of remote hypoxic-ischemic damage in the immature rat, Acta Neuropathol, 81 (1991) 578-587.
[45] J. Towfighi, D. Mauger, R.C. Vannucci, S.J. Vannucci, Influence of age on the cerebral lesions in an immature rat model of cerebral hypoxia-ischemia: a light microscopic study, Brain Res Dev Brain Res, 100 (1997) 149-160.
[46] H. Sabir, E. Scull-Brown, X. Liu, M. Thoresen, Immediate hypothermia is not neuroprotective after severe hypoxia-ischemia and is deleterious when delayed by 12 hours in neonatal rats, Stroke, 43 (2012) 3364-3370.
[47] Y. Liu, F.S. Silverstein, R. Skoff, J.D. Barks, Hypoxic-ischemic oligodendroglial injury in neonatal rat brain, Pediatr Res, 51 (2002) 25-33.
[48] A. Okereafor, J. Allsop, S.J. Counsell, J. Fitzpatrick, D. Azzopardi, M.A. Rutherford, F.M. Cowan, Patterns of brain injury in neonates exposed to perinatal sentinel events, Pediatrics, 121 (2008) 906-914.
[49] L.S. de Vries, F. Groenendaal, Patterns of neonatal hypoxic-ischaemic brain injury, Neuroradiology, 52 (2010) 555-566.
[50] E. Bona, H. Hagberg, E.M. Loberg, R. Bagenholm, M. Thoresen, Protective effects of moderate hypothermia after neonatal hypoxia-ischemia: short- and long-term outcome, Pediatr Res, 43 (1998) 738-745.
[51] D. Sampath, A.M. White, Y.H. Raol, Characterization of neonatal seizures in an animal model of hypoxic-ischemic encephalopathy, Epilepsia, 55 (2014) 985-993.
[52] L.C. Weeke, G.B. Boylan, R.M. Pressler, B. Hallberg, M. Blennow, M.C. Toet, F. Groenendaal, L.S. de Vries, N.E.s.t.w.M.O.-p. consortium, Role of EEG background activity, seizure burden and MRI in predicting neurodevelopmental outcome in full-term infants with hypoxic-ischaemic encephalopathy in the era of therapeutic hypothermia, Eur J Paediatr Neurol, 20 (2016) 855-864.
[53] J.S. Wyatt, P.D. Gluckman, P.Y. Liu, D. Azzopardi, R. Ballard, A.D. Edwards, D.M. Ferriero, R.A. Polin, C.M. Robertson, M. Thoresen, A. Whitelaw, A.J. Gunn, G. CoolCap Study, Determinants of outcomes after head cooling for neonatal encephalopathy, Pediatrics, 119 (2007) 912-921.
[54] S.E. Jacobs, M. Berg, R. Hunt, W.O. Tarnow-Mordi, T.E. Inder, P.G. Davis, Cooling for newborns with hypoxic ischaemic encephalopathy, Cochrane Database Syst Rev, (2013) CD003311.
[55] P.D. Gluckman, J.S. Wyatt, D. Azzopardi, R. Ballard, A.D. Edwards, D.M. Ferriero, R.A. Polin, C.M. Robertson, M. Thoresen, A. Whitelaw, A.J. Gunn, Selective head cooling with mild systemic hypothermia after neonatal encephalopathy: multicentre randomised trial, Lancet, 365 (2005) 663-670.
[56] S. Shankaran, A.R. Laptook, R.A. Ehrenkranz, J.E. Tyson, S.A. McDonald, E.F. Donovan, A.A. Fanaroff, W.K. Poole, L.L. Wright, R.D. Higgins, N.N. Finer, W.A. Carlo, S. Duara, W. Oh, C.M. Cotten, D.K. Stevenson, B.J. Stoll, J.A. Lemons, R. Guillet, A.H. Jobe, H. National Institute of Child, N. Human Development Neonatal Research, Whole-body hypothermia for neonates with hypoxic-ischemic encephalopathy, N Engl J Med, 353 (2005) 1574-1584.
[57] D.V. Azzopardi, B. Strohm, A.D. Edwards, L. Dyet, H.L. Halliday, E. Juszczak, O. Kapellou, M. Levene, N. Marlow, E. Porter, M. Thoresen, A. Whitelaw, P. Brocklehurst, T.S. Group, Moderate hypothermia to treat perinatal asphyxial encephalopathy, N Engl J Med, 361 (2009) 1349-1358.

[58] A.R. Laptook, R.J. Corbett, R. Sterett, D. Garcia, G. Tollefsbol, Quantitative relationship between brain temperature and energy utilization rate measured in vivo using 31P and 1H magnetic resonance spectroscopy, Pediatr Res, 38 (1995) 919-925.
[59] M. Erecinska, M. Thoresen, I.A. Silver, Effects of hypothermia on energy metabolism in Mammalian central nervous system, J Cereb Blood Flow Metab, 23 (2003) 513-530.
[60] M. Thoresen, S. Satas, M. Puka-Sundvall, A. Whitelaw, A. Hallstrom, E.M. Loberg, U. Ungerstedt, P.A. Steen, H. Hagberg, Post-hypoxic hypothermia reduces cerebrocortical release of NO and excitotoxins, Neuroreport, 8 (1997) 3359-3362.
[61] G. Wassink, E.R. Gunn, P.P. Drury, L. Bennet, A.J. Gunn, The mechanisms and treatment of asphyxial encephalopathy, Front Neurosci, 8 (2014) 40.
[62] V. Roelfsema, L. Bennet, S. George, D. Wu, J. Guan, M. Veerman, A.J. Gunn, Window of opportunity of cerebral hypothermia for postischemic white matter injury in the near-term fetal sheep, J Cereb Blood Flow Metab, 24 (2004) 877-886.
[63] A.D. Edwards, X. Yue, M.V. Squier, M. Thoresen, E.B. Cady, J. Penrice, C.E. Cooper, J.S. Wyatt, E.O. Reynolds, H. Mehmet, Specific inhibition of apoptosis after cerebral hypoxia-ischaemia by moderate post-insult hypothermia, Biochem Biophys Res Commun, 217 (1995) 1193-1199.
[64] R. Askalan, C. Wang, H. Shi, E. Armstrong, J.Y. Yager, The effect of postischemic hypothermia on apoptotic cell death in the neonatal rat brain, Dev Neurosci, 33 (2011) 320-329.
[65] T.W. Pin, B. Eldridge, M.P. Galea, A review of developmental outcomes of term infants with post-asphyxia neonatal encephalopathy, Eur J Paediatr Neurol, 13 (2009) 224-234.
[66] B. Fleiss, C.J. Tann, V. Degos, S. Sigaut, J. Van Steenwinckel, A.L. Schang, A. Kichev, N.J. Robertson, C. Mallard, H. Hagberg, P. Gressens, Inflammation-induced sensitization of the brain in term infants, Dev Med Child Neurol, 57 Suppl 3 (2015) 17-28.
[67] E. Smit, X. Liu, S. Jary, F. Cowan, M. Thoresen, Cooling neonates who do not fulfil the standard cooling criteria - short- and long-term outcomes, Acta Paediatr, 104 (2015) 138-145.
[68] J. Dingley, X. Liu, H. Gill, E. Smit, H. Sabir, J. Tooley, E. Chakkarapani, D. Windsor, M. Thoresen, The feasibility of using a portable xenon delivery device to permit earlier xenon ventilation with therapeutic cooling of neonates during ambulance retrieval, Anesth Analg, 120 (2015) 1331-1336.
[69] S.E. Juul, B.A. Comstock, P.J. Heagerty, D.E. Mayock, A.M. Goodman, S. Hauge, F. Gonzalez, Y.W. Wu, High-Dose Erythropoietin for Asphyxia and Encephalopathy (HEAL): A Randomized Controlled Trial - Background, Aims, and Study Protocol, Neonatology, 113 (2018) 331-338.
[70] C.M. Traudt, R.J. McPherson, L.A. Bauer, T.L. Richards, T.M. Burbacher, R.M. McAdams, S.E. Juul, Concurrent erythropoietin and hypothermia treatment improve outcomes in a term nonhuman primate model of perinatal asphyxia, Dev Neurosci, 35 (2013) 491-503.
[71] J.Y. Yager, E.A. Armstrong, A.M. Black, Treatment of the term newborn with brain injury: simplicity as the mother of invention, Pediatr Neurol, 40 (2009) 237-243.
[72] F. Groenendaal, L.S. de Vries, Selection of babies for intervention after birth asphyxia, Semin Neonatol, 5 (2000) 17-32.
[73] T. Patel, J. Zhou, J.M. Piepmeier, W.M. Saltzman, Polymeric nanoparticles for drug delivery to the central nervous system, Adv Drug Deliv Rev, 64 (2012) 701-705.
[74] J. Kreuter, Nanoparticulate systems for brain delivery of drugs, Adv Drug Deliv Rev, 47 (2001) 65-81.
[75] S. Gelperina, O. Maksimenko, A. Khalansky, L. Vanchugova, E. Shipulo, K. Abbasova, R. Berdiev, S. Wohlfart, N. Chepurnova, J. Kreuter, Drug delivery to the brain using surfactant-coated poly(lactide-co-glycolide) nanoparticles: influence of the formulation parameters, Eur J Pharm Biopharm, 74 (2010) 157-163.
[76] N. Huang, S. Lu, X.G. Liu, J. Zhu, Y.J. Wang, R.T. Liu, PLGA nanoparticles modified with a BBB-penetrating peptide co-delivering Abeta generation inhibitor and curcumin attenuate

memory deficits and neuropathology in Alzheimer's disease mice, Oncotarget, 8 (2017) 81001-81013.
[77] S. Sathya, B. Shanmuganathan, S. Saranya, S. Vaidevi, K. Ruckmani, K. Pandima Devi, Phytol-loaded PLGA nanoparticle as a modulator of Alzheimer's toxic Abeta peptide aggregation and fibrillation associated with impaired neuronal cell function, Artif Cells Nanomed Biotechnol, (2017) 1-12.
[78] E. Sanchez-Lopez, M.A. Egea, B.M. Davis, L. Guo, M. Espina, A.M. Silva, A.C. Calpena, E.M.B. Souto, N. Ravindran, M. Ettcheto, A. Camins, M.L. Garcia, M.F. Cordeiro, Memantine-Loaded PEGylated Biodegradable Nanoparticles for the Treatment of Glaucoma, Small, 14 (2018).
[79] B. Ruozi, D. Belletti, H.S. Sharma, A. Sharma, D.F. Muresanu, H. Mossler, F. Forni, M.A. Vandelli, G. Tosi, PLGA Nanoparticles Loaded Cerebrolysin: Studies on Their Preparation and Investigation of the Effect of Storage and Serum Stability with Reference to Traumatic Brain Injury, Mol Neurobiol, 52 (2015) 899-912.
[80] K.A. Langert, B. Goshu, E.B. Stubbs, Jr., Attenuation of experimental autoimmune neuritis with locally administered lovastatin-encapsulating poly(lactic-co-glycolic) acid nanoparticles, J Neurochem, 140 (2017) 334-346.
[81] J. Tang, J. Li, G. Li, H. Zhang, L. Wang, D. Li, J. Ding, Spermidine-mediated poly(lactic-co-glycolic acid) nanoparticles containing fluorofenidone for the treatment of idiopathic pulmonary fibrosis, Int J Nanomedicine, 12 (2017) 6687-6704.
[82] Q. Cai, L. Wang, G. Deng, J. Liu, Q. Chen, Z. Chen, Systemic delivery to central nervous system by engineered PLGA nanoparticles, Am J Transl Res, 8 (2016) 749-764.
[83] E.A. Nance, G.F. Woodworth, K.A. Sailor, T.Y. Shih, Q. Xu, G. Swaminathan, D. Xiang, C. Eberhart, J. Hanes, A dense poly(ethylene glycol) coating improves penetration of large polymeric nanoparticles within brain tissue, Sci Transl Med, 4 (2012) 149ra119.
[84] R. Mehvar, Modulation of the pharmacokinetics and pharmacodynamics of proteins by polyethylene glycol conjugation, J Pharm Pharm Sci, 3 (2000) 125-136.
[85] J.S. Suk, Q. Xu, N. Kim, J. Hanes, L.M. Ensign, PEGylation as a strategy for improving nanoparticle-based drug and gene delivery, Adv Drug Deliv Rev, 99 (2016) 28-51.
[86] R. Gref, Y. Minamitake, M.T. Peracchia, V. Trubetskoy, V. Torchilin, R. Langer, Biodegradable long-circulating polymeric nanospheres, Science, 263 (1994) 1600-1603.
[87] G. Yu, Q.S. Zheng, G.F. Li, Similarities and differences in gastrointestinal physiology between neonates and adults: a physiologically based pharmacokinetic modeling perspective, AAPS J, 16 (2014) 1162-1166.
[88] E. Fernandez, R. Perez, A. Hernandez, P. Tejada, M. Arteta, J.T. Ramos, Factors and Mechanisms for Pharmacokinetic Differences between Pediatric Population and Adults, Pharmaceutics, 3 (2011) 53-72.
[89] S.B. M, W. R, B. EL, Differences in adsorption, distribution, metabolism and excretion of xenobiotics between the paediatric and adult populations, Expert Opin Drug Metab Toxicol, 1 (2005) 447-471.
[90] J.R. Kelly, P.J. Kennedy, J.F. Cryan, T.G. Dinan, G. Clarke, N.P. Hyland, Breaking down the barriers: the gut microbiome, intestinal permeability and stress-related psychiatric disorders, Front Cell Neurosci, 9 (2015) 392.
[91] C.A. Woodhouse, V.C. Patel, A. Singanayagam, D.L. Shawcross, Review article: the gut microbiome as a therapeutic target in the pathogenesis and treatment of chronic liver disease, Aliment Pharmacol Ther, 47 (2018) 192-202.
[92] P.D. Cani, N.M. Delzenne, The gut microbiome as therapeutic target, Pharmacol Ther, 130 (2011) 202-212.
[93] M.B. Delgado-Charro, R.H. Guy, Effective use of transdermal drug delivery in children, Adv Drug Deliv Rev, 73 (2014) 63-82.

[94] J.K. Lam, Y. Xu, A. Worsley, I.C. Wong, Oral transmucosal drug delivery for pediatric use, Adv Drug Deliv Rev, 73 (2014) 50-62.
[95] V. Jannin, G. Lemagnen, P. Gueroult, D. Larrouture, C. Tuleu, Rectal route in the 21st Century to treat children, Adv Drug Deliv Rev, 73 (2014) 34-49.
[96] P.C. Kwok, H.K. Chan, Delivery of inhalation drugs to children for asthma and other respiratory diseases, Adv Drug Deliv Rev, 73 (2014) 83-88.
[97] S.B. M, B. EL, Drug metabolism and disposition in children, Fundam Clin Pharmacol, 17 (2003) 281-299.
[98] H.C. Meissner, A.L. Smith, The current status of chloramphenicol, Pediatrics, 64 (1979) 348-356.
[99] M. Albani, I. Wernicke, Oral phenytoin in infancy: dose requirement, absorption, and elimination, Pediatr Pharmacol (New York), 3 (1983) 229-236.
[100] G.P. Giacoia, P. Taylor-Zapata, A. Zajicek, Eunice Kennedy Shriver National Institute of Child Health and Human Development Pediatrics Formulation Initiative: proceedings from the Second Workshop on Pediatric Formulations, Clin Ther, 34 (2012) S1-10.
[101] P. Moore, Children are not small adults, Lancet, 352 (1998) 630.
[102] J. Breitkreutz, J. Boos, Paediatric and geriatric drug delivery, Expert Opin Drug Del, 4 (2007) 37-45.
[103] G.L. Kearns, S.M. Abdel-Rahman, S.W. Alander, D.L. Blowey, J.S. Leeder, R.E. Kauffman, Developmental pharmacology--drug disposition, action, and therapy in infants and children, N Engl J Med, 349 (2003) 1157-1167.
[104] V. Ivanovska, C.M.A. Rademaker, L. van Dijk, A.K. Mantel-Teeuwisse, Pediatric Drug Formulations: A Review of Challenges and Progress, Pediatrics, 134 (2014) 361-372.
[105] K. Allegaert, Neonates need tailored drug formulations, World J Clin Pediatr, 2 (2013) 1-5.
[106] G.J. Noel, J.N. Van Den Anker, D. Lombardi, R. Ward, Improving drug formulations for neonates: making a big difference in our smallest patients, J Pediatr, 161 (2012) 947-949.
[107] V. Ivanovska, C.M. Rademaker, L. van Dijk, A.K. Mantel-Teeuwisse, Pediatric drug formulations: a review of challenges and progress, Pediatrics, 134 (2014) 361-372.
[108] T. Wood, E. Nance, Disease-directed engineering for physiology-driven treatment interventions in neurological disorders, APL Bioeng, 3 (2019) 040901.
[109] E. Nance, Brain-Penetrating Nanoparticles for Analysis of the Brain Microenvironment, Methods Mol Biol, 1570 (2017) 91-104.
[110] M.K. Mishra, C.A. Beaty, W.G. Lesniak, S.P. Kambhampati, F. Zhang, M.A. Wilson, M.E. Blue, J.C. Troncoso, S. Kannan, M.V. Johnston, W.A. Baumgartner, R.M. Kannan, Dendrimer brain uptake and targeted therapy for brain injury in a large animal model of hypothermic circulatory arrest, ACS Nano, 8 (2014) 2134-2147.
[111] W.G. Lesniak, M.K. Mishra, A. Jyoti, B. Balakrishnan, F. Zhang, E. Nance, R. Romero, S. Kannan, R.M. Kannan, Biodistribution of fluorescently labeled PAMAM dendrimers in neonatal rabbits: effect of neuroinflammation, Mol Pharm, 10 (2013) 4560-4571.
[112] F. Zhang, E. Nance, Y. Alnasser, R. Kannan, S. Kannan, Microglial migration and interactions with dendrimer nanoparticles are altered in the presence of neuroinflammation, J Neuroinflammation, 13 (2016) 65.
[113] M. Zhang, B.P. Bishop, N.L. Thompson, K. Hildahl, B. Dang, O. Mironchuk, N. Chen, R. Aoki, V.C. Holmberg, E. Nance, Quantum Dot Cellular Uptake and Toxicity in the Developing Brain: Implications for Use as Imaging Probes, Nanoscale Adv, 1 (2019) 3424-3442.
[114] Q. Xu, N.J. Boylan, S. Cai, B. Miao, H. Patel, J. Hanes, Scalable method to produce biodegradable nanoparticles that rapidly penetrate human mucus, J Control Release, 170 (2013) 279-286.
[115] R.F. Beers, Jr., I.W. Sizer, A spectrophotometric method for measuring the breakdown of hydrogen peroxide by catalase, J Biol Chem, 195 (1952) 133-140.

[116] T.D. Dziubla, A. Karim, V.R. Muzykantov, Polymer nanocarriers protecting active enzyme cargo against proteolysis, J Control Release, 102 (2005) 427-439.
[117] E. Nance, K. Timbie, G.W. Miller, J. Song, C. Louttit, A.L. Klibanov, T.Y. Shih, G. Swaminathan, R.J. Tamargo, G.F. Woodworth, J. Hanes, R.J. Price, Non-invasive delivery of stealth, brain-penetrating nanoparticles across the blood-brain barrier using MRI-guided focused ultrasound, J Control Release, 189 (2014) 123-132.
[118] E. Nance, C. Zhang, T.Y. Shih, Q. Xu, B.S. Schuster, J. Hanes, Brain-penetrating nanoparticles improve paclitaxel efficacy in malignant glioma following local administration, ACS Nano, 8 (2014) 10655-10664.
[119] T. Wagner, A. Kroll, C.R. Haramagatti, H.G. Lipinski, M. Wiemann, Classification and Segmentation of Nanoparticle Diffusion Trajectories in Cellular Micro Environments, PLoS One, 12 (2017) e0170165.
[120] C. Curtis, A. Rokem, E. Nance, diff_classifier: Parallelization of multi-particle tracking video analyses, J Open Source Softw, 4 (2019).
[121] P.H. Wu, J.M. Phillip, S.B. Khatau, W.C. Chen, J. Stirman, S. Rosseel, K. Tschudi, J. Van Patten, M. Wong, S. Gupta, A.S. Baras, J.T. Leek, A. Maitra, D. Wirtz, Evolution of cellular morpho-phenotypes in cancer metastasis, Sci Rep, 5 (2015) 18437.
[122] P. Virtanen, R. Gommers, T.E. Oliphant, M. Haberland, T. Reddy, D. Cournapeau, E. Burovski, P. Peterson, W. Weckesser, J. Bright, S.J. van der Walt, M. Brett, J. Wilson, K.J. Millman, N. Mayorov, A.R.J. Nelson, E. Jones, R. Kern, E. Larson, C.J. Carey, I. Polat, Y. Feng, E.W. Moore, J. VanderPlas, D. Laxalde, J. Perktold, R. Cimrman, I. Henriksen, E.A. Quintero, C.R. Harris, A.M. Archibald, A.H. Ribeiro, F. Pedregosa, P. van Mulbregt, C. SciPy, SciPy 1.0: fundamental algorithms for scientific computing in Python, Nat Methods, 17 (2020) 261-272.
[123] F. Pérez, B.E. Granger, IPython: a system for interactive scientific computing, Computing in Science & Engineering, 9 (2007) 21-29.
[124] T.E. Oliphant, A guide to NumPy, Trelgol Publishing USA2006.
[125] F. Pedregosa, G. Varoquaux, A. Gramfort, V. Michel, B. Thirion, O. Grisel, M. Blondel, P. Prettenhofer, R. Weiss, V. Dubourg, Scikit-learn: Machine learning in Python, the Journal of machine Learning research, 12 (2011) 2825-2830.
[126] C. McQuin, A. Goodman, V. Chernyshev, L. Kamentsky, B.A. Cimini, K.W. Karhohs, M. Doan, L. Ding, S.M. Rafelski, D. Thirstrup, W. Wiegraebe, S. Singh, T. Becker, J.C. Caicedo, A.E. Carpenter, CellProfiler 3.0: Next-generation image processing for biology, PLoS Biol, 16 (2018) e2005970.
[127] W.A. Banks, E.O. Freed, K.M. Wolf, S.M. Robinson, M. Franko, V.B. Kumar, Transport of human immunodeficiency virus type 1 pseudoviruses across the blood-brain barrier: role of envelope proteins and adsorptive endocytosis, J Virol, 75 (2001) 4681-4691.
[128] R. Natarajan, N. Northrop, B. Yamamoto, Fluorescein Isothiocyanate (FITC)-Dextran Extravasation as a Measure of Blood-Brain Barrier Permeability, Curr Protoc Neurosci, 79 (2017) 9 58 51-59 58 15.
[129] B.A. Kellert, R.J. McPherson, S.E. Juul, A comparison of high-dose recombinant erythropoietin treatment regimens in brain-injured neonatal rats, Pediatr Res, 61 (2007) 451-455.
[130] S.E. Juul, R.P. Beyer, T.K. Bammler, R.J. McPherson, J. Wilkerson, F.M. Farin, Microarray analysis of high-dose recombinant erythropoietin treatment of unilateral brain injury in neonatal mouse hippocampus, Pediatr Res, 65 (2009) 485-492.
[131] M. Thoresen, R. Bagenholm, E.M. Loberg, F. Apricena, I. Kjellmer, Posthypoxic cooling of neonatal rats provides protection against brain injury, Arch Dis Child Fetal Neonatal Ed, 74 (1996) F3-9.
[132] E. Nance, M. Porambo, F. Zhang, M.K. Mishra, M. Buelow, R. Getzenberg, M. Johnston, R.M. Kannan, A. Fatemi, S. Kannan, Systemic dendrimer-drug treatment of ischemia-induced neonatal white matter injury, J Control Release, 214 (2015) 112-120.

[133] E. Nance, F. Zhang, M.K. Mishra, Z. Zhang, S.P. Kambhampati, R.M. Kannan, S. Kannan, Nanoscale effects in dendrimer-mediated targeting of neuroinflammation, Biomaterials, 101 (2016) 96-107.
[134] M. Thoresen, R. Bagenholm, E.M. Loberg, F. Apriccna, The stress of being restrained reduces brain damage after a hypoxic-ischaemic insult in the 7-day-old rat, Neuroreport, 7 (1996) 481-484.
[135] Z.Y. Zhang, M. Jiang, J. Fang, M.F. Yang, S. Zhang, Y.X. Yin, D.W. Li, L.L. Mao, X.Y. Fu, Y.J. Hou, X.T. Fu, C.D. Fan, B.L. Sun, Enhanced Therapeutic Potential of Nano-Curcumin Against Subarachnoid Hemorrhage-Induced Blood-Brain Barrier Disruption Through Inhibition of Inflammatory Response and Oxidative Stress, Mol Neurobiol, 54 (2017) 1-14.
[136] A. Wu, E.E. Noble, E. Tyagi, Z. Ying, Y. Zhuang, F. Gomez-Pinilla, Curcumin boosts DHA in the brain: Implications for the prevention of anxiety disorders, Biochim Biophys Acta, 1852 (2015) 951-961.
[137] T. Ishrat, M.N. Hoda, M.B. Khan, S. Yousuf, M. Ahmad, M.M. Khan, A. Ahmad, F. Islam, Amelioration of cognitive deficits and neurodegeneration by curcumin in rat model of sporadic dementia of Alzheimer's type (SDAT), Eur Neuropsychopharmacol, 19 (2009) 636-647.
[138] M. Pulido-Moran, J. Moreno-Fernandez, C. Ramirez-Tortosa, M. Ramirez-Tortosa, Curcumin and Health, Molecules, 21 (2016) 264.
[139] R.A. Sharma, W.P. Steward, A.J. Gescher, Pharmacokinetics and pharmacodynamics of curcumin, Adv Exp Med Biol, 595 (2007) 453-470.
[140] M.M. Yallapu, P.K. Nagesh, M. Jaggi, S.C. Chauhan, Therapeutic Applications of Curcumin Nanoformulations, AAPS J, 17 (2015) 1341-1356.
[141] A. Mathew, T. Fukuda, Y. Nagaoka, T. Hasumura, H. Morimoto, Y. Yoshida, T. Maekawa, K. Venugopal, D.S. Kumar, Curcumin loaded-PLGA nanoparticles conjugated with Tet-1 peptide for potential use in Alzheimer's disease, PLoS One, 7 (2012) e32616.
[142] B. Ray, S. Bisht, A. Maitra, A. Maitra, D.K. Lahiri, Neuroprotective and neurorescue effects of a novel polymeric nanoparticle formulation of curcumin (NanoCurc) in the neuronal cell culture and animal model: implications for Alzheimer's disease, J Alzheimers Dis, 23 (2011) 61-77.
[143] N. Ahmad, I. Ahmad, S. Umar, Z. Iqbal, M. Samim, F.J. Ahmad, PNIPAM nanoparticles for targeted and enhanced nose-to-brain delivery of curcuminoids: UPLC/ESI-Q-ToF-MS/MS-based pharmacokinetics and pharmacodynamic evaluation in cerebral ischemia model, Drug Deliv, 23 (2016) 2095-2114.
[144] M. Orunoglu, A. Kaffashi, S.B. Pehlivan, S. Sahin, F. Soylemezoglu, K.K. Oguz, M. Mut, Effects of curcumin-loaded PLGA nanoparticles on the RG2 rat glioma model, Mater Sci Eng C Mater Biol Appl, 78 (2017) 32-38.
[145] X. Zhang, X. Li, H. Hua, A. Wang, W. Liu, Y. Li, F. Fu, Y. Shi, K. Sun, Cyclic hexapeptide-conjugated nanoparticles enhance curcumin delivery to glioma tumor cells and tissue, Int J Nanomedicine, 12 (2017) 5717-5732.
[146] H.C. Huang, K. Xu, Z.F. Jiang, Curcumin-mediated neuroprotection against amyloid-beta-induced mitochondrial dysfunction involves the inhibition of GSK-3beta, J Alzheimers Dis, 32 (2012) 981-996.
[147] J. Luo, R. Borgens, R. Shi, Polyethylene glycol immediately repairs neuronal membranes and inhibits free radical production after acute spinal cord injury, J Neurochem, 83 (2002) 471-480.
[148] T. Wood, D. Osredkar, M. Puchades, E. Maes, M. Falck, T. Flatebo, L. Walloe, H. Sabir, M. Thoresen, Treatment temperature and insult severity influence the neuroprotective effects of therapeutic hypothermia, Sci Rep, 6 (2016) 23430.
[149] R.C. Vannucci, J. Towfighi, D.F. Heitjan, R.M. Brucklacher, Carbon dioxide protects the perinatal brain from hypoxic-ischemic damage: an experimental study in the immature rat, Pediatrics, 95 (1995) 868-874.

[150] H. Sabir, D. Osredkar, E. Maes, T. Wood, M. Thoresen, Xenon Combined with Therapeutic Hypothermia Is Not Neuroprotective after Severe Hypoxia-Ischemia in Neonatal Rats, PLoS One, 11 (2016) e0156759.
[151] Y. Wang, S.Y. Li, S. Shen, J. Wang, Protecting neurons from cerebral ischemia/reperfusion injury via nanoparticle-mediated delivery of an siRNA to inhibit microglial neurotoxicity, Biomaterials, 161 (2018) 95-105.
[152] T. Ishii, T. Fukuta, Y. Agato, D. Oyama, N. Yasuda, K. Shimizu, A.T. Kawaguchi, T. Asai, N. Oku, Nanoparticles accumulate in ischemic core and penumbra region even when cerebral perfusion is reduced, Biochem Biophys Res Commun, 430 (2013) 1201-1205.
[153] A. Ambruosi, S. Gelperina, A. Khalansky, S. Tanski, A. Theisen, J. Kreuter, Influence of surfactants, polymer and doxorubicin loading on the anti-tumour effect of poly(butyl cyanoacrylate) nanoparticles in a rat glioma model, J Microencapsul, 23 (2006) 582-592.
[154] A. Ambruosi, A.S. Khalansky, H. Yamamoto, S.E. Gelperina, D.J. Begley, J. Kreuter, Biodistribution of polysorbate 80-coated doxorubicin-loaded [14C]-poly(butyl cyanoacrylate) nanoparticles after intravenous administration to glioblastoma-bearing rats, J Drug Target, 14 (2006) 97-105.
[155] S.A. Kulkarni, S.S. Feng, Effects of surface modification on delivery efficiency of biodegradable nanoparticles across the blood-brain barrier, Nanomedicine (Lond), 6 (2011) 377-394.
[156] J.H. Na, H. Koo, S. Lee, K.H. Min, K. Park, H. Yoo, S.H. Lee, J.H. Park, I.C. Kwon, S.Y. Jeong, K. Kim, Real-time and non-invasive optical imaging of tumor-targeting glycol chitosan nanoparticles in various tumor models, Biomaterials, 32 (2011) 5252-5261.
[157] R. Gref, M. Luck, P. Quellec, M. Marchand, E. Dellacherie, S. Harnisch, T. Blunk, R.H. Muller, 'Stealth' corona-core nanoparticles surface modified by polyethylene glycol (PEG): influences of the corona (PEG chain length and surface density) and of the core composition on phagocytic uptake and plasma protein adsorption, Colloids Surf B Biointerfaces, 18 (2000) 301-313.
[158] S. Stolnik, S.E. Dunn, M.C. Garnett, M.C. Davies, A.G. Coombes, D.C. Taylor, M.P. Irving, S.C. Purkiss, T.F. Tadros, S.S. Davis, et al., Surface modification of poly(lactide-co-glycolide) nanospheres by biodegradable poly(lactide)-poly(ethylene glycol) copolymers, Pharm Res, 11 (1994) 1800-1808.
[159] R. Langer, Drug delivery and targeting, Nature, 392 (1998) 5-10.
[160] C. Zhang, E.A. Nance, P. Mastorakos, J. Chisholm, S. Berry, C. Eberhart, B. Tyler, H. Brem, J.S. Suk, J. Hanes, Convection enhanced delivery of cisplatin-loaded brain penetrating nanoparticles cures malignant glioma in rats, J Control Release, 263 (2017) 112-119.
[161] R.Z. Xiao, Z.W. Zeng, G.L. Zhou, J.J. Wang, F.Z. Li, A.M. Wang, Recent advances in PEG-PLA block copolymer nanoparticles, Int J Nanomedicine, 5 (2010) 1057-1065.
[162] S.D. Allison, Analysis of initial burst in PLGA microparticles, Expert Opin Drug Deliv, 5 (2008) 615-628.
[163] C. Yang, X. Zhang, H. Fan, Y. Liu, Curcumin upregulates transcription factor Nrf2, HO-1 expression and protects rat brains against focal ischemia, Brain Res, 1282 (2009) 133-141.
[164] T. Esatbeyoglu, P. Huebbe, I.M. Ernst, D. Chin, A.E. Wagner, G. Rimbach, Curcumin--from molecule to biological function, Angew Chem Int Ed Engl, 51 (2012) 5308-5332.
[165] J.K. Lin, Molecular targets of curcumin, Adv Exp Med Biol, 595 (2007) 227-243.
[166] H.T. Zhu, C. Bian, J.C. Yuan, W.H. Chu, X. Xiang, F. Chen, C.S. Wang, H. Feng, J.K. Lin, Curcumin attenuates acute inflammatory injury by inhibiting the TLR4/MyD88/NF-kappaB signaling pathway in experimental traumatic brain injury, J Neuroinflammation, 11 (2014) 59.
[167] Z.J. Liu, W. Liu, L. Liu, C. Xiao, Y. Wang, J.S. Jiao, Curcumin Protects Neuron against Cerebral Ischemia-Induced Inflammation through Improving PPAR-Gamma Function, Evid Based Complement Alternat Med, 2013 (2013) 470975.

[168] H.C. Huang, P. Chang, S.Y. Lu, B.W. Zheng, Z.F. Jiang, Protection of curcumin against amyloid-beta-induced cell damage and death involves the prevention from NMDA receptor-mediated intracellular Ca2+ elevation, J Recept Signal Transduct Res, 35 (2015) 450-457.
[169] S.K. Tiwari, S. Agarwal, B. Seth, A. Yadav, S. Nair, P. Bhatnagar, M. Karmakar, M. Kumari, L.K. Chauhan, D.K. Patel, V. Srivastava, D. Singh, S.K. Gupta, A. Tripathi, R.K. Chaturvedi, K.C. Gupta, Curcumin-loaded nanoparticles potently induce adult neurogenesis and reverse cognitive deficits in Alzheimer's disease model via canonical Wnt/beta-catenin pathway, ACS Nano, 8 (2014) 76-103.
[170] A. Ameruoso, R. Palomba, A.L. Palange, A. Cervadoro, A. Lee, D. Di Mascolo, P. Decuzzi, Ameliorating Amyloid-beta Fibrils Triggered Inflammation via Curcumin-Loaded Polymeric Nanoconstructs, Front Immunol, 8 (2017) 1411.
[171] A. Umerska, C. Gaucher, F. Oyarzun-Ampuero, I. Fries-Raeth, F. Colin, M.G. Villamizar-Sarmiento, P. Maincent, A. Sapin-Minet, Polymeric Nanoparticles for Increasing Oral Bioavailability of Curcumin, Antioxidants (Basel), 7 (2018).
[172] P. Verderio, P. Bonetti, M. Colombo, L. Pandolfi, D. Prosperi, Intracellular drug release from curcumin-loaded PLGA nanoparticles induces G2/M block in breast cancer cells, Biomacromolecules, 14 (2013) 672-682.
[173] R.K. Basniwal, R. Khosla, N. Jain, Improving the anticancer activity of curcumin using nanocurcumin dispersion in water, Nutr Cancer, 66 (2014) 1015-1022.
[174] H.R. Berger, T.S. Morken, R. Vettukattil, A.M. Brubakk, U. Sonnewald, M. Wideroe, No improvement of neuronal metabolism in the reperfusion phase with melatonin treatment after hypoxic-ischemic brain injury in the neonatal rat, J Neurochem, 136 (2016) 339-350.
[175] A.M. Di Giorgio, Y. Hou, X. Zhao, B. Zhang, B.G. Lyeth, M.J. Russell, Dimethyl sulfoxide provides neuroprotection in a traumatic brain injury model, Restor Neurol Neurosci, 26 (2008) 501-507.
[176] A.L. Smith, H. Garbus, T.S. Rosenkrantz, R.H. Fitch, Sex differences in behavioral outcomes following temperature modulation during induced neonatal hypoxic ischemic injury in rats, Brain Sci, 5 (2015) 220-240.
[177] A.L. Smith, M. Alexander, T.S. Rosenkrantz, M.L. Sadek, R.H. Fitch, Sex differences in behavioral outcome following neonatal hypoxia ischemia: insights from a clinical meta-analysis and a rodent model of induced hypoxic ischemic brain injury, Exp Neurol, 254 (2014) 54-67.
[178] J.C. Burnsed, R. Chavez-Valdez, M.S. Hossain, K. Kesavan, L.J. Martin, J. Zhang, F.J. Northington, Hypoxia-ischemia and therapeutic hypothermia in the neonatal mouse brain--a longitudinal study, PLoS One, 10 (2015) e0118889.
[179] S.S. Cohen, B.S. Stonestreet, Sex differences in behavioral outcome following neonatal hypoxia ischemia: Insights from a clinical meta-analysis and a rodent model of induced hypoxic ischemic injury, Exp Neurol, 256 (2014) 70-73.
[180] X. Nie, D.W. Lowe, L.G. Rollins, J. Bentzley, J.L. Fraser, R. Martin, I. Singh, D. Jenkins, Sex-specific effects of N-acetylcysteine in neonatal rats treated with hypothermia after severe hypoxia-ischemia, Neurosci Res, 108 (2016) 24-33.
[181] T.G. Demarest, M.M. McCarthy, Sex differences in mitochondrial (dys)function: Implications for neuroprotection, J Bioenerg Biomembr, 47 (2015) 173-188.
[182] M. Douglas-Escobar, M.D. Weiss, Hypoxic-ischemic encephalopathy: a review for the clinician, JAMA pediatrics, 169 (2015) 397-403.
[183] W. Johnson, O. Onuma, M. Owolabi, S. Sachdev, Stroke: a global response is needed, Bulletin of the World Health Organization, 94 (2016) 634.
[184] A.D. Edwards, P. Brocklehurst, A.J. Gunn, H. Halliday, E. Juszczak, M. Levene, B. Strohm, M. Thoresen, A. Whitelaw, D. Azzopardi, Neurological outcomes at 18 months of age after moderate hypothermia for perinatal hypoxic ischaemic encephalopathy: synthesis and meta-analysis of trial data, Bmj, 340 (2010) c363.

[185] G.W. Albers, P. Amarenco, J.D. Easton, R.L. Sacco, P. Teal, Antithrombotic and thrombolytic therapy for ischemic stroke: the Seventh ACCP Conference on Antithrombotic and Thrombolytic Therapy, Chest, 126 (2004) 483S-512S.
[186] J. Priller, M. Prinz, Targeting microglia in brain disorders, Science, 365 (2019) 32-33.
[187] S. Wohlfart, S. Gelperina, J. Kreuter, Transport of drugs across the blood-brain barrier by nanoparticles, J Control Release, 161 (2012) 264-273.
[188] E. Nance, S.P. Kambhampati, E.S. Smith, Z. Zhang, F. Zhang, S. Singh, M.V. Johnston, R.M. Kannan, M.E. Blue, S. Kannan, Dendrimer-mediated delivery of N-acetyl cysteine to microglia in a mouse model of Rett syndrome, J Neuroinflammation, 14 (2017) 252.
[189] C. Curtis, M. Zhang, R. Liao, T. Wood, E. Nance, Systems-level thinking for nanoparticle-mediated therapeutic delivery to neurological diseases, Wiley Interdiscip Rev Nanomed Nanobiotechnol, 9 (2017).
[190] R. Liao, T.R. Wood, E. Nance, Superoxide dismutase reduces monosodium glutamate-induced injury in an organotypic whole hemisphere brain slice model of excitotoxicity, J Biol Eng, 14 (2020) 3.
[191] R. Liao, J. Pon, M. Chungyoun, E. Nance, Enzymatic protection and biocompatibility screening of enzyme-loaded polymeric nanoparticles for neurotherapeutic applications, Biomaterials, (2020) 120238.
[192] C.I. Tasca, T. Dal-Cim, H. Cimarosti, In vitro oxygen-glucose deprivation to study ischemic cell death, Methods Mol Biol, 1254 (2015) 197-210.
[193] S. Fujimoto, H. Katsuki, T. Kume, S. Kaneko, A. Akaike, Mechanisms of oxygen glucose deprivation-induced glutamate release from cerebrocortical slice cultures, Neurosci Res, 50 (2004) 179-187.
[194] A.A. Hall, C.C. Leonardo, L.A. Collier, D.D. Rowe, A.E. Willing, K.R. Pennypacker, Delayed treatments for stroke influence neuronal death in rat organotypic slice cultures subjected to oxygen glucose deprivation, Neuroscience, 164 (2009) 470-477.
[195] J. De Alba, A. Cardenas, M.A. Moro, J.C. Leza, P. Lorenzo, L. Bosca, I. Lizasoain, Down-regulation of neuronal nitric oxide synthase by nitric oxide after oxygen-glucose deprivation in rat forebrain slices, J Neurochem, 72 (1999) 248-254.
[196] D. Amantea, M. Certo, F. Petrelli, C. Tassorelli, G. Micieli, M.T. Corasaniti, P. Puccetti, F. Fallarino, G. Bagetta, Azithromycin protects mice against ischemic stroke injury by promoting macrophage transition towards M2 phenotype, Exp Neurol, 275 Pt 1 (2016) 116-125.
[197] M.J. Parnham, V. Erakovic Haber, E.J. Giamarellos-Bourboulis, G. Perletti, G.M. Verleden, R. Vos, Azithromycin: mechanisms of action and their relevance for clinical applications, Pharmacol Ther, 143 (2014) 225-245.
[198] A. Bosco, C.O. Romero, K.T. Breen, A.A. Chagovetz, M.R. Steele, B.K. Ambati, M.L. Vetter, Neurodegeneration severity can be predicted from early microglia alterations monitored in vivo in a mouse model of chronic glaucoma, Dis Model Mech, 8 (2015) 443-455.
[199] N. Pavese, A. Gerhard, Y.F. Tai, A.K. Ho, F. Turkheimer, R.A. Barker, D.J. Brooks, P. Piccini, Microglial activation correlates with severity in Huntington disease: a clinical and PET study, Neurology, 66 (2006) 1638-1643.
[200] J.D.E. Barks, Y. Liu, L. Wang, M.P. Pai, F.S. Silverstein, Repurposing azithromycin for neonatal neuroprotection, Pediatr Res, 86 (2019) 444-451.
[201] J.L. Saver, Time is brain—quantified, Stroke, 37 (2006) 263-266.
[202] L.J. Lawson, V.H. Perry, P. Dri, S. Gordon, Heterogeneity in the distribution and morphology of microglia in the normal adult mouse brain, Neuroscience, 39 (1990) 151-170.
[203] D. Gomez-Nicola, V.H. Perry, Microglial dynamics and role in the healthy and diseased brain: a paradigm of functional plasticity, Neuroscientist, 21 (2015) 169-184.
[204] B. Amsden, Solute diffusion within hydrogels. Mechanisms and models, Macromolecules, 31 (1998) 8382-8395.

[205] U. Strasser, G. Fischer, Quantitative measurement of neuronal degeneration in organotypic hippocampal cultures after combined oxygen/glucose deprivation, J Neurosci Methods, 57 (1995) 177-186.
[206] P.M. Holloway, F.N. Gavins, Modeling Ischemic Stroke In Vitro: Status Quo and Future Perspectives, Stroke, 47 (2016) 561-569.
[207] A. Kalda, E. Eriste, V. Vassiljev, A. Zharkovsky, Medium transitory oxygen-glucose deprivation induced both apoptosis and necrosis in cerebellar granule cells, Neurosci Lett, 240 (1998) 21-24.
[208] B.J. Gwag, D. Lobner, J.Y. Koh, M.B. Wie, D.W. Choi, Blockade of glutamate receptors unmasks neuronal apoptosis after oxygen-glucose deprivation in vitro, Neuroscience, 68 (1995) 615-619.
[209] D. Fernandez-Lopez, J. Martinez-Orgado, I. Casanova, B. Bonet, J.C. Leza, P. Lorenzo, M.A. Moro, I. Lizasoain, Immature rat brain slices exposed to oxygen-glucose deprivation as an in vitro model of neonatal hypoxic-ischemic encephalopathy, J Neurosci Methods, 145 (2005) 205-212.
[210] R. Berger, A. Jensen, K.A. Hossmann, W. Paschen, Effect of mild hypothermia during and after transient in vitro ischemia on metabolic disturbances in hippocampal slices at different stages of development, Brain Res Dev Brain Res, 105 (1998) 67-77.
[211] K. Brongholi, D.G. Souza, A.C. Bainy, A.L. Dafre, C.I. Tasca, Oxygen–glucose deprivation decreases glutathione levels and glutamate uptake in rat hippocampal slices, Brain research, 1083 (2006) 211-218.
[212] V. Ravindranath, D.J. Reed, Glutathione depletion and formation of glutathione-protein mixed disulfide following exposure of brain mitochondria to oxidative stress, Biochem Biophys Res Commun, 169 (1990) 1075-1079.
[213] I. Burd, F. Zhang, T. Dada, M.K. Mishra, T. Borbiev, W.G. Lesniak, H. Baghlaf, S. Kannan, R.M. Kannan, Fetal uptake of intra-amniotically delivered dendrimers in a mouse model of intrauterine inflammation and preterm birth, Nanomedicine, 10 (2014) 1343-1351.
[214] C.L. Nemeth, G.T. Drummond, M.K. Mishra, F. Zhang, P. Carr, M.S. Garcia, S. Doman, A. Fatemi, M.V. Johnston, R.M. Kannan, S. Kannan, M.A. Wilson, Uptake of dendrimer-drug by different cell types in the hippocampus after hypoxic-ischemic insult in neonatal mice: Effects of injury, microglial activation and hypothermia, Nanomedicine, 13 (2017) 2359-2369.
[215] S.P. Kambhampati, A.J. Clunies-Ross, I. Bhutto, M.K. Mishra, M. Edwards, D.S. McLeod, R.M. Kannan, G. Lutty, Systemic and Intravitreal Delivery of Dendrimers to Activated Microglia/Macrophage in Ischemia/Reperfusion Mouse Retina, Invest Ophthalmol Vis Sci, 56 (2015) 4413-4424.
[216] S. Girard, D. Brough, G. Lopez-Castejon, J. Giles, N.J. Rothwell, S.M. Allan, Microglia and macrophages differentially modulate cell death after brain injury caused by oxygen-glucose deprivation in organotypic brain slices, Glia, 61 (2013) 813-824.
[217] H.S. Suh, M.O. Kim, S.C. Lee, Inhibition of granulocyte-macrophage colony-stimulating factor signaling and microglial proliferation by anti-CD45RO: role of Hck tyrosine kinase and phosphatidylinositol 3-kinase/Akt, J Immunol, 174 (2005) 2712-2719.
[218] O.M. Mitrasinovic, A. Grattan, C.C. Robinson, N.B. Lapustea, C. Poon, H. Ryan, C. Phong, G.M. Murphy, Jr., Microglia overexpressing the macrophage colony-stimulating factor receptor are neuroprotective in a microglial-hippocampal organotypic coculture system, J Neurosci, 25 (2005) 4442-4451.
[219] A.K. Mausberg, S. Jander, G. Reichmann, Intracerebral granulocyte-macrophage colony-stimulating factor induces functionally competent dendritic cells in the mouse brain, Glia, 57 (2009) 1341-1350.
[220] M.L. Dubbelaar, L. Kracht, B.J.L. Eggen, E. Boddeke, The Kaleidoscope of Microglial Phenotypes, Front Immunol, 9 (2018) 1753.

[221] F. Zhang, Y.A. Lin, S. Kannan, R.M. Kannan, Targeting specific cells in the brain with nanomedicines for CNS therapies, Journal of controlled release : official journal of the Controlled Release Society, 240 (2016) 212-226.
[222] B. Choi, M. Soh, Y. Manandhar, D. Kim, S.I. Han, S. Baik, K. Shin, S. Koo, H.J. Kwon, G. Ko, J. Oh, H. Hwang, T. Hyeon, S.J. Lee, Highly selective microglial uptake of ceria-zirconia nanoparticles for enhanced analgesic treatment of neuropathic pain, Nanoscale, 11 (2019) 19437-19447.
[223] F.Y. McWhorter, T. Wang, P. Nguyen, T. Chung, W.F. Liu, Modulation of macrophage phenotype by cell shape, Proceedings of the National Academy of Sciences, 110 (2013) 17253-17258.
[224] M.D.M. Fernandez-Arjona, J.M. Grondona, P. Granados-Duran, P. Fernandez-Llebrez, M.D. Lopez-Avalos, Microglia Morphological Categorization in a Rat Model of Neuroinflammation by Hierarchical Cluster and Principal Components Analysis, Front Cell Neurosci, 11 (2017) 235.
[225] R.M. Ransohoff, A polarizing question: do M1 and M2 microglia exist?, Nature neuroscience, 19 (2016) 987.
[226] M.J. Bottema, Circularity of objects in images, 2000 IEEE International Conference on Acoustics, Speech, and Signal Processing. Proceedings (Cat. No. 00CH37100), IEEE, 2000, pp. 2247-2250.
[227] E.S. Smith, J.E. Porterfield, R.M. Kannan, Leveraging the interplay of nanotechnology and neuroscience: Designing new avenues for treating central nervous system disorders, Adv Drug Deliv Rev, 148 (2019) 181-203.
[228] R.M. Kannan, E. Nance, S. Kannan, D.A. Tomalia, Emerging concepts in dendrimer-based nanomedicine: from design principles to clinical applications, J Intern Med, 276 (2014) 579-617.
[229] J. Sun, L. Zhang, J. Wang, Q. Feng, D. Liu, Q. Yin, D. Xu, Y. Wei, B. Ding, X. Shi, X. Jiang, Tunable rigidity of (polymeric core)-(lipid shell) nanoparticles for regulated cellular uptake, Adv Mater, 27 (2015) 1402-1407.
[230] E. Hutter, S. Boridy, S. Labrecque, M. Lalancette-Hebert, J. Kriz, F.M. Winnik, D. Maysinger, Microglial response to gold nanoparticles, ACS Nano, 4 (2010) 2595-2606.
[231] A.D. Ducray, A. Stojiljkovic, A. Moller, M.H. Stoffel, H.R. Widmer, M. Frenz, M. Mevissen, Uptake of silica nanoparticles in the brain and effects on neuronal differentiation using different in vitro models, Nanomedicine, 13 (2017) 1195-1204.
[232] E. Nance, C. Zhang, T.-Y. Shih, Q. Xu, B.S. Schuster, J. Hanes, Brain-penetrating nanoparticles improve paclitaxel efficacy in malignant glioma following local administration, ACS nano, 8 (2014) 10655-10664.
[233] C. Zhang, P. Mastorakos, M. Sobral, S. Berry, E. Song, E. Nance, C.G. Eberhart, J. Hanes, J.S. Suk, Strategies to enhance the distribution of nanotherapeutics in the brain, Journal of Controlled Release, 267 (2017) 232-239.
[234] M.E. Rice, C. Nicholson, Diffusion characteristics and extracellular volume fraction during normoxia and hypoxia in slices of rat neostriatum, J Neurophysiol, 65 (1991) 264-272.
[235] M.A. Perez-Pinzon, L. Tao, C. Nicholson, Extracellular potassium, volume fraction, and tortuosity in rat hippocampal CA1, CA3, and cortical slices during ischemia, J Neurophysiol, 74 (1995) 565-573.
[236] E. Sykova, C. Nicholson, Diffusion in brain extracellular space, Physiol Rev, 88 (2008) 1277-1340.
[237] G.J. del Zoppo, R. Milner, T. Mabuchi, S. Hung, X. Wang, G.I. Berg, J.A. Koziol, Microglial activation and matrix protease generation during focal cerebral ischemia, Stroke, 38 (2007) 646-651.
[238] C.D. Brisson, M.K. Lukewich, R.D. Andrew, A distinct boundary between the higher brain's susceptibility to ischemia and the lower brain's resistance, PLoS One, 8 (2013).

[239] U. Dirnagl, Inflammation in stroke: the good, the bad, and the unknown, Ernst Schering Res Found Workshop, (2004) 87-99.
[240] E. Veal, A. Day, Hydrogen peroxide as a signaling molecule, Mary Ann Liebert, Inc. 140 Huguenot Street, 3rd Floor New Rochelle, NY 10801 USA, 2011.
[241] T.M. Buetler, A. Krauskopf, U.T. Ruegg, Role of superoxide as a signaling molecule, Physiology, 19 (2004) 120-123.
[242] G.P. Varano, V. Parisi, A. Adornetto, F. Cavaliere, D. Amantea, C. Nucci, M.T. Corasaniti, L.A. Morrone, G. Bagetta, R. Russo, Post-ischemic treatment with azithromycin protects ganglion cells against retinal ischemia/reperfusion injury in the rat, Mol Vis, 23 (2017) 911-921.
[243] S. Cuevas, Y. Yang, I. Armando, P.A. Jose, Mechanisms involved in the antioxidant properties of azithromycin in lung epithelial cells stimulated with cigarette smoke extract, The FASEB Journal, 30 (2016) 982.982-982.982.
[244] H.L. Wong, X.Y. Wu, R. Bendayan, Nanotechnological advances for the delivery of CNS therapeutics, Adv Drug Deliv Rev, 64 (2012) 686-700.
[245] G. Tosi, L. Costantino, B. Ruozi, F. Forni, M.A. Vandelli, Polymeric nanoparticles for the drug delivery to the central nervous system, Expert Opin Drug Deliv, 5 (2008) 155-174.
[246] S. Wohlfart, A.S. Khalansky, S. Gelperina, O. Maksimenko, C. Bernreuther, M. Glatzel, J. Kreuter, Efficient chemotherapy of rat glioblastoma using doxorubicin-loaded PLGA nanoparticles with different stabilizers, PLoS One, 6 (2011) e19121.
[247] Z. Liu, X. Gao, T. Kang, M. Jiang, D. Miao, G. Gu, Q. Hu, Q. Song, L. Yao, Y. Tu, H. Chen, X. Jiang, J. Chen, B6 peptide-modified PEG-PLA nanoparticles for enhanced brain delivery of neuroprotective peptide, Bioconjug Chem, 24 (2013) 997-1007.
[248] A. Joseph, T. Wood, C.C. Chen, K. Corry, J.M. Snyder, S.E. Juul, P. Parikh, E. Nance, Curcumin-loaded polymeric nanoparticles for neuro-protection in neonatal rats with hypoxic-ischemic encephalopathy, Nano Res, 11 (2018) 5670-5688.
[249] B.M.D.C. Godinho, J.R. Ogier, R. Darcy, C.M. Driscoll, J.F. Cryan, Self-assembling Modified beta-Cyclodextrin Nanoparticles as Neuronal siRNA Delivery Vectors: Focus on Huntington's Disease, Mol Pharmaceut, 10 (2013) 640-649.
[250] I. Khalin, R. Alyautdin, T.W. Wong, J. Gnanou, G. Kocherga, J. Kreuter, Brain-derived neurotrophic factor delivered to the brain using poly (lactide-co-glycolide) nanoparticles improves neurological and cognitive outcome in mice with traumatic brain injury, Drug Deliv, 23 (2016) 3520-3528.
[251] E. Lepeltier, C. Bourgaux, P. Couvreur, Nanoprecipitation and the "Ouzo effect": Application to drug delivery devices, Adv Drug Deliv Rev, 71 (2014) 86-97.
[252] J. Kreuter, D. Shamenkov, V. Petrov, P. Ramge, K. Cychutek, C. Koch-Brandt, R. Alyautdin, Apolipoprotein-mediated transport of nanoparticle-bound drugs across the blood-brain barrier, J Drug Target, 10 (2002) 317-325.
[253] J. Kreuter, Influence of the surface properties on nanoparticle-mediated transport of drugs to the brain, J Nanosci Nanotechno, 4 (2004) 484-488.
[254] Y.I. Lo, Relationships between the hydrophilic-lipophilic balance values of pharmaceutical excipients and their multidrug resistance modulating effect in Caco-2 cells and rat intestines, J Control Release, 90 (2003) 37-48.
[255] A. Jain, A. Jain, N.K. Garg, R.K. Tyagi, B. Singh, O.P. Katare, T.J. Webster, V. Soni, Surface engineered polymeric nanocarriers mediate the delivery of transferrin-methotrexate conjugates for an improved understanding of brain cancer, Acta Biomater, 24 (2015) 140-151.
[256] Q.G. Xu, L.M. Ensign, N.J. Boylan, A. Schon, X.Q. Gong, J.C. Yang, N.W. Lamb, S.T. Cai, T. Yu, E. Freire, J. Hanes, Impact of Surface Polyethylene Glycol (PEG) Density on Biodegradable Nanoparticle Transport in Mucus ex Vivo and Distribution in Vivo, Acs Nano, 9 (2015) 9217-9227.

[257] M. Yang, S.K. Lai, T. Yu, Y.Y. Wang, C. Happe, W. Zhong, M. Zhang, A. Anonuevo, C. Fridley, A. Hung, J. Fu, J. Hanes, Nanoparticle penetration of human cervicovaginal mucus: the effect of polyvinyl alcohol, J Control Release, 192 (2014) 202-208.
[258] C. Curtis, D. Toghani, B. Wong, E. Nance, Colloidal stability as a determinant of nanoparticle behavior in the brain, Colloids Surf B Biointerfaces, 170 (2018) 673-682.
[259] E. Altuntas, U.S. Schubert, "Polymeromics": Mass spectrometry based strategies in polymer science toward complete sequencing approaches: a review, Anal Chim Acta, 808 (2014) 56-69.
[260] A. Joseph, R. Liao, M. Zhang, H. Helmbrecht, M. McKenna, J.R. Filteau, E. Nance, Nanoparticle-microglial interaction in the ischemic brain is modulated by injury duration and treatment, Bioeng Transl Med, 5 (2020) e10175.
[261] I. Hering, E. Eilebrecht, M.J. Parnham, N. Gunday-Tureli, A.E. Tureli, M. Weiler, C. Schafers, M. Fenske, M.G. Wacker, Evaluation of potential environmental toxicity of polymeric nanomaterials and surfactants, Environ Toxicol Pharmacol, 76 (2020) 103353.
[262] A. Cox, P. Andreozzi, R. Dal Magro, F. Fiordaliso, A. Corbelli, L. Talamini, C. Chinello, F. Raimondo, F. Magni, M. Tringali, S. Krol, P. Jacob Silva, F. Stellacci, M. Masserini, F. Re, Evolution of Nanoparticle Protein Corona across the Blood-Brain Barrier, Acs Nano, 12 (2018) 7292-7300.
[263] Y.C. Chen, W.Y. Hsieh, W.F. Lee, D.T. Zeng, Effects of surface modification of PLGA-PEG-PLGA nanoparticles on loperamide delivery efficiency across the blood-brain barrier, J Biomater Appl, 27 (2013) 909-922.
[264] G. Mittal, H. Carswell, R. Brett, S. Currie, M.N. Kumar, Development and evaluation of polymer nanoparticles for oral delivery of estradiol to rat brain in a model of Alzheimer's pathology, J Control Release, 150 (2011) 220-228.
[265] M. Chaturvedi, Y. Molino, B. Sreedhar, M. Khrestchatisky, L. Kaczmarek, Tissue inhibitor of matrix metalloproteinases-1 loaded poly(lactic-co-glycolic acid) nanoparticles for delivery across the blood-brain barrier, Int J Nanomedicine, 9 (2014) 575-588.
[266] K. Tahara, Y. Miyazaki, Y. Kawashima, J. Kreuter, H. Yamamoto, Brain targeting with surface-modified poly(D,L-lactic-co-glycolic acid) nanoparticles delivered via carotid artery administration, Eur J Pharm Biopharm, 77 (2011) 84-88.
[267] H. Helmbrecht, A. Joseph, M. McKenna, M. Zhang, E. Nance, Governing Transport Principles for Nanotherapeutic Application in the Brain, Curr Opin Chem Eng, 30 (2020) 112-119.
[268] A. Zensi, D. Begley, C. Pontikis, C. Legros, L. Mihoreanu, S. Wagner, C. Buchel, H. von Briesen, J. Kreuter, Albumin nanoparticles targeted with Apo E enter the CNS by transcytosis and are delivered to neurones, J Control Release, 137 (2009) 78-86.
[269] L.Y. Zhang, P. Lin, J. Pan, Y. Ma, Z. Wei, L. Jiang, L. Wang, Y. Song, Y. Wang, Z. Zhang, K. Jin, Q. Wang, G.Y. Yang, CLARITY for High-resolution Imaging and Quantification of Vasculature in the Whole Mouse Brain, Aging Dis, 9 (2018) 262-272.
[270] M. Vanlandewijck, L. He, M.A. Mae, J. Andrae, K. Ando, F. Del Gaudio, K. Nahar, T. Lebouvier, B. Lavina, L. Gouveia, Y. Sun, E. Raschperger, M. Rasanen, Y. Zarb, N. Mochizuki, A. Keller, U. Lendahl, C. Betsholtz, A molecular atlas of cell types and zonation in the brain vasculature, Nature, 554 (2018) 475-480.
[271] S. Hrabetova, D. Masri, L. Tao, F. Xiao, C. Nicholson, Calcium diffusion enhanced after cleavage of negatively charged components of brain extracellular matrix by chondroitinase ABC, J Physiol, 587 (2009) 4029-4049.
[272] B. Weir, Subarachnoid hemorrhage : causes and cures, Oxford University Press, New York, 1998.
[273] C. Nicholson, S. Hrabetova, Brain Extracellular Space: The Final Frontier of Neuroscience, Biophys J, 113 (2017) 2133-2142.

[274] I. Canton, G. Battaglia, Endocytosis at the nanoscale, Chem Soc Rev, 41 (2012) 2718-2739.
[275] D.E. Owens, 3rd, N.A. Peppas, Opsonization, biodistribution, and pharmacokinetics of polymeric nanoparticles, Int J Pharm, 307 (2006) 93-102.
[276] L. Illum, L.O. Jacobsen, R.H. Muller, E. Mak, S.S. Davis, Surface Characteristics and the Interaction of Colloidal Particles with Mouse Peritoneal-Macrophages, Biomaterials, 8 (1987) 113-117.
[277] Y.W. Wu, K.H. Backstrand, S. Zhao, H.J. Fullerton, S.C. Johnston, Declining diagnosis of birth asphyxia in California: 1991-2000, Pediatrics, 114 (2004) 1584-1590.
[278] S. Shankaran, A.R. Laptook, A. Pappas, S.A. McDonald, A. Das, J.E. Tyson, B.B. Poindexter, K. Schibler, E.F. Bell, R.J. Heyne, C. Pedroza, R. Bara, K.P. Van Meurs, C.M.P. Huitema, C. Grisby, U. Devaskar, R.A. Ehrenkranz, H.M. Harmon, L.F. Chalak, S.B. DeMauro, M. Garg, M.E. Hartley-McAndrew, A.M. Khan, M.C. Walsh, N. Ambalavanan, J.E. Brumbaugh, K.L. Watterberg, E.G. Shepherd, S.E.G. Hamrick, J. Barks, C.M. Cotten, H.W. Kilbride, R.D. Higgins, H. Eunice Kennedy Shriver National Institute of Child, N. Human Development Neonatal Research, Effect of Depth and Duration of Cooling on Death or Disability at Age 18 Months Among Neonates With Hypoxic-Ischemic Encephalopathy: A Randomized Clinical Trial, JAMA, 318 (2017) 57-67.
[279] R.J. McPherson, E.J. Demers, S.E. Juul, Safety of high-dose recombinant erythropoietin in a neonatal rat model, Neonatology, 91 (2007) 36-43.
[280] X. Cheng, L. He, J. Xu, Q. Fang, L. Yang, Y. Xue, X. Wang, R. Tang, Oxygen-producing catalase-based prodrug nanoparticles overcoming resistance in hypoxia-mediated chemo-photodynamic therapy, Acta Biomater, 112 (2020) 234-249.
[281] Q. Chen, J. Chen, C. Liang, L. Feng, Z. Dong, X. Song, G. Song, Z. Liu, Drug-induced co-assembly of albumin/catalase as smart nano-theranostics for deep intra-tumoral penetration, hypoxia relieve, and synergistic combination therapy, J Control Release, 263 (2017) 79-89.
[282] Q. Zhang, H. Tao, Y. Lin, Y. Hu, H. An, D. Zhang, S. Feng, H. Hu, R. Wang, X. Li, J. Zhang, A superoxide dismutase/catalase mimetic nanomedicine for targeted therapy of inflammatory bowel disease, Biomaterials, 105 (2016) 206-221.
[283] S. Muro, X. Cui, C. Gajewski, J.C. Murciano, V.R. Muzykantov, M. Koval, Slow intracellular trafficking of catalase nanoparticles targeted to ICAM-1 protects endothelial cells from oxidative stress, Am J Physiol Cell Physiol, 285 (2003) C1339-1347.
[284] M. Armogida, A. Spalloni, D. Amantea, M. Nutini, F. Petrelli, P. Longone, G. Bagetta, R. Nistico, N.B. Mercuri, The protective role of catalase against cerebral ischemia in vitro and in vivo, Int J Immunopathol Pharmacol, 24 (2011) 735-747.
[285] H. Wang, E. Cheng, S. Brooke, P. Chang, R. Sapolsky, Over-expression of antioxidant enzymes protects cultured hippocampal and cortical neurons from necrotic insults, J Neurochem, 87 (2003) 1527-1534.
[286] A. Singhal, V.B. Morris, V. Labhasetwar, A. Ghorpade, Nanoparticle-mediated catalase delivery protects human neurons from oxidative stress, Cell Death Dis, 4 (2013) e903.
[287] M.J. Haney, Y. Zhao, S. Li, S.M. Higginbotham, S.L. Booth, H.Y. Han, J.A. Vetro, R.L. Mosley, A.V. Kabanov, H.E. Gendelman, E.V. Batrakova, Cell-mediated transfer of catalase nanoparticles from macrophages to brain endothelial, glial and neuronal cells, Nanomedicine (Lond), 6 (2011) 1215-1230.
[288] A. Joseph, T. Wood, C.-C. Chen, K. Corry, J.M. Snyder, S.E. Juul, P. Parikh, E. Nance, Curcumin-loaded polymeric nanoparticles for neuroprotection in neonatal rats with hypoxic-ischemic encephalopathy, Nano Research, 11 (2018) 5670-5688.
[289] M. Yu, J. Wu, J. Shi, O.C. Farokhzad, Nanotechnology for protein delivery: Overview and perspectives, J Control Release, 240 (2016) 24-37.

[290] D. Quintanar-Guerrero, E. Allemann, H. Fessi, E. Doelker, Applications of the ion-pair concept to hydrophilic substances with special emphasis on peptides, Pharm Res, 14 (1997) 119-127.
[291] J.D. Meyer, M.C. Manning, Hydrophobic ion pairing: altering the solubility properties of biomolecules, Pharm Res, 15 (1998) 188-193.
[292] R. Gaudana, V. Khurana, A. Parenky, A.K. Mitra, Encapsulation of Protein-Polysaccharide HIP Complex in Polymeric Nanoparticles, J Drug Deliv, 2011 (2011) 458128.
[293] A. Patel, R. Gaudana, A.K. Mitra, A novel approach for antibody nanocarriers development through hydrophobic ion-pairing complexation, J Microencapsul, 31 (2014) 542-550.
[294] Y.H. Song, E. Shin, H. Wang, J. Nolan, S. Low, D. Parsons, S. Zale, S. Ashton, M. Ashford, M. Ali, D. Thrasher, N. Boylan, G. Troiano, A novel in situ hydrophobic ion paring (HIP) formulation strategy for clinical product selection of a nanoparticle drug delivery system, J Control Release, 229 (2016) 106-119.
[295] L. Yang, F. Cui, K. Shi, D. Cun, R. Wang, Design of high payload PLGA nanoparticles containing melittin/sodium dodecyl sulfate complex by the hydrophobic ion-pairing technique, Drug Dev Ind Pharm, 35 (2009) 959-968.
[296] P.O. Hegg, Precipitation of egg white proteins below their isoelectric points by sodium dodecyl sulphate and temperature, Biochim Biophys Acta, 579 (1979) 73-87.
[297] J. Matsuura, M.E. Powers, M.C. Manning, E. Shefter, Structure and stability of insulin dissolved in 1-octanol, Journal of the American Chemical Society, 115 (1993) 1261-1264.
[298] H.S. Yoo, H.-K. Choi, T.G. Park, Protein–fatty acid complex for enhanced loading and stability within biodegradable nanoparticles, Journal of Pharmaceutical Sciences, 90 (2001) 194-201.
[299] D. Stigter, K.A. Dill, Charge effects on folded and unfolded proteins, Biochemistry, 29 (1990) 1262-1271.
[300] M. Bartoszek, W. Sułkowski, The Study of pH Influence on Bovine Liver Catalase by Means of UV-VIS Spectroscopyand Spin Labelling Method, (2006).
[301] W.G. Dai, L.C. Dong, Characterization of physiochemical and biological properties of an insulin/lauryl sulfate complex formed by hydrophobic ion pairing, Int J Pharm, 336 (2007) 58-66.
[302] K.D. Ristroph, R.K. Prud'homme, Hydrophobic ion pairing: encapsulating small molecules, peptides, and proteins into nanocarriers, Nanoscale Adv, 1 (2019) 4207-4237.
[303] S. Yang, W. Yuan, T. Jin, Formulating protein therapeutics into particulate forms, Expert Opin Drug Deliv, 6 (2009) 1123-1133.
[304] R. Liao, J. Pon, M. Chungyoun, E. Nance, Enzymatic protection and biocompatibility screening of enzyme-loaded polymeric nanoparticles for neurotherapeutic applications, Biomaterials, 257 (2020) 120238.
[305] M. Petro, H. Jaffer, J. Yang, S. Kabu, V.B. Morris, V. Labhasetwar, Tissue plasminogen activator followed by antioxidant-loaded nanoparticle delivery promotes activation/mobilization of progenitor cells in infarcted rat brain, Biomaterials, 81 (2016) 169-180.
[306] C. Zhang, C.L. Ling, L. Pang, Q. Wang, J.X. Liu, B.S. Wang, J.M. Liang, Y.Z. Guo, J. Qin, J.X. Wang, Direct Macromolecular Drug Delivery to Cerebral Ischemia Area using Neutrophil-Mediated Nanoparticles, Theranostics, 7 (2017) 3260-3275.
[307] E.M. Lutton, R. Razmpour, A.M. Andrews, L.A. Cannella, Y.J. Son, V.V. Shuvaev, V.R. Muzykantov, S.H. Ramirez, Acute administration of catalase targeted to ICAM-1 attenuates neuropathology in experimental traumatic brain injury, Sci Rep, 7 (2017) 3846.
[308] S. Krishna, A. Hutton, E. Aronowitz, H. Moore, S.J. Vannucci, The effects of adding prophylactic phenobarbital to therapeutic hypothermia in the term-equivalent hypoxic-ischemic rat, Pediatr Res, 83 (2018) 506-513.
[309] S.D. Patel, L. Pierce, A. Ciardiello, A. Hutton, S. Paskewitz, E. Aronowitz, H.U. Voss, H. Moore, S.J. Vannucci, Therapeutic hypothermia and hypoxia-ischemia in the term-equivalent

neonatal rat: characterization of a translational preclinical model, Pediatr Res, 78 (2015) 264-271.
[310] J. Rodriguez-Fanjul, C. Duran Fernandez-Feijoo, M. Lopez-Abad, M.G. Lopez Ramos, R. Balada Caballe, S. Alcantara-Horillo, M. Camprubi Camprubi, Neuroprotection with hypothermia and allopurinol in an animal model of hypoxic-ischemic injury: Is it a gender question?, PLoS One, 12 (2017) e0184643.
[311] G.A. Matchett, N. Fathali, Y. Hasegawa, V. Jadhav, R.P. Ostrowski, R.D. Martin, I.R. Dorotta, X. Sun, J.H. Zhang, Hydrogen gas is ineffective in moderate and severe neonatal hypoxia-ischemia rat models, Brain Res, 1259 (2009) 90-97.
[312] A.L. Smith, T.S. Rosenkrantz, R.H. Fitch, Effects of Sex and Mild Intrainsult Hypothermia on Neuropathology and Neural Reorganization following Neonatal Hypoxic Ischemic Brain Injury in Rats, Neural Plast, 2016 (2016) 2585230.
[313] T.R. Wood, J.K. Gundersen, M. Falck, E. Maes, D. Osredkar, E.M. Loberg, H. Sabir, L. Walloe, M. Thoresen, Variability and sex-dependence of hypothermic neuroprotection in a rat model of neonatal hypoxic-ischaemic brain injury: a single laboratory meta-analysis, Sci Rep, 10 (2020) 10833.
[314] L. Du, H. Bayir, Y. Lai, X. Zhang, P.M. Kochanek, S.C. Watkins, S.H. Graham, R.S. Clark, Innate gender-based proclivity in response to cytotoxicity and programmed cell death pathway, J Biol Chem, 279 (2004) 38563-38570.

Curriculum Vitae

ANDREA A. JOSEPH
Department of Chemical Engineering | University of Washington | Seattle, WA 98105
Phone: (802) 777-9313 | Email: ajoseph1@uw.edu

I. EDUCATION

University of Washington, Seattle, WA
Ph.D. Chemical Engineering, expected June 2021
Thesis title: Biodegradable polymeric nanoparticles for neuroprotection against neonatal brain injury

Johns Hopkins University, Baltimore, MD
B.S. Chemical and Biomolecular Engineering, awarded May 18, 2016

II. HONORS and AWARDS

2021	Outstanding Women in Engineering Award, Society of Women Engineers at UW
2020	Faculty Lecture Award, UW Chemical Engineering
2020	High Impact Publication Award, UW Chemical Engineering
2020	Krieger-Brockett Travel Award, UW Chemical Engineering
2020	AIChE Biomaterials Graduate Student Award Session (Finalist)
2020	Collegiate Rapid Fire Competition, 2nd place, Society of Women Engineers
2020	Schmidt Science Fellowship Nominee, UW
2020	Husky 100 Awardee, UW
2019	Graduate School Conference Travel Award, UW Graduate School
2019	NIH Training Course in Neurotherapeutics Discovery and Development Attendee
2018-2021	NIH F31 Fellow (8th percentile)
2018	Travel Grant, UW Graduate & Professional Student Senate
2017	National Science Foundation Graduate Research Fellowship Honorable Mention
2016	Runstad Family Endowed Fellowship Recipient
2016	Centennial Conference Champions, Johns Hopkins University Varsity Tennis
2013-2016	Engineering Dean's List, Johns Hopkins University
2013-2016	Thomas J. Watson Memorial Scholarship

III. PUBLICATIONS (*Co-first; Corresponding)

1. H. Helmbrecht, **A. Joseph**, M. McKenna, M. Zhang, E. Nance. Governing Transport Principles for Nanotherapeutic Application in the Brain, *Current Opinions in Chemical Engineering.* (2020)
2. **A. Joseph***, R. Liao*, M. Zhang, H. Helmbrecht, M. McKenna, J. Filteau, E. Nance. Nanoparticle-microglial interaction in the ischemic brain is modulated by injury duration and treatment, *Bioengineering & Translational Medicine.* (2020)
3. V. Yellepeddi, **A. Joseph**, E. Nance. Pharmacokinetics of Nanotechnology-Based Formulations in Pediatric Populations, *Advanced Drug Delivery Reviews.* (2019)
4. **A. Joseph**, T. Wood, C. Chen, K. Corry, J. Snyder, S. Juul, P. Parikh, E. Nance. Curcumin-loaded polymeric nanoparticles for neuroprotection in neonatal rats with hypoxic ischemic encephalopathy, *Nano Research*. (2018)
5. J. Smith*, K. G. Sprenger*, R. Liao, **A. Joseph**, E. Nance, J. Pfaendtner, Determining Dominant Driving Forces Affecting Controlled Protein Release from Polymeric Nanoparticles, *Biointerphases*. (2017)
6. G. Duncan, J. Jung, **A. Joseph**, A. Thaxton, N. West, M. Boyle, J. Hanes, J. S. Suk, Microstructural alterations of Sputum in Cystic Fibrosis Lung Disease, *JCI Insight*. (2016)

In preparation

1. **A. Joseph**, G. Simo, T. Gao, N. Alhindi, E. Nance. Surfactant effects on nanotherapeutic fate in the brain, *Journal of Controlled Release.* First submitted: April 2020
2. **A. Joseph**, C. Nyambura, D. Beebout, G. Bondurant, E. Nance. Formulation and efficacy of catalase-loaded nanoparticles for the treatment of neonatal hypoxic-ischemic encephalopathy, *Pharmaceutics*. Invited: September 2020

IV. PRESENTATIONS (*Presenting author)

Oral presentations

1. **A. Joseph***, E. Nance. Faculty Lecture Award: Engineering nanotherapeutics for neonatal brain injury. *UW Chemical Engineering Departmental Seminar.* Seattle, WA. (November 23, 2020)
2. **A. Joseph***, G. Simo, T. Gao, N. Alhindi, E. Nance. Graduate Student Award Session: Surfactant effects on nanotherapeutic fate within the brain. *AIChE Annual Meeting*. San Francisco, CA; Virtual. (November 17, 2020)
3. J. Filteau*, R. Liao, **A. Joseph**, E. Nance. Organotypic brain slices as a platform for measuring response to biological stimuli. *AIChE Annual Meeting*. San Francisco, CA; Virtual. (November 16, 2020)
4. E. Nance*, **A. Joseph**, R. Liao, K. Hildahl. Engineering nanomedicine to overcome biological barriers for improved treatment of pediatric brain diseases. *AIChE Annual Meeting*. San Francisco, CA; Virtual. (November 16, 2020) *Invited Plenary
5. **A. Joseph***, E. Nance. Collegiate Awards Session: Can nanoparticles treat brain disease? *Society of Women Engineers Annual Meeting.* New Orleans, LA; Virtual. (November 6, 2020)
6. E. Nance*, M. McKenna, C. Curtis, R. Liao, **A. Joseph**. Nanotechnology-based probes of structure-function in living tissue. *Clemson University Department of Chemical Engineering seminar series*. Clemson, SC; Virtual. (Sept 11, 2020)
7. A. Rios*, **A. Joseph**, E. Nance. Nanoparticle Delivery of Protein Therapeutics to Treat Neuronal Death in Hypoxic Ischemic Encephalopathy. *UW Undergraduate Research Symposium.* Seattle, WA; Virtual. (August 19, 2020)
8. **A. Joseph***, E. Nance. Can nanoparticles treat brain disease? *Town Hall Science Speaker Series.* Seattle, WA; Virtual. (June 15, 2020)
9. E. Nance*, M. McKenna, C. Curtis, R. Liao, **A. Joseph**. Nanotechnology-based probes of structure-function in living tissue. *Johns Hopkins University School of Pharmacy Seminar Series.* Baltimore, MD. (January 8, 2020)
10. **A. Joseph***, G. Simo, T. Gao, E. Nance. Effect of surfactant size and structure on biodegradable nanoparticle interaction with the brain microenvironment. *Society for Biomaterials UW Chapter Biomaterials Day.* Seattle, WA. (December 10, 2019)
11. E. Nance*, M. McKenna, C. Curtis, R. Liao, **A. Joseph**. Nanotechnology-based probes of structure-function in living tissue. *AIChE Annual Meeting*. Orlando, FL. (November 12, 2019) *Invited Plenary
12. **A. Joseph***, E. Nance. Nanoparticle design for drug delivery to the neonatal brain. *Graduate Student Symposium.* Seattle, WA. (September 19, 2019)
13. R. Liao, **A. Joseph**, T. Wood, S. Juul, E. Nance*. Nanotherapeutic modulation of inflammation and oxidative stress in neonatal brain injury. *Distinguished Lecture Series in Cardiovascular Medicine*. Seattle, WA. (January 21, 2019)
14. **A. Joseph**, R. Liao, K. Corry, T. Wood, S. Juul, P. Parikh, E. Nance*. Nanotherapeutics for neuroprotection in the developing brain. *AIChE Annual Meeting*. Pittsburgh, PA. (October 29, 2018)
15. M. McKenna, C. Curtis, **A. Joseph**, R. Liao, E. Nance*. Nanotherapeutics for neuroprotection in the injured brain. *University of Colorado Department of Chemical and Biological Engineering*. Boulder, CO. (October 11, 2018)
16. **A. Joseph**, R. Liao, E. Nance*. Nanotherapeutics for neuroprotection in the injured perinatal brain. *Houston Methodist Department of Nanomedicine Seminar Series*. Houston, TX. (July 27, 2018)
17. **A. Joseph**, T. Wood, C. Chen, K. Corry, J. Snyder, S. Juul, P. Parikh, E. Nance*. Curcumin-loaded polymeric nanoparticles for the treatment of neonatal hypoxic-ischemic encephalopathy. *Pediatric Academic Societies Annual Meeting*. Toronto, Canada. (May 6, 2018)

18. C. Curtis, M. McKenna, **A. Joseph**, R. Liao, E. Nance*. Nano-based probes of the diseased brain: directing therapeutic intervention. *BioNanoMed Annual Meeting*. Graz, Austria. (April 26, 2018)
19. **A. Joseph**, T. Wood, C. Chen, K. Corry, J. Snyder, S. Juul, P. Parikh, E. Nance. Curcumin-loaded brain penetrating nanoparticles for the treatment of neonatal brain injury. *UW Biomaterials Seminar Series.* Seattle, WA. (March 8, 2018)
20. M. Mallya*, **A. Joseph**, E. Nance. The Evaluation of Various Surfactants on PLGA and PLGA-PEG Nanoparticles. *STEMM Prep Symposium*. Seattle, WA. (August 11, 2017)

Teaching lectures and workshops

21. **A. Joseph**, C. McNicholas, J. O'Connor, A. Duvall, Y. Venkataraman. Communication with Science-Averse Audiences. *Science Talk '21.* Seattle, WA. (March 24, 2021)
22. **A. Joseph.** Nanomedicine uses in neurodegeneration. *UW Chemical Engineering 434/534: Physiological processes in engineering nanomedicine.* Seattle, WA. (March 10, 2021)
23. **A. Joseph**, C. McNicholas, J. O'Connor, M. Garrett. How to Talk Science and Discuss Controversial Topics. *UW Engage.* Seattle, WA. (March 2, 2021)
24. **A. Joseph.** Statistics in Biological Research. *UW Chemical Engineering 436: Chemical Engineering Laboratory I.* Seattle, WA. (November 10, 2020)
25. **A. Joseph.** Essential Communication Skills for Scientists. *Controlled Release Society Annual Meeting.* Valencia, Spain. (June 14, 2020)

Poster presentations

26. **A. Joseph***, R. Liao, M. Zhang, H. Helmbrecht, M. McKenna, J. Filteau, E. Nance. Injury severity impacts nanoparticle delivery to microglia in the injured brain. *Controlled Release Society Annual Meeting.* Virtual presentation (originally Las Vegas, NV). (July 2020)
27. **A. Joseph***, R. Liao, C. Nyambura, K. Hildahl, E. Nance. Nanotechnology for therapeutic applications in the developing brain. *Chemical Engineering Research Showcase.* Seattle, WA. (February 2020)
28. G. Simo*, **A. Joseph**, T. Gao, E. Nance. Evaluation of Surfactant Effects on Nanoparticle Toxicity in the Brain Microenvironment. *NCSU Future Leaders in Chemical Engineering Symposium.* Seattle, WA. (November 2019)
29. **A. Joseph***, T. Wood, C. Chen, K. Corry, J. Snyder, S. Juul, P. Parikh, E. Nance. Curcumin-loaded polymeric nanoparticles for neuroprotection in neonatal rats with hypoxic ischemic encephalopathy. *Biomedical Engineering Society Annual Meeting*. Philadelphia, PA. (October 2019)
30. G. Simo*, **A. Joseph**, T. Gao, E. Nance. Evaluation of Surfactant Effects on Nanoparticle Toxicity in the Brain Microenvironment. *NSF REU in Data-enabled Science and Engineering Symposium.* Seattle, WA. (August 2019)
31. **A. Joseph***, G. Simo, T. Gao, E. Nance. Surfactant choice in nanoparticle formulation drives nanoparticle behavior and fate in the brain. *Controlled Release Society.* Valencia, Spain. (July 2019)
32. **A. Joseph***, R. Liao, M. Zhang, C. Nyambura, J. Filteau, E. Nance. Nanotherapeutics for developmental brain injury. *Chemical Engineering Research Showcase.* Seattle, WA. (March 2019)
33. **A. Joseph***, R. Liao, E. Rhodes, H. Pontes, J. Pon, E. Nance. Surfactant effects on biodegradable nanoparticle behavior in the brain. *Nano Drug Delivery Symposium*. Portland, OR. (September 2018)
34. **A. Joseph***, T. Wood, C. Chen, K. Corry, J. Snyder, S. Juul, P. Parikh, E. Nance. Curcumin-loaded polymeric nanoparticles for neuroprotection in neonatal rats with hypoxic ischemic encephalopathy. New York City, NY. *Controlled Release Society*. (July 2018)
35. **A. Joseph**, T. Wood, C. Chen, K. Corry, J. Snyder, S. Juul, P. Parikh, E. Nance*. Curcumin-loaded brain-penetrating nanoparticles for neuroprotection in neonatal HIE. Asilomar, CA. *11th Hershey Conference on Developmental Brain Injury*. (May 2018)
36. C. Curtis*, **A. Joseph**, R. Liao, M. McKenna, M. Zhang, E. Nance. Nanotechnology and imaging-based platforms for the evaluation and treatment of neurological disease. Seattle, WA. *Chemical Engineering Research Showcase*. (March 2018)

V. TEACHING EXPERIENCE

Summer 2019	University of Washington, *Project Leader for Math Academy*
Fall 2019	University of Washington, Chemical Engineering, *Teaching Assistant for Mass Transfer and Separations*
Summer 2018	University of Washington, *Project Leader for Math Academy*
2017-present	Associates in Tutoring & Academic Consultation, *Advanced math & science tutor*
Fall 2015	Johns Hopkins University, Chemical and Biomolecular Engineering, *Teaching Assistant for Introduction to Process Analysis*
2015-16	Johns Hopkins University, Introductory Chemistry, *Peer-Led Team Learning Leader*

VI. MENTORSHIP and OUTREACH

Undergraduate Students

2020-present	Gabriella Bondurant, Chemical Engineering Bachelor's student
2020-present	Zachara Saba, Chemical Engineering Bachelor's student
2020-present	Denise Beebout, Chemical Engineering Bachelor's student NSF REU, Fall 2020
2020-present	Ana Rios, Bioengineering Bachelor's student UW STAR Program, Summer 2020
2019-present	Norah Alhindi, Molecular and Cellular Biology Bachelor's student KAUST Scholar
2019-2020	Tora Gao, BS in Chemical Engineering *Current position:* PhD student at UCLA Chemical and Biomolecular Engineering
2018-2020	Georges Simo, BS in Chemical Engineering and Biochemistry Mary Gates Research Scholarship, Class of 1954 Scholarship, 2020 Husky 100 Recipient, Spence Scholarship *Current position:* Engineer at Bristol Myers Squibb, Seattle
2018	Hugo Pontes, BS in Chemical Engineering CoMotion Fellowship, WRF Fellowship (2019, 2020), Honors Thesis candidate, 2020 Husky 100 Recipient *Current position:* PhD student at NIH Oxford-Cambridge Scholars program
2017-2020	Jessica Pon, BS in Chemical Engineering
2017-2018	Emily Rhodes, BS in Chemical Engineering 2018 Center for Sensorimotor Neural Engineering Scholarship *Current position:* PhD student at University of Colorado Boulder, Chemical and Biological Engineering
2017-2018	Andrew Kirk, BS in Chemical Engineering
2017-2018	Catherine Panlillio, BS in Chemical Engineering
2017-2018	Sanchit Gad, BS in Chemical Engineering
2017-2018	Alex Choe, BS in Chemical Engineering

High School Students

2020-present	Maria Sati, Bellevue WA
2018	Sanjana Janakiraman, Bellevue WA
2017	Meghan Mallya, Austin TX, STEMMPREP

Outreach

2020	Introduce a Girl to Renewable Energy, ACES booth lead
2019	Science demonstration at Horizon Elementary School, Mukilteo School District
2019	Engineering Discovery Days, Nance Lab booth lead
2018	Women in Science and Engineering Conference (UW), Volunteer
2018	Engineering Discovery Days, Nance Lab booth lead

2017 Engineering Discovery Days, Nance Lab booth lead
2017 Introduce a Girl to Nano, Nance Lab booth lead

VII. EXTRACURRICULAR ACTIVITIES

2021-present Communication chair and trainee representative, Controlled Release Society Nervous System Delivery Focus Group, International
2020-present Vice President for Graduate Student Membership, Society of Women Engineers at UW, Seattle WA
2020-present Treasurer, Young Scientists Committee, International
2020-present Board member, Engage Science Communication, Seattle WA
2019-present Graduate Student Liaison, Faculty Council on Women in Academia, Seattle WA
2019 President, Association of Chemical Engineering Graduate Students, Seattle WA
2018 Fundraising and event chair, Association of Chemical Engineering Graduate Students, Seattle WA
2018-2020 Sponsorship Chair, Young Scientists Committee, International
2017-2018 Vice President, Women in Chemical Engineering, Seattle WA
2016-2017 Social Director, Women in Chemical Engineering, Seattle WA
2014-2016 Mentor, Thread, Baltimore MD
2013-2016 Peer Tutor, Peer-Led Team Learning, Baltimore MD

VIII. MEMBERSHIPS

Society of Women Engineers
Controlled Release Society
American Institute of Chemical Engineers
Tau Beta Pi Engineering National Honor Society